Inaugural dissertation

for

obtaining the doctoral degree

of the

Combined Faculty of Mathematics, Engineering and Natural Sciences

of the

Ruprecht – Karls – University

Heidelberg

Presented by

M. Sc. Jonas Koch

born in Kirchheimbolanden, Germany

Oral examination: 05.03.2026

The functional relevance of adenine mRNA methylation for the progression of bladder cancer

Referees:

Prof. Dr. Frank Lyko

Prof. Dr. Michaela Frye

Abstract

Urothelial carcinoma of the bladder (UCB) presents a major health challenge, and increasing evidence indicates that epitranscriptomic reprogramming contributes to tumor development. N^6-methyladenosine (m^6A) is the most abundant internal modification in mammalian mRNA and regulates transcripts across the mRNA life cycle. The mark is installed by the m^6A writer complex, in which METTL3 serves as the catalytically active component. Although METTL3 has been implicated in many cancers, its role in UCB remains controversial, and quantitative, high-resolution maps of m^6A are lacking. Thus, this study aimed to reevaluate the role of METTL3 in UCB and to generate the first quantitative, base-resolution map of m^6A in cancer, thereby resolving the mechanisms underlying malignant epitranscriptomic reprogramming.

METTL3 knockout and inhibition impaired the oncogenic phenotype and global m^6A levels in UCB cells. A complete loss of METTL3 could not be achieved due to the selection of cells expressing aberrant METTL3 isoforms. Dependency analyses and inhibitor response assays indicated that both UCB and uroepithelial cells require METTL3 for viability. Clinically, METTL3 is upregulated in UCB. However, liquid chromatography-tandem mass spectrometry (LC-MS/MS) analyses of patient tissues found a global decrease in m^6A, emphasizing the need for rigorous m^6A mapping to resolve this contradiction. Accordingly, GLORI-seq was implemented to compare UCB with paratumoral tissue and showed systematic changes in the m^6A profile of UCB. Two central m^6A signatures were identified: a global methylation dilution driven by the upregulation of unmethylated transcripts and the downregulation of highly methylated transcripts. Conversely, differential methylation analyses found local stop-codon-proximal hypermethylation associated with an upregulation of the m^6A writer complex component VIRMA. VIRMA knockdown reduced stop-codon-proximal m^6A levels and impaired the oncogenic phenotype of UCB cells, suggesting a functional role for VIRMA in UCB development.

Taken together, this study suggests a narrow therapeutic window for systemic METTL3 inhibition in UCB due to its essential character. However, the systematic alterations of the UCB m^6A profile emphasize the diagnostic potential of m^6A profiling. Finally, this work also provides first insights into the mechanisms that drive m^6A epitranscriptomic reprogramming in cancer.

Zusammenfassung

Urotheliale Karzinome der Harnblase (UCB) stellen eine große gesundheitliche Herausforderung dar, und wachsende Evidenz zeigt, dass epitranskriptomische Reprogrammierung zur Tumorentstehung beiträgt. N^6-Methyladenosin (m^6A) ist die häufigste interne Modifikation in Säuger-mRNA und reguliert Transkripte während des gesamten mRNA-Lebenszyklus. Die Modifikation wird durch den m^6A-Schreibkomplex installiert, in dem METTL3 die katalytisch aktive Komponente darstellt. Obwohl METTL3 in vielen Krebsarten eine Rolle spielt, bleibt seine Funktion im UCB umstritten. Zudem fehlen quantitative, hochauflösende m^6A-Karten. Daher zielte diese Studie darauf ab, die Rolle von METTL3 in UCB neu zu bewerten und die erste quantitative, basen-genaue m^6A-Karte in Krebs zu erstellen, um die Mechanismen der malignen epitranskriptomischen Reprogrammierung aufzuklären.

Der Knockout von METTL3 sowie dessen Inhibition reduzierten den onkogenen Phänotyp und die globalen m^6A-Level in UCB-Zellen. Ein vollständiger Verlust von METTL3 wurde jedoch nicht erreicht, da Zellen mit aberranten METTL3-Isoformen selektiert wurden. Abhängigkeitsanalysen und Inhibitor-Antworttests zeigten, dass sowohl UCB als auch uroepitheliale Zellen für ihre Viabilität auf METTL3 angewiesen sind. Klinisch ist METTL3 im UCB hochreguliert. Flüssigchromatographie-Tandem-Massenspektrometrie-basierte Analysen (LC-MS/MS) von Patientengeweben ergaben jedoch eine globale Reduktion von m^6A, was die Notwendigkeit rigoroser m^6A-Kartierungen zur Klärung dieses Widerspruchs unterstreicht. Entsprechend wurde GLORI-seq implementiert, um UCB mit paratumoralem Gewebe zu vergleichen. Es zeigten sich systematische Veränderungen im m^6A-Profil des UCB. Zwei zentrale m^6A Signaturen wurden identifiziert: Eine globale Methylierungsverdünnung, bedingt durch die Hochregulation unmethylierter Transkripte und die Herunterregulation stark methylierter Transkripte. Im Gegensatz dazu identifizierten Differentialmethylierungsanalysen eine lokale Stopcodon-nahe Hypermethylierung, die mit einer Hochregulation der m^6A-Schreibkomplex-Komponente VIRMA verknüpft war. Der Knockdown von VIRMA verringerte die Methylierungslevel an den Stopcodons und schwächte den onkogenen Phänotyp von UCB-Zellen, was auf eine funktionelle Rolle für VIRMA in der Entwicklung von UCB hinweist.

Zusammengefasst deutet diese Studie aufgrund des essenziellen Charakters von METTL3 auf ein enges therapeutisches Fenster für eine systemische METTL3-Inhibition im UCB hin. Die systematischen Veränderungen des m^{6}A-Profils im UCB betonen jedoch das diagnostische Potenzial des m^{6}A-Profilings. Abschließend liefert diese Arbeit erste Einblicke in die Mechanismen, die die epitranskriptomische Reprogrammierung von m^{6}A in Krebs antreiben.

Table of Contents

List of abbreviations

3’READS	3' region extraction and deep sequencing
A	Adenosine
AML	Acute myeloid leukemia
APA	Alternative polyadenylation
ATCC	American Type Culture Collection
ATP	Adenosine triphosphate
BLCA	Bladder urothelial carcinoma
C	Cytidine
carRNA	chromosome-associated regulatory RNA
cDNA	coding DNA
CDS	Coding sequence
CFAPP	Cellular fractionation and affinity purification of P-bodies
CNA	Copy number alteration
Ctrl	Control
DAPI	4’,6-Diamidino-2-phenylindole
DART	Deamination adjacent to RNA modification targets
DepMap	Cancer dependency map
DMEM	Dulbecco’s Modified Eagle Medium
DMSO	Dimethyl sulfoxide
DNA	Deoxyribonucleic acid

dNTP	Deoxy nucleotidetriphosphate triphosphate
DTT	Dithiothreitol
ECACC	European Collection of Authenticated Cell Cultures
EDTA	Ethylenediaminetetraacetic Acid
ELISA	Enzyme-linked immunosorbent assay
FACS	Fluorescence-activated cell sorting
FAPS	Fluorescence-activated particle sorting
FBS	Fetal Bovine Serum
FDR	False Discovery Rate
FSC	Forward scatter
G	Guanosine
GISTIC	Genomic Identification of Significant Targets in Cancer
GLORI	Glyoxal and nitrite-mediated deamination of unmethylated adenosines
GO	Gene Ontology
GTEx	Genotype-Tissue Expression
H3K36me3	Trimethylation of histone H3 lysine 36
H3K9me2	Dimethylation of histone H3 lysine 9
H3K9me3	Trimethylation of histone H3 lysine 9
HEPES	4-(2-hydroxyethyl)-1-piperazineethanesulfonic acid
HOMER	Hypergeometric Optimization of Motif EnRichment
HRP	Horseradish Peroxidase
KD	Knockdown

KEGG	Kyoto Encyclopedia of Genes and Genomes
KH	K homology
KO	Knockout
LC-MS/MS	Liquid chromatography-tandem mass spectrometry
lncRNA	Long non-coding RNA
$m_2{}^6A$	N^6,N^6-Dimethyladenosine
m^5C	5-methylcytosine
m^6A	N^6-Methyladenosine
m^6A-CLIP	m^6A cross-linking and immunoprecipitation
m^6A-LAIC-seq	m^6A-level and isoform-characterization sequencing
m^6A_m	N^6,2′-O-dimethyladenosine
m^6A-Ref-seq	m^6A-sensitive RNA-Endoribonuclease-Facilitated sequencing
m^6A-SAC-seq	m^6A-selective allyl chemical labeling and sequencing
m^6A-SEAL-seq	m^6A selective chemical labeling-sequencing
MAC	m^6A-METTL complex
MACOM	m^6A-METTL-associated complex
MePMe-seq	Metabolic propargylation for methylation sequencing
meRIP	Methylated RNA immunoprecipitation
MES	4-(2-Sulfonatoethyl)morpholin-4-ium
MIBC	Muscle-invasive bladder cancer
miCLIP	m^6A individual-nucleotide-resolution cross-linking and immunoprecipitation
mRNA	messenger RNA

MTC	Methyltransferase complex
mtRNA	mitochondrial RNA
NMIBC	Non-muscle-invasive bladder cancer
PAGE	Polyacrylamide gel electrophoresis
P-body	Processing body
PBS	Phosphate Buffered Saline
PBST	PBS-Tween 20
PCA	Principal Component Analysis
PCR	Polymerase Chain Reaction
PDUI	Percentage of Distal polyA site Usage Index
PFA	Paraformaldehyde
P/S	Penicillin-Streptomycin
qRT-PCR	Quantitative Real-Time Polymerase Chain Reaction
RNA	Ribonucleic acid
RPMI	Roswell Park Memorial Institute
rRNA	ribosomal RNA
RSEM	RNA-seq by Expectation-Maximization
RT	Room temperature
SAM	S-adenosylmethionine
Scr	Scramble
SD	Standard deviation
SDS	Sodium dodecyl sulfate

seq	sequencing
sgRNA	single guide RNA
shRNA	short hairpin RNA
STAR	Spliced Transcripts Alignment to a Reference
T	Thymidine
TBE	Tris-borate-EDTA
TCGA	The Cancer Genome Atlas
TEC	to be experimentally confirmed
TNM	Tumor-Node-Metastasis (staging system)
TPM	Transcripts Per Kilobase Million
t-SNE	t-distributed Stochastic Neighbor Embedding
TURBT	Transurethral resection of the bladder tumor
U	Uridine
UCB	Urothelial carcinoma of the bladder
UCSC	University of California, Santa Cruz
UICC	Union for International Cancer Control
UMAP	Uniform Manifold Approximation and Projection
UTR	Untranslated region
WT	Wild type
YTH	YT521-B homology

List of Figures

List of Tables

1 Introduction

1.1 Urothelial carcinoma of the bladder (UCB)

Bladder cancer is among the most prevalent malignancies of the urinary tract, and approximately 90% - 95% of cases originate from the urothelial lining [1]. Consequently, UCB represents the most common subtype of bladder cancer. In the United States, UCB is the fourth most frequently diagnosed cancer in men, with an estimated 65,080 new cases in 2025. It also ranks as the eighth leading cause of cancer-related deaths, accounting for approximately 12,640 deaths in the same year [2].

UCB can be classified according to the depth of tumor invasion into the bladder wall, distinguishing non-muscle-invasive bladder cancer (NMIBC) from muscle-invasive bladder cancer (MIBC, Fig. 1). About 75% of diagnosed cases are NMIBC, which remain confined to the urothelium or lamina propria without invasion of the bladder muscle [3]. Despite favorable outcomes, with a five-year survival rate of around 90%, NMIBC is associated with a high recurrence rate, ranging from 31% to 78% within five years [4]. Within the tumor-node-metastasis (TNM) staging system, stages Ta, Tis, and T1 fall into the NMIBC category. NMIBC is typically treated with transurethral resection of the bladder tumor (TURBT) [1].

10% - 20% of NMIBC cases progress to MIBC, which encompasses stages T2 to T4 of the TNM classification system. MIBC is characterized by a substantially worse prognosis due to its invasive growth and high metastatic potential [3,4]. The five-year survival rate decreases to approximately 9% for patients with distant metastases [2]. Standard treatment for MIBC patients includes radical cystectomy in combination with neoadjuvant chemotherapy [4].

Despite recent advances in cancer diagnostics, surgical techniques, and systemic therapies, the overall survival rates for UCB have remained largely unchanged since the 1990s [3]. With global population growth and aging, the incidence and prevalence of UCB are expected to rise further in the coming decades [5]. Currently, there are no approved early detection biomarkers for UCB, highlighting an urgent need for new diagnostic biomarkers and therapeutic targets to improve patient outcomes [6,7].

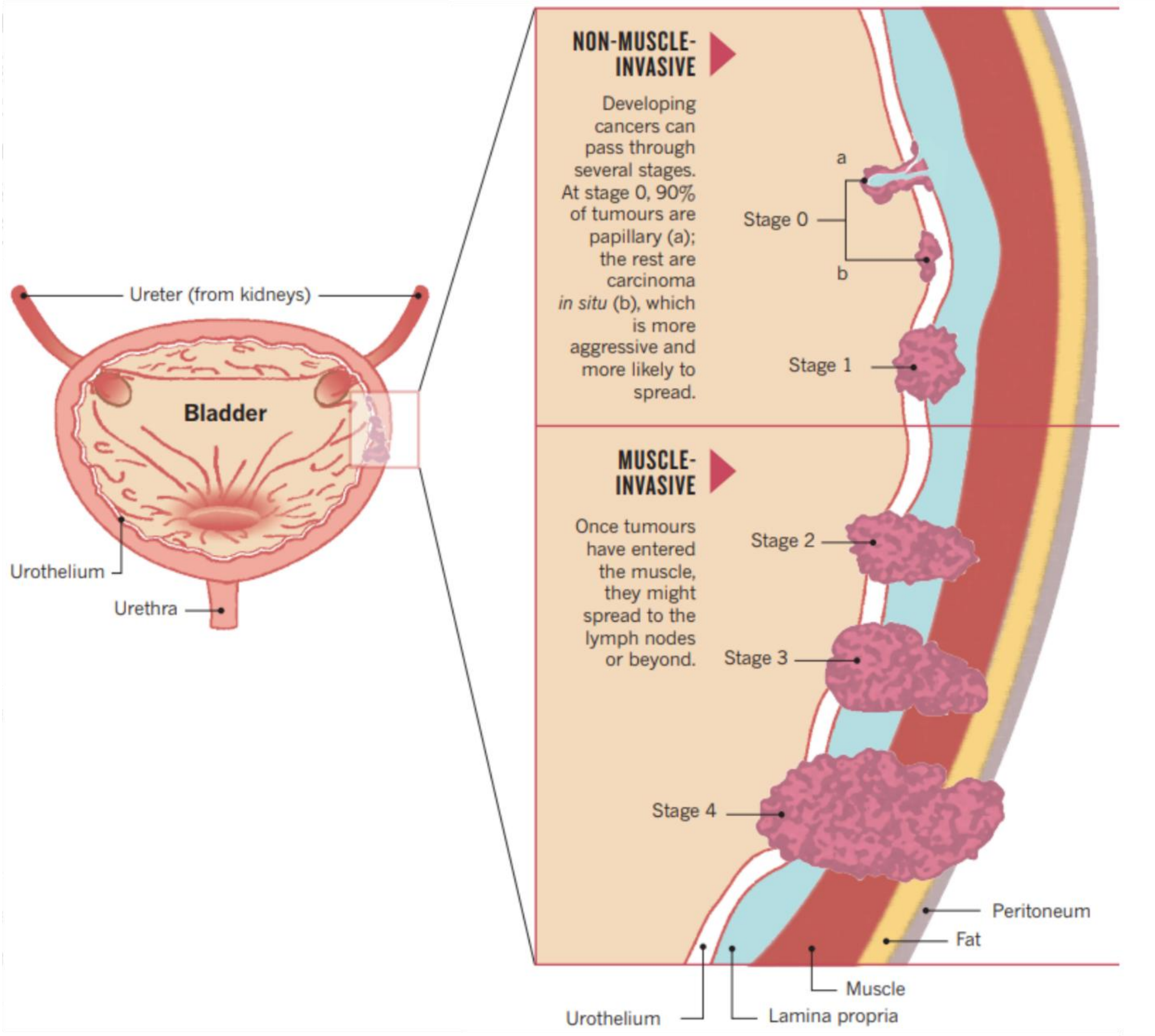

Fig. 1: Staging of UCB into NMIBC and MIBC. Carcinomas *in situ* (b) have a higher potential to spread than non-invasive papillary tumors (a). T2 tumors already invade the bladder muscle and have an increased risk of metastasizing. This figure was modified from Berdik, 2017 [3].

1.2 N^6-Methyladenosine (m^{6}A) mRNA methylation

1.2.1 Writing of m^{6}A - The m^{6}A methyltransferase complex (MTC)

m^{6}A is the most abundant internal RNA modification of mRNAs in eukaryotes. m^{6}A is catalyzed co-transcriptionally by a multiprotein MTC that has a nuclear localization (Fig. 2) [8,9]. The different subunits of the MTC have diverse catalytic and regulatory functions. METTL3 is the catalytically active writing component of the complex and is responsible for transferring a methyl group from the S-adenosylmethionine (SAM) donor to the transcript acceptor adenine [10-12]. METTL14 forms a heterodimer with METTL3, facilitates substrate recognition, and stabilizes the structural conformation of METTL3 that is required for m^6A catalysis [10-12]. Notably, METTL14 also contains a methyltransferase domain that was initially presumed to enable the protein to modify target transcripts. However, structural insights into the complex revealed that the active site of METTL14's methyltransferase domain is degenerated and incapable of binding SAM [12]. Biochemical m^6A methylation assays finally confirmed the lack of METTL14's writing activity [10-12]. Phylogenetic analyses furthermore suggested that METTL14 lost its methyltransferase activity [13]. Together, METTL3 and METTL14 form the m^6A-METTL complex (MAC), which represents the catalytic subunit of the MTC [14,15]. The METTL3-METTL14 dimer further associates with WTAP, which was shown to be important for RNA binding, m^6A deposition specificity along the transcripts, and the localization of the MTC to nuclear speckles [16,17]. Further components of the MTC comprise RBM15 and its paralogue RBM15B [18,19]. These proteins were found to bind to U-enriched mRNA regions and to be important for the recruitment of the MTC to the XIST long non-coding RNA (lncRNA) [19]. It was shown that MTC-mediated deposition of m^6A on XIST is required for transcriptional silencing of genes located on the X chromosome [19]. VIRMA, also known as KIAA1429, was shown to be responsible for site-specific deposition of m^6A close to the stop codon and in the 3' untranslated region (UTR) of transcripts [18,20]. ZC3H13 was identified to be important for the nuclear localization of the MTC via its interaction with WTAP, VIRMA, and HAKAI [18,20,21]. HAKAI is required for the stabilization of the MTC in *Drosophila* and humans [18,20,22]. Together, WTAP, RBM15, RBM15B, VIRMA, ZC3H13, and HAKAI form the so-called MAC-associated complex (MACOM), which represents the regulatory subunit of the MTC [14,15]. Cryo-electron microscopy analyses revealed that MACOM and MAC bind to each other via METTL3 - WTAP interactions to form a functional MTC for m^6A catalysis [15]. Together, the MTC has an expected molecular weight of approximately 1,000 kDa [20].

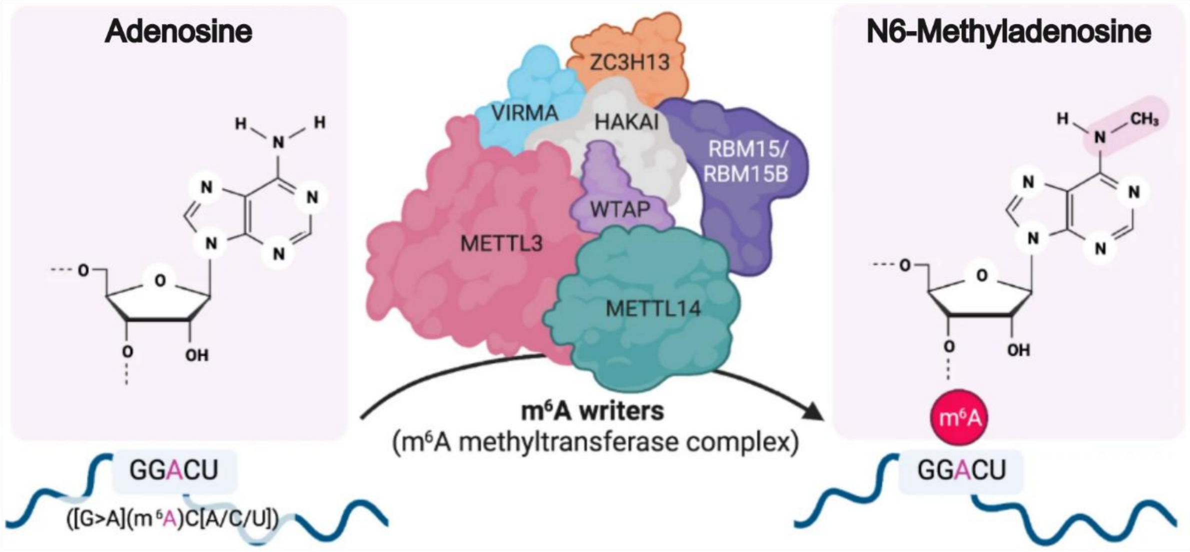

Fig. 2: The m^{6}A methyltransferase complex. METTL3 represents the catalytically active writer enzyme that installs m^{6}A. METTL14 forms a heterodimer with METTL3 and is responsible for the stabilization of METTL3 and RNA recognition. All other components of the complex have important regulatory functions, affecting the localization of the complex and m^{6}A deposition selectivity. This figure was modified from Hong *et al*., 2022 [23].

1.2.2 m^{6}A abundance in the protein-coding transcriptome

Liquid chromatography-tandem mass spectrometry (LC-MS/MS) analyses showed that the global m^{6}A/A ratio ranges from 0.15% to 0.6% in mRNA [9]. Notably, this ratio is strongly influenced by highly expressed transcripts. Depending on the tissue context, 10 - 1,000 expressed transcripts from the entire mRNA transcriptome can comprise the majority of the mRNA pool [24]. Concerning the percentage of mRNAs in the transcriptome that contain at least one m^{6}A modification site, antibody-dependent m^{6}A mapping techniques found that m^{6}A peaks were present in approximately 7,000 - 8,000 transcripts [25,26]. This would correspond to 35% - 40% of all mRNAs that contain m^{6}A modifications if a total number of 20,000 protein-coding genes is assumed. However, this number likely represents an underestimate, as gene expression is cell type-specific and lowly expressed genes may not be detected due to insufficient sequencing depth. In GLORI-seq, which represents a base-resolution, antibody-independent m^{6}A mapping technique, deep-seq at 140x coverage revealed a total number of 170,000 m^{6}A sites, with at least 87% of all transcripts found to contain modification sites [27]. Regarding the number of m^{6}A sites per transcript, original LC-MS/MS studies using mouse

L cells suggested an average of 3 modification sites per transcript [28]. Later, an antibody-dependent method reported an average of approximately 1.7 m^6A peaks per transcript [25]. More recently, GLORI-seq identified an average of 10 m^6A sites per transcript [27].

1.2.3 Selectivity of m^6A deposition along mRNAs

The METTL3-METTL14 heterodimer was found to exert intrinsic selectivity with respect to sequence preference in m^6A deposition on mRNA. The consensus sequence motifs in which m^6A occurs were described as the so-called RRACH (R = A or G; H = A, C or U) [29-33], DRAC (D = A, G or T; R = A or G), or DRACH (D = A, G or T; R = A or G; H = A, C or U) motifs [25,34]. Recently, GLORI-seq also described the presence of non-canonical motifs in HEK293T cells [27]. In a pathophysiological context, a gain-of-function missense mutation in METTL14 ($\text{METTL14}^{\text{R298P}}$), which is frequently observed in cancer patients, was shown to affect METTL3-METTL14 m^6A deposition specificity, which resulted in the preferential methylation of non-canonical GGAU motifs [35]. These findings showed that METTL14 mutations affect m^6A deposition selectivity, which may also hold true for other subunits of the MTC. Furthermore, m^6A sites were shown to occur in distinct regions of mRNA transcripts. Generally, m^6A sites can be located throughout the length of a transcript, but the modification sites preferentially occur in the coding sequence (CDS) and the 3’-UTR of transcripts, with the strongest enrichment around the stop codon [25,26,34]. The selectivity toward the stop codon and the 3’-UTR might be promoted by VIRMA, but the underlying mechanisms are not understood [20]. Selectivity toward distinct mRNA regions might also be influenced by other regulatory subunits of the MTC, such as RBM15 and its paralogue RBM15B, which were shown to preferentially bind U-enriched mRNA regions via their RNA-binding domains [19]. Besides this MTC-intrinsic selectivity for m^6A installation, gene architecture was also described to affect m^6A deposition. It was shown that m^6A is often placed within long internal exons [25,26,34], and near terminal exon-exon junctions, which were suggested to represent the structural feature that promotes the described m^6A enrichment around the stop codon [33]. Additionally, chromatin marks were linked to MTC recruitment. For example, the trimethylation of histone H3 lysine 36 (H3K36me3) was found to be enriched in long internal exons [36]. However, recent studies proposed that m^{6}A deposition is not selective at all, but exclusion-based [37-39]. It was hypothesized that DRACH motifs are modified by default if they are located more than approximately 100 nucleotides away from a splice junction. If not, the motif should not be accessible for the MTC due to the presence and steric hindrance of the exon junction complex [37-39]. This postulated mechanism provides another example of gene architecture-dependent m^{6}A deposition. Another cis-regulatory feature that potentially affects m^{6}A deposition is mRNA secondary structure. In *in vitro* methylation experiments, substrate RNAs with secondary structures inhibited methylation by recombinantly expressed METTL3-METTL14 dimers [40]. Recently, the role of RNA secondary structure in m^{6}A deposition and evolution was confirmed in yeast and mammalian hybrid systems. In yeast, changes in the DRAC consensus sequence motifs and changes in the target site secondary structure were the two mechanisms identified that exclusively determined m^{6}A deposition in yeast [41]. In mammals, 60% of methylation changes could be explained by these cis-regulatory mechanisms, thereby raising the question to what extent trans-regulatory mechanisms influence m^{6}A deposition. Trans-regulatory mechanisms that could impact m^{6}A installation include the recruitment of the MTC to distinct target sites by transcription factors, as well as RNA-binding proteins [42-44]. The H3K36me3-mediated guidance of the MTC toward nascent RNA could furthermore decide which sequence motifs are selected for m^{6}A deposition during transcription [36]. As m^{6}A catalysis occurs co-transcriptionally, interactions of the MTC and the RNA polymerase II complex were also considered to be important for m^{6}A deposition. In this regard, an interaction between METTL3 and the RNA polymerase II complex was reported, as well as a correlation between transcription dynamics and m^{6}A deposition [45]. Taken together, several mechanisms are suggested to affect m^{6}A deposition and its selectivity. These mechanisms are considered to dictate which sequence motifs are highly methylated, less frequently methylated, or completely unmethylated. However, the molecular basis of these processes remains poorly understood and requires further investigation [9].

1.2.4 Molecular mechanisms of m^{6}A-dependent transcript regulation

m^{6}A affects the fate of its target transcripts in all steps of the mRNA life cycle, including pre-mRNA-processing, nuclear export, stability, and translation. Most of these m^{6}A-dependent effects are mediated by reader proteins. Proteins of the YT521-B homology (YTH) family are the best studied m^{6}A readers and essentially comprise YTHDC1, as well as YTHDF1, YTHDF2, and YTHDF3 [46]. Also, members of the IGF2BPs were described to bind m^{6}A via their K homology (KH) domains and have also been recognized as relevant readers [47,48]. Here, the different molecular mechanisms of m^{6}A-dependent transcript regulation are highlighted and summarized in Fig. 3.

YTHDC1 is involved in several steps of m^{6}A-dependent mRNA processing that occur in the nucleus. It was shown that YTHDC1 interacts with different splicing and polyadenylation factors to regulate the splicing and alternative polyadenylation (APA) of mRNAs [49,50]. By interacting with SRSF3 and NFX1, YTHDC1 was also found to regulate the nuclear export of m^{6}A-modified transcripts [51]. As already described, the RBM15 and RBM15B proteins are responsible for the recruitment of the MTC to the XIST lncRNA. MTC-mediated XIST methylation is recognized by YTHDC1 and results in the silencing of X chromosome genes [19]. Furthermore, several links between m^{6}A methylation and chromatin modulation have been established [52]. It was shown that YTHDC1 regulates the removal of the repressive H3K9me2 mark via the recruitment of KDM3B toward m^{6}A-modified chromatin, thereby promoting gene expression [53]. Additionally, YTHDC1 was found to bind m^{6}A-marked retrotransposon transcripts and to recruit SETDB1 for the installation of repressive H3K9me3 marks, which influenced embryonic stem cell identity in mice [54]. It was also reported that YTHDC1 binds m^{6}A sites on chromosome-associated regulatory RNAs (carRNAs) to promote their degradation via the nuclear exosome, thereby regulating chromatin accessibility and transcription rates [55]. An emerging concept of m^{6}A-dependent transcript regulation is referred to as compartmentalization, which describes the recruitment of m^{6}A-modified transcripts into phase-separated condensates [56]. YTHDC1 was originally described as a protein located in phase-separated nuclear speckles [57,58]. It was shown that the low-complexity regions of YTHDC1 promote its phase separation potential, inducing the formation of nuclear YTHDC1-m^{6}A condensates [59]. The recruitment of transcripts into these condensates affects their regulation. For example, the compartmentalization of MYC transcripts by YTHDC1 prevented their degradation via the PAXT-exosome complex in the context of acute myeloid leukemia (AML) [59]. Also, binding of YTHDC1 to m^6A-modified MALAT1 transcripts was shown to regulate the composition and genomic binding sites of nuclear speckles, which affects gene expression [60].

The m^6A-dependent mechanisms mediated by cytoplasmic YTHDF proteins are currently debated in the field. Originally, it was suggested that YTHDF proteins have distinct, exclusive m^6A binding sites and therefore distinct functions. In this model, YTHDF1 promotes translation of its target transcripts, for example, via interactions with eIF3a/b and eEF2 [52,61]. YTHDF2 is essentially associated with the degradation of target transcripts, which is caused through interactions with the CCR4-NOT deadenylase complex [62,63]. YTHDF3 was shown to enhance translation of distinct transcripts, most likely by an interaction with YTHDF1 [64,65]. Also, YTHDF3 was reported to facilitate mRNA degradation via YTHDF2 [64]. More recent analyses suggested that the binding properties and functions of the different YTHDF readers are redundant and that these readers exclusively promote transcript degradation, likely via the CCR4-NOT deadenylase complex [66,67]. YTHDF1 and YTHDF3 were also shown to promote transcript degradation, but to a lesser extent than YTHDF2 [63], which is consistent with the finding that loss of YTHDF2 has a more pronounced impact on mRNA stability compared to the loss of YTHDF1 or YTHDF3 [67]. Notably, the strongest accumulation of m^6A-modified transcripts was observed when all YTHDF proteins were depleted, thereby indicating that all YTHDF readers play a role in transcript degradation [67]. The predominant role of YTHDF2 in mRNA degradation was further manifested when YTHDF2 was found to recruit the RNase P/MRP via an HRSP12 interaction to induce endonucleolytic cleavage of target mRNAs [68]. Furthermore, YTHDF2 was shown to promote decapping of transcripts through recruitment of PNRC2 and DCP1A via an UPF1 interaction [69]. Similar to YTHDC1, the YTHDF proteins also contain a low-complexity region that promotes phase separation into cytoplasmic condensates, which were shown to further partition into stress granules and P-bodies [62,70,71]. Thus, m^6A-dependent transcript regulation via compartmentalization is promoted by YTHDF reader proteins. Most recently, it was shown that relatively long mRNAs are targeted to stress granules via YTHDF proteins, suggesting that m^6A controls the length-dependent accumulation of transcripts in stress granules [72].

Direct m^{6}A-binding of eIF3 to the 5’-UTR of transcripts was shown to promote cap-independent translation [73]. Furthermore, circularization of transcripts induced by METTL3 was also found to stimulate cap-independent translation via eIF3 [74].

The IGF2BP readers were shown to promote transcript stabilization, which also positively affected their translation [47,48]. Furthermore, IGF2BP proteins mediate transcript compartmentalization [47,75]. It was shown that IGF2BP3 regulates the translation of its targets by spatially separating them into non-translating and actively translating pools. Poly-m^{6}A-methylated transcripts were targeted into P-bodies, which inhibited their translation. Global m^{6}A reduction led to a re-localization of the targets from P-bodies to active polysomes [75].

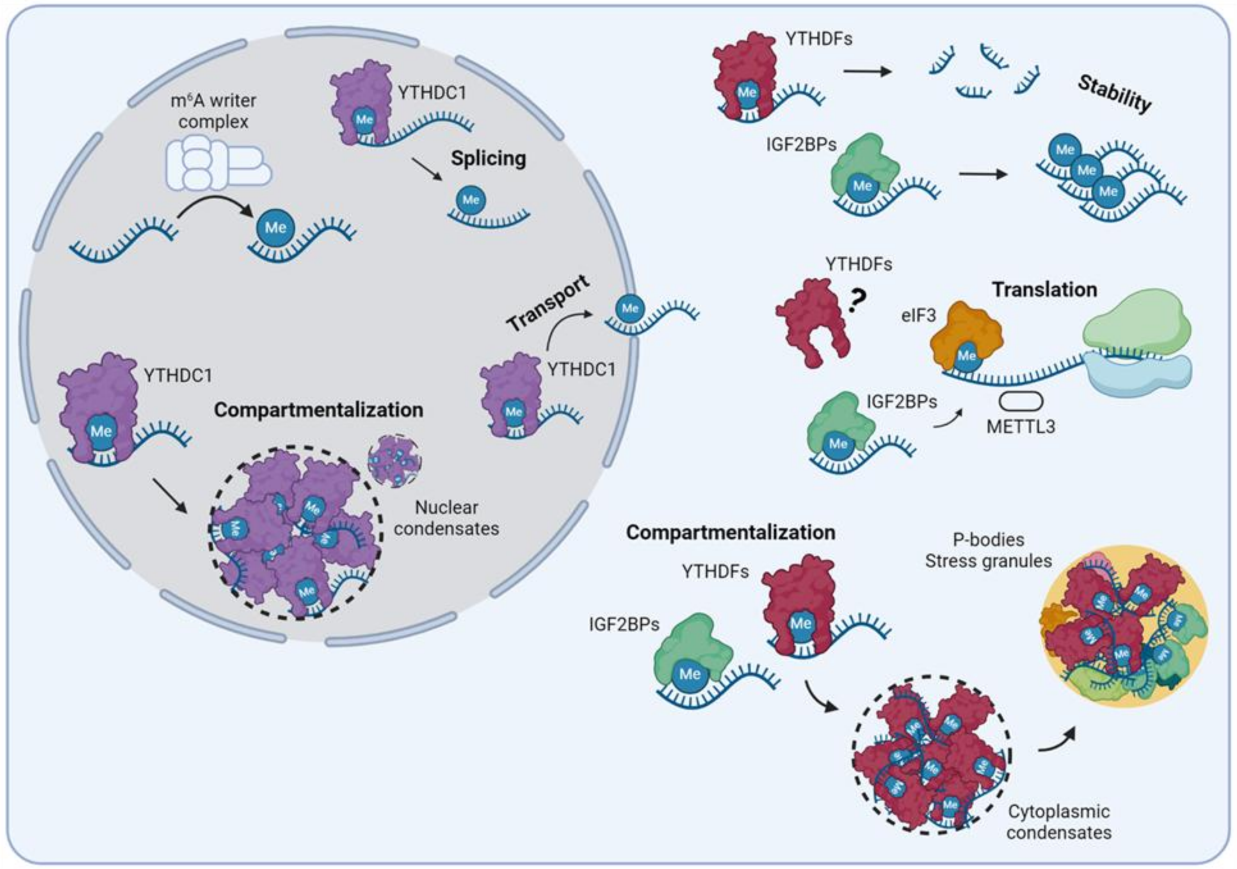

Fig. 3: Mechanisms of m^{6}A-dependent transcript regulation. After m^{6}A deposition via the m^{6}A writer complex, m^{6}A readers essentially affect the regulation of modified mRNAs. YTHDC1, the key nuclear m^{6}A reader, was shown to be involved in alternative splicing and transport of transcripts. The cytosolic YTHDF m^{6}A reader proteins are known for mediating the decay of m^{6}A-modified transcripts. In contrast, IGF2BP reader proteins promote the stabilization of marked mRNAs and were shown to be involved in their translation. Shown readers were also found to promote the compartmentalization of m^{6}A-modified mRNAs into phase-separated condensates that can further fuse with other condensates, including P-bodies. Thereby, m^{6}A readers affect the localization and stabilization of their targets. This figure was taken from Koch and Lyko, 2024 [56].

1.3 Methods for the detection and quantification of m^6A

For the detection of m^6A in the transcriptome, multiple methodologies have been developed. However, the detection of m^6A still represents a major problem in the field, mainly due to method-specific limitations and the lack of techniques that allow for an absolute quantification of m^6A levels. In this section, an overview of the different m^6A detection approaches is provided. Also, their advantages and limitations are described.

1.3.1 Global quantification of m^6A

RNA dot blots and enzyme-linked immunosorbent assays (ELISA) are commonly used to measure global m^6A methylation levels. These methods make use of m^6A-targeting antibodies that allow for the detection of m^6A-modified mRNAs that were previously immobilized. However, these antibodies suffer from limited specificity as they were described to cross-react with other RNA modifications and to promiscuously bind to certain RNA sequences or structures [76]. In addition, the enrichment of mRNA from total RNA preparations is challenging as ribosomal RNA (rRNA) contaminants, which are m^6A-methylated by METTL5, are difficult to deplete and make up more than 90% of the transcriptome [77]. Therefore, the source of the detected signal is difficult to interpret and can vary between different mRNA preparations and antibodies. LC-MS/MS is a more stringent method for measuring m^6A levels globally and allows for the quantification of distinct RNA modifications with high sensitivity by using external calibrations, spike-in controls, and radio-labelled internal standards [78]. Furthermore, LC-MS/MS can measure rRNA-specific modifications like N^6,N^6-dimethyladenosine ($m_2{}^6A$) in parallel to the quantification of m^6A, which allows for the determination of the degree of contaminating rRNA species in the corresponding mRNA preparation. Therefore, equal levels of rRNA contamination in different mRNA preparations make detected differences in m^6A methylation levels more reliable.

1.3.2 Detection and quantification of m^6A at transcript and base resolution

1.3.2.1 Antibody-dependent detection methods

The first methods that enabled the detection of m^6A on the transcript level were m^6A-seq and methylated RNA immunoprecipitation sequencing (meRIP-seq) [25,26]. Those methods combined the use of m^6A antibodies for immunoprecipitation of modified transcripts and deep-seq to detect m^6A transcriptome-wide. From those results, the DRACH m^6A consensus sequence motif and the distribution of m^6A along the transcripts, with the typical enrichment in the 3'-UTR and near the stop codon, were described for the first time [25,26]. However, these antibody-dependent methods suffer from poor antibody specificity, resulting in the detection of other RNA modifications like N^6,2'-O-dimethyladenosine (m^6A_m), and low resolution. In m^6A- and meRIP-seq, modification peaks in 200-nucleotide RNA fragments are called, but the precise position(s) of the modified adenosine residue(s) within these peaks cannot be identified. Furthermore, the methylation status of the modification site cannot be quantified using these approaches [76,79].

Several efforts were made to improve the performance of the antibody-dependent methods. In the m^6A cross-linking and immunoprecipitation (m^6A-CLIP) and m^6A individual-nucleotide-resolution cross-linking and immunoprecipitation (miCLIP) methods, the resolution of m^6A mapping could be improved [33,34]. After fragmentation and antibody-based enrichment of modified transcripts, RNAs are cross-linked to the antibody by UV-irradiation. It was shown that these cross-links create mutational signatures and truncations after reverse transcription of the RNA, which are then used to identify m^6A sites at single-nucleotide resolution [33,34]. With m^6A-level and isoform-characterization sequencing (m^6A-LAIC-seq), it also became possible to quantify the ratio of methylated to non-methylated transcripts and to compare the methylation status of alternatively spliced isoforms using an antibody-dependent method [80]. In m^6A-seq2, a multiplexing approach was introduced that counteracts the requirement for performing the immunoprecipitation step for each sample separately, which is prone to technical noise and batch effects [81]. In brief, fragmented RNA from different samples is barcoded via RNA adaptor ligations, pooled, and then enriched by a single immunoprecipitation step. Therefore, the technical variability, costs, input material, and labor of m^{6}A-seq and meRIP-seq were reduced [81].

Despite this progress in improving the performance of antibody-dependent m^{6}A detection methods, important limitations remain. Specificity represents the major limitation, as the m^{6}A antibodies were shown to cross-react with other RNA modifications and to exert an intrinsic preference to bind toward distinct RNA structures. Furthermore, differences concerning the specificity of antibodies from different distributors affect the reproducibility of the assays. Also, transcriptome-wide stochiometric information of m^{6}A at base-resolution is required to precisely connect m^{6}A to transcript fate and cellular phenotypes [76,79].

1.3.2.2 (Chemo-)enzymatic detection methods

Thus, several antibody-independent m^{6}A detection methods were developed in recent years. In MAZTER-seq and m^{6}A-sensitive RNA-Endoribonuclease-Facilitated sequencing (m^{6}A-Ref-seq), modification sites can be identified by the methylation-sensitive endoribonuclease MazF. The enzyme selectively cuts non-methylated ACA motifs in the transcriptome, while m^{6}ACA sites remain intact [82,83]. In those techniques, MazF-fragmented RNA is sequenced and enables base-resolution detection of m^{6}A as well as quantification of methylation levels based on the cut/uncut reads ratio at each position. Therefore, MAZTER-seq and m^{6}A-Ref-seq represented the first sequencing methods that allowed for an absolute quantification of m^{6}A levels. For the detection and semi-quantitative quantification of individual sites, MazF-treated samples are analyzed by qRT-PCR using primers that flank the ACA site of interest and a non-ACA control site for normalization. However, these MazF-based methods are limited to ACA motifs and do not detect modification sites in other consensus sequence motifs. Thus, only 16% of all potential m^{6}A sites in the mammalian transcriptome can be detected [82,83]. Furthermore, it was found that the MazF enzyme does not achieve a complete digestion of unmodified ACA motifs, which leads to the detection of false positives [84].

In deamination adjacent to RNA modification targets sequencing (DART-seq), a fusion protein, which consists of the YTH domain from the YTHDF2 reader and the APOBEC1 enzyme that catalyzes C→U deamination, is used for the detection of m^{6}A sites [85]. APOBEC1-YTH binds to

m^6A sites via the YTH domain while APOBEC1 deaminates the cytosine that follows the modified adenosine in the DRACH consensus sequence motif. The introduced C→U mutations can be detected as C→T editing events by RNA-seq and allow for local or transcriptome-wide base-resolution mapping of m^6A as well as a semi-quantitative methylation level readout. Furthermore, DART-seq can be performed *in vitro* via recombinant expression of APOBEC1-YTH or in cells via transfection/transduction of target cells [85-87]. Additionally, DART-seq was the first technique used for m^6A detection in single cells [87]. However, DART-seq relies on several controls to filter false-positive modification sites that result from unspecific cytosine editing by the APOBEC1 moiety. A mutated APOBEC1-YTH construct with a deletion in the m^6A-binding motif shows reduced binding affinity to m^6A sites and therefore results in no or reduced editing at true-positive modification sites. This control indicates that the APOBEC1-YTH deaminase activity is specifically directed by the YTH domain's binding function. Similarly, editing events detected in an APOBEC1-only control should be considered as false positives and filtered [85].

Besides these purely enzyme-assisted approaches, several chemo-enzymatic techniques have been developed for the detection of m^6A. These methods aim at the detection of m^6A by its chemical or metabolic labelling and comprise m^6A selective chemical labeling-seq (m^6A-SEAL-seq) [88], m^6A-label-seq [89], metabolic propargylation for methylation sequencing (MePMe-seq) [90,91], and m^6A-selective allyl chemical labeling and sequencing (m^6A-SAC-seq) [92,93]. However, m^6A detection methods based on chemical or metabolic labeling can suffer from incomplete labeling, rely on enzymatic efficiency, and have limited applicability to biological or clinical samples.

1.3.2.3 Chemical-assisted detection methods

The detection of m^6A by chemical treatments is challenging since its chemical properties are similar to unmodified adenosines, thereby hindering their discrimination. Also, the N^6-methyl group of m^6A is considered chemically inert to most treatments [88]. Thus, assays based on the principle of the chemical conversion of distinct nucleotides combined with deep-seq, such as those established for 5-methylcytosine (m^5C) in DNA and RNA bisulfite sequencing [94-97], were difficult to establish for m^6A. Nevertheless, the community was seeking a bisulfite-seq-comparable method for m^{6}A detection as it provides a quantitative, base-resolution approach that is not biased by the use of antibodies and enzymes.

In glyoxal and nitrite-mediated deamination of unmethylated adenosines (GLORI)-seq, an optimized deamination protocol was provided [27]. To reduce the nitrous acid-mediated deamination of guanosines into xanthosines, which were shown to block the reverse transcription step in the preparation of sequencing libraries, a protection step was included. Before deamination, the RNA is treated with glyoxal and boric acid. Glyoxal reacts with the exocyclic amino group of nucleobases. This reaction is further stabilized by boric acid treatment, allowing for subsequent nitrite-mediated deamination. It was also shown that the addition of glyoxal to the deamination reaction further improved A→G conversion. Thus, glyoxal serves as an essential catalyst that promotes A→G conversion, while blocking the deamination of guanosines. After deamination, protected guanosines are then deprotected under alkaline conditions. m^{6}A residues resist glyoxal and sodium nitrite-mediated deamination. By further optimizations concerning reagent concentration, reaction temperature, and incubation time, 98% - 99% global A→G conversion ratios were achieved for mRNA preparations from HEK293T cells [27]. The achieved conversion ratios are lower than ratios obtained for bisulfite sequencing, which usually reach near complete conversion of unmodified cytosines, but the higher copy number of RNA molecules, as well as the higher m^{6}A abundance, likely buffer the detection of false positives. GLORI-tools, the associated bioinformatics pipeline for GLORI-seq analysis, enables user-defined threshold settings for m^{6}A site detection, allowing the fine-tuning of specificity and sensitivity. For the first time, GLORI-seq enabled a quantitative description of the m^{6}A transcriptome. In HEK293T cells, roughly 170,000 m^{6}A sites were identified. 87% of all transcripts were found to contain at least one modification site with a median methylation level of roughly 40%. Also, the presence of a non-canonical m^{6}A sequence motif (GGAUU) was described, which was found to be less methylated than the canonical DRACH motifs. Like other detection methods, the typical distribution of m^{6}A sites along transcripts could be confirmed. Concerning the regulatory functions of m^{6}A, GLORI identified that m^{6}A sites frequently appear in clusters. Those clustered sites showed higher methylation levels than non-clustered sites and could be linked to transcript regulatory functions.

Furthermore, GLORI allowed the quantitative tracking of m^6A dynamics when comparing stressed and unstressed HeLa and MEF cells. Approximately 5% - 10% of m^6A sites were found to be dynamic under hypoxia and heat shock conditions. [27]. Taken together, GLORI-seq represents a chemical-assisted m^6A detection method that resembles bisulfite sequencing for m^5C. GLORI achieves transcriptome-wide base-resolution mapping of m^6A and allows for the absolute quantification of m^6A at each position based on the A→G conversion ratio (Fig. 4). Therefore, GLORI may emerge as the gold-standard approach for quantitative m^6A profiling.

1.3.2.4 Detection by direct RNA-seq

Unlike other methods that detect m^6A indirectly by sequencing reverse-transcribed RNA libraries, the Oxford Nanopore Platform enables direct detection of RNA modifications. In direct RNA-seq, RNA molecules are pulled through a membrane-embedded protein pore, which leads to nucleotide-characteristic profiles of the constantly measured current intensity. These profiles are then used for the computational identification of the respective nucleotide. While passing the RNA molecule through the pore, the current intensity changes depending on the sequence of the molecule. Those changes are referred to as “squiggles”, which are ultimately used for the determination of the RNA sequence [98]. Modified RNA nucleotides have different current intensities compared to unmodified nucleotides, thereby enabling RNA modification detection. In 2019, the first algorithm for the identification of m^6A in native RNA molecules was developed, which is based on the detection of systematic “errors” and decreased base-calling quality [99]. Generally, algorithms for m^6A detection are either comparative or supervised [100]. Comparative algorithms have the advantage that they do not require training data sets for modification calling, as they compare RNA molecules of interest with a m^6A-free control sample [101]. However, m^6A-free control samples are not always available, thereby limiting the use of comparative algorithms. For training supervised algorithms, training data sets have to be generated, for example, by sequencing synthetic RNA oligonucleotides. Also, published data sets can be used. These data sets are used to train a classifier that ultimately determines the presence or absence of a m^6A modification site in an unknown RNA sample. Supervised algorithms enable detection from single samples and can identify multiple RNA modifications simultaneously if the training data supports it [102,103]. The performance of a supervised algorithm essentially depends on the training data set, which represents a major limitation. Synthetic RNA oligonucleotides do not represent the most suitable training data set as they are less complex than a cellular transcriptome, which likely leads to base calling errors. Additionally, most available published m^{6}A data sets for training supervised algorithms derive from m^{6}A sequencing methods that have several limitations.

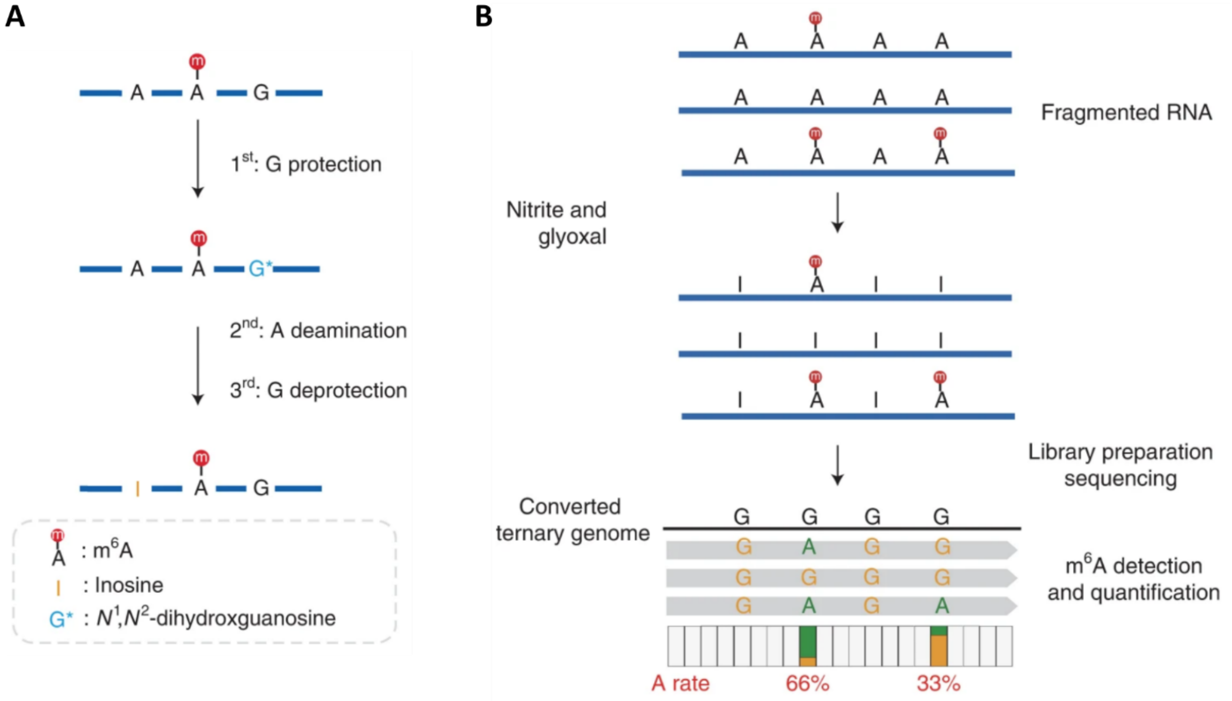

Fig. 4: Principle of GLORI-seq. A) mRNA is initially treated with glyoxal and boric acid to protect guanosines from deamination. Sodium nitrite mediates the deamination of unmethylated adenosines. After the deamination reaction, guanosines are recovered under heat and alkaline conditions. **B)** Fragmented mRNA is treated with glyoxal and nitrite to induce efficient deamination of unmethylated adenosines. Sequencing libraries can then be generated using a standardized protocol. The resulting sequencing reads are aligned to a ternary genomic reference, and the “A rate” is calculated for each site, reflecting the m^{6}A methylation level. This figure was modified from Liu *et al*., 2023 [27].

1.4 The role of METTL3 in cancer and its therapeutic potential

Given the central regulatory role of m^{6}A in RNA metabolism, its dysregulation has been implicated in various pathophysiological processes, including cancer development [104]. In multiple cancers, altered m^{6}A methylation signatures and aberrant expression patterns of the m^{6}A regulatory proteins have been described to promote cancer initiation, progression, and metastasis via the dysregulation of target transcripts and their downstream pathways [105,106]. Although roles for the entire m^6A machinery have been described in cancer, this study focuses on the role of METTL3, with particular emphasis on UCB.

1.4.1 The therapeutic potential of METTL3 inhibition in human cancers

Across hematologic malignancies and solid tumors, METTL3 has predominantly been characterized as tumor-promoting, except in endometrial and kidney cancers, where tumor-suppressive roles have been reported. Its role in bladder, breast, colorectal, and thyroid cancers remains controversial, with evidence for both tumor-promoting and tumor-suppressive functions (Tab. 1) [56].

Tab. 1: Described roles of METTL3 in selected cancers. Representative studies were cited as references. This table was modified from Koch and Lyko, 2024 [56].

Entity	Tumor-promoting	Tumor-suppressing	Reference
Acute myeloid leukemia	X		107
Cervical cancer	X		108
Gastric cancer	X		109
Head and neck cancer	X		110
Liver cancer	X		111
Lung cancer	X		112
Melanoma	X		113
Pancreatic cancer	X		114
Prostate cancer	X		115
Ovarian cancer	X		116
Bladder cancer	X	X	117 (Oncogene), 118 (Suppressor)
Breast cancer	X	X	119 (Oncogene), 120 (Suppressor)
Colorectal cancer	X	X	121 (Oncogene), 122 (Suppressor)
Thyroid cancer	X	X	123 (Oncogene), 124 (Suppressor)
Endometrial cancer		X	125
Kidney cancer		X	126

Given its predominantly tumor-promoting activity across many cancers (Tab. 1), METTL3 has emerged as a potential therapeutic target. In AML, inhibition of METTL3 using the small molecule STM2457 attenuated leukemic cell oncogenic phenotypes. Mechanistically, STM2457 reduced m^6A levels on leukemogenic transcripts, thereby suppressing their expression and translation. Additionally, METTL3 inhibition impaired engraftment and extended survival in a leukemia mouse model, with no notable adverse effects observed [127]. In small cell lung cancer, pharmacological inhibition of METTL3 was also found to reduce the oncogenic phenotype of cancer cells and to reverse chemoresistance at concentrations tolerable for healthy lung epithelial cells [128]. Further studies reported similar therapeutic effects in osteosarcoma [129], intrahepatic cholangiocarcinoma [130,131], and hepatocellular carcinoma [132]. Recently, several studies also described a role for METTL3 in cancer immunotherapy. The global reduction of m^6A methylation levels in human ovarian and mouse breast cancer cell lines by the METTL3 inhibitor STM3006 led to the formation of double-stranded RNA, which activated the RIG-I-like receptor, thereby triggering a cell-intrinsic interferon response. METTL3 inhibition increased the killing of tumor cells *in vitro*, mediated by enhancing the potency of CD8+ T cells. In immunocompetent mouse models of hematologic and solid cancers, METTL3 inhibition was as effective as PD-1 blockade, and the combination of both treatments outperformed either monotherapy [133]. METTL3 was also shown to promote hepatocellular carcinoma arising from nonalcoholic fatty liver disease by limiting intratumoral CD8+ T-cell infiltration. The combination of STM2457 and anti-PD-1 therapy restored CD8+ T-cell infiltration and induced tumor regression [134]. In colorectal and non-small-cell lung cancers, METTL3 has been described to contribute to an immunosuppressive tumor microenvironment defined by the accumulation of myeloid-derived suppressor cells and diminished CD4+ and CD8+ T-cell function. METTL3 inhibition reprogrammed the microenvironment to enhance effector immune cell infiltration and amplified responses to anti-PD-1 therapy [135,136].

Taken together, these findings establish METTL3 as a regulator of antitumor immunity and strengthen the rationale for METTL3 inhibitor-based therapeutic strategies. Of note, preliminary data from an ongoing Phase I clinical trial of the METTL3 inhibitor STC-15 in patients with advanced malignancies showed good tolerability across pharmacologically active doses and evidence of clinical activity [137].

1.4.2 The conflicting role and therapeutic potential of METTL3 in UCB

Although METTL3 is broadly characterized as tumor-promoting, evidence in UCB is conflicting (Tab. 1). Several studies support tumor-promoting roles, yet at least one study reports tumor-suppressive activity.

METTL3 is frequently overexpressed in UCB [117,138]. In a cohort of 180 patients, high METTL3 protein expression predicted shorter survival [138], supporting an oncogenic role for METTL3 in UCB. On the molecular level, METTL3 was found to promote UCB progression and stemness via the AFF4/NF-κB/MYC signaling pathway, as elevated m^6A levels not only increased the stability of the oncogenic MYC mRNA [117], but also enhanced its expression and that of SOX2 through the modification of the AFF4 mRNA [139]. Furthermore, METTL3-dependent methylation of the ITGA6 integrin mRNA was shown to promote its translation efficiency and tumor cell migration [140], while methylation of the PD-L1 transcript led to mRNA stabilization, favoring UCB immune escape [141]. UCB progression and angiogenesis were also linked to METTL3-mediated TEK and VEGF-A mRNA m^6A methylation, which led to elevated PI3K/AKT signaling [142], and to METTL3-dependent methylation and stabilization of the BIRC5 transcript [143]. Interestingly, METTL3 can also initiate the decay of tumor suppressor mRNAs in an m^6A-dependent manner. Examples include the transcripts of CDCP1 [144,145], SETD7, and KLF4 [146]. METTL3 has also been shown to promote the maturation of pri-miRNAs 221/222 that act as inhibitors of the tumor suppressor PTEN [138]. Furthermore, an oncogenic METTL3-YTHDF2-RIG-I axis has been related to bladder cancer tumor immunity. RIG-I has been identified as a downstream target of YTHDF2, which has been shown to mediate the degradation of RIG-I target transcripts, thereby promoting immune evasion of UCB cells. The loss of YTHDF2 increased CD8+ T-cell infiltration and antitumoral activity *in vivo*, improving the efficacy of Bacillus Calmette-Guerin immunotherapy [147].

In a study reporting contradictory findings, it was shown that METTL3 somatic mutations, which impaired its methyltransferase activity, promoted UCB cell growth [118].

Consequently, the therapeutic potential of METTL3 for UCB patients requires careful evaluation. Since METTL3 has a unique role in RNA metabolism and in basic cellular functions, it is also crucial to determine whether it functions as a tumor-specific gene or represents a generally essential factor for cell viability. Notably, the knockout (KO) of METTL3 in mice, which caused a complete loss of m^6A methylation, led to early embryonic lethality [148]. Furthermore, it was shown that many presumable METTL3 KO cell lines are not viable, except when expressing aberrant, but catalytically active isoforms of METTL3. These data were supported by METTL3 dependency analyses using CRISPR/Cas9 screenings [149]. Taken together, these findings support the notion that METTL3 activity is required for cellular viability and that METTL3 appears as a pan-essential gene, at least in certain models.

1.4.3 Restricted knowledge about the UCB m^6A epitranscriptome

Knowledge about the UCB m^6A epitranscriptomic landscape remains limited. At the global level, a 2-3-fold increase in m^6A methylation has been reported in UCB tissue [117]. However, this evidence derives from a very small LC-MS/MS case series, in which two tumor samples were compared against two paratumoral samples, therefore limiting generalizability. At the transcript or nucleotide level, knowledge has been constrained by the field's reliance on error-prone antibody-dependent m^6A mapping methods [76,79]. These approaches enabled the identification of m^6A effector-target axes (as described in section 1.4.2), but could not provide a quantitative, transcriptome-wide, base-resolution map of m^6A. Notably, one study applied direct RNA-seq to profile MIBC, but the results can only be considered preliminary due to the application of low-stringency cutoffs for coverage at m^6A candidate sites (> 2 reads) and for calling differential methylation ($p < 0.1$) [150]. Consequently, there is an urgent need for high-stringency, base-resolution, quantitative m^6A profiling in UCB to establish the first precise cancer m^6A epitranscriptome map, to resolve m^6A-dependent, cancer-associated pathways, and to elucidate the clinical potential of m^6A in cancer.

2 Aims

m^{6}A is the most abundant internal RNA modification in eukaryotic mRNA and has emerged as a key regulator of gene expression at the post-transcriptional level. In cancer, dysregulation of the m^{6}A machinery, particularly METTL3, has been implicated in both oncogenic and tumor-suppressive processes. In the context of UCB, however, the role of METTL3 remains poorly defined, with conflicting reports suggesting both tumor-promoting and tumor-suppressive functions.

Therefore, the first aim of this thesis was to reinvestigate the function of METTL3 in UCB. This included the generation and characterization of METTL3-deficient cell lines using functional *in vitro* assays and LC-MS/MS to assess global m^{6}A levels. Moreover, the clinical relevance of METTL3 was explored by evaluating the effects of METTL3 inhibition. Also, LC-MS/MS-based quantification was used to investigate global m^{6}A methylation levels in clinical patient samples.

The second aim of this study was to implement a robust, antibody-independent method for transcriptome-wide m^{6}A mapping. To overcome the resolution and quantification limitations of existing antibody-based techniques, GLORI-seq was implemented and optimized. This method is based on a chemical deamination protocol that enables base-resolution and quantitative detection of m^{6}A modifications across the transcriptome, providing a more accurate and reliable characterization of the m^{6}A epitranscriptome.

The final aim was then to use GLORI-seq to systematically compare the m^{6}A landscapes of UCB and paratumoral tissues. This analysis sought to identify cancer-associated m^{6}A signatures and to explore their potential biological and diagnostic relevance in the context of UCB.

Together, these aims were designed to advance our understanding of the functional relevance of m^{6}A in UCB and to provide novel insights into the epitranscriptomic reprogramming that accompanies malignant transformation in the bladder.

3 Results

3.1 Reevaluating the clinical relevance of METTL3 in UCB

3.1.1 METTL3 depletion impairs the oncogenic phenotype of UCB cells

For reinvestigating the potentially oncogenic or tumor-suppressive roles of METTL3 in UCB, I generated METTL3 scramble (Scr) and KO T24 and UM-UC-3 cell lines using the inducible TLCV2 system. 24 hours after doxycycline-mediated Cas9 enzyme induction, METTL3 protein levels were found to be strongly reduced (Fig. 5A). The METTL3 KO cell lines were subsequently characterized using several functional assays. The induced depletion of METTL3 caused a reduction in cell proliferation (Fig. 5B) and colony formation (Fig. 5C), while Caspase 3/7 activity assays suggested increased apoptosis signaling (Fig. 5D). Taken together, the METTL3 KO UCB cell lines were characterized by a reduced oncogenic phenotype. These results are consistent with previous findings [138,140,146] and question the reported tumor-suppressive functions in which, amongst others, METTL3 knockdown (KD) was shown to increase cell proliferation in T24 and 5637 UCB cells [118].

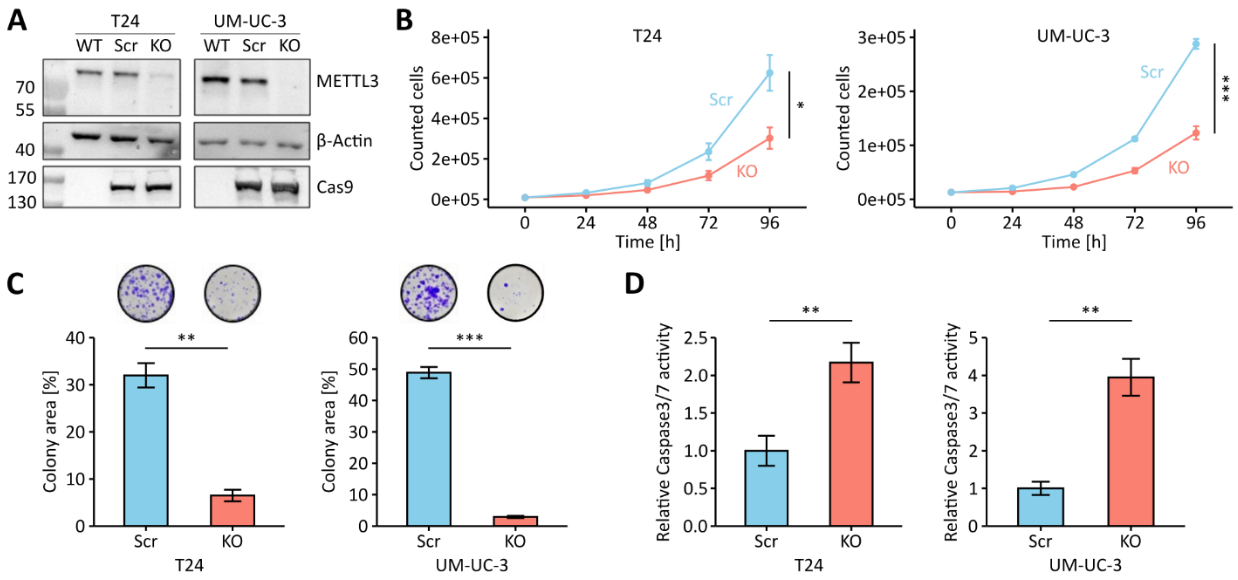

Fig. 5: METTL3 depletion reduces the oncogenic phenotype of T24 and UM-UC-3 cells. A) Western blot analysis of METTL3 protein levels in METTL3 KO and Scr cells 24 hours after Cas9 induction. **B)** Cell proliferation of METTL3 KO and Scr cells. *p < 0.05, ***p < 0.001, two-way analysis of variance. **C)** Colony formation results from METTL3 KO and Scr cells. **p < 0.01, ***p < 0.001, t-test. **D)** Caspase 3/7 activity measurements in METTL3 KO and Scr cells. **p < 0.01, t-test. TLCV2 Scr and METTL3 KO cell pools were analyzed.

3.1.2 METTL3 and m^6A are essential for the survival of UCB and uroepithelial cells

Next, the impact of METTL3 depletion on global m^6A RNA methylation levels was investigated by LC-MS/MS. All LC-MS/MS analyses were performed in collaboration with Dr. Martina Krämer and Prof. Dr. Mark Helm (Helm lab, Institute of Pharmaceutical and Biomedical Sciences, Johannes Gutenberg University, Mainz). Since total RNA is predominantly composed of rRNA, that is not methylated by METTL3 but METTL5, no or minor differences in m^6A methylation levels were detected in total RNA (Fig. 6A). The effect of altering METTL3 levels on RNA methylation is diluted if total RNA preparations are analyzed since METTL3 is a mRNA methyltransferase and mRNA make up approximately 5% of total RNA only. As expected, m^6A methylation levels were significantly decreased in mRNA that was isolated 24 hours after Cas9 induction (Fig. 6B). These data emphasize the importance of analyzing mRNA fractions whenever METTL3-modified cell lines are the subject of global m^6A methylation analyses. Furthermore, m_2^6A was measured in the RNA preparations, which represents an rRNA-specific modification. m_2^6A measurements can therefore be utilized as a quality control for the isolated mRNA fractions and used for the determination of the level of contaminating rRNA species. In the measurements, no significant differences in m_2^6A levels were observed (Fig. 6A and B), suggesting that the reported effects in m^6A mRNA methylation level reduction were reliable (Fig. 6B). Then, the reduction of m^6A mRNA methylation levels was monitored over a period of one week. Surprisingly, the methylation levels remained constant at the initially reduced level and did not decrease further (Fig. 6C and Suppl. Fig. 1). A further reduction was expected since METTL3 was shown to be responsible for more than 95% of the overall m^6A mRNA methylation levels [148]. These findings indicated a selection process ongoing in the pool of METTL3 KO cells, favoring subpopulations that still express catalytically active METTL3.

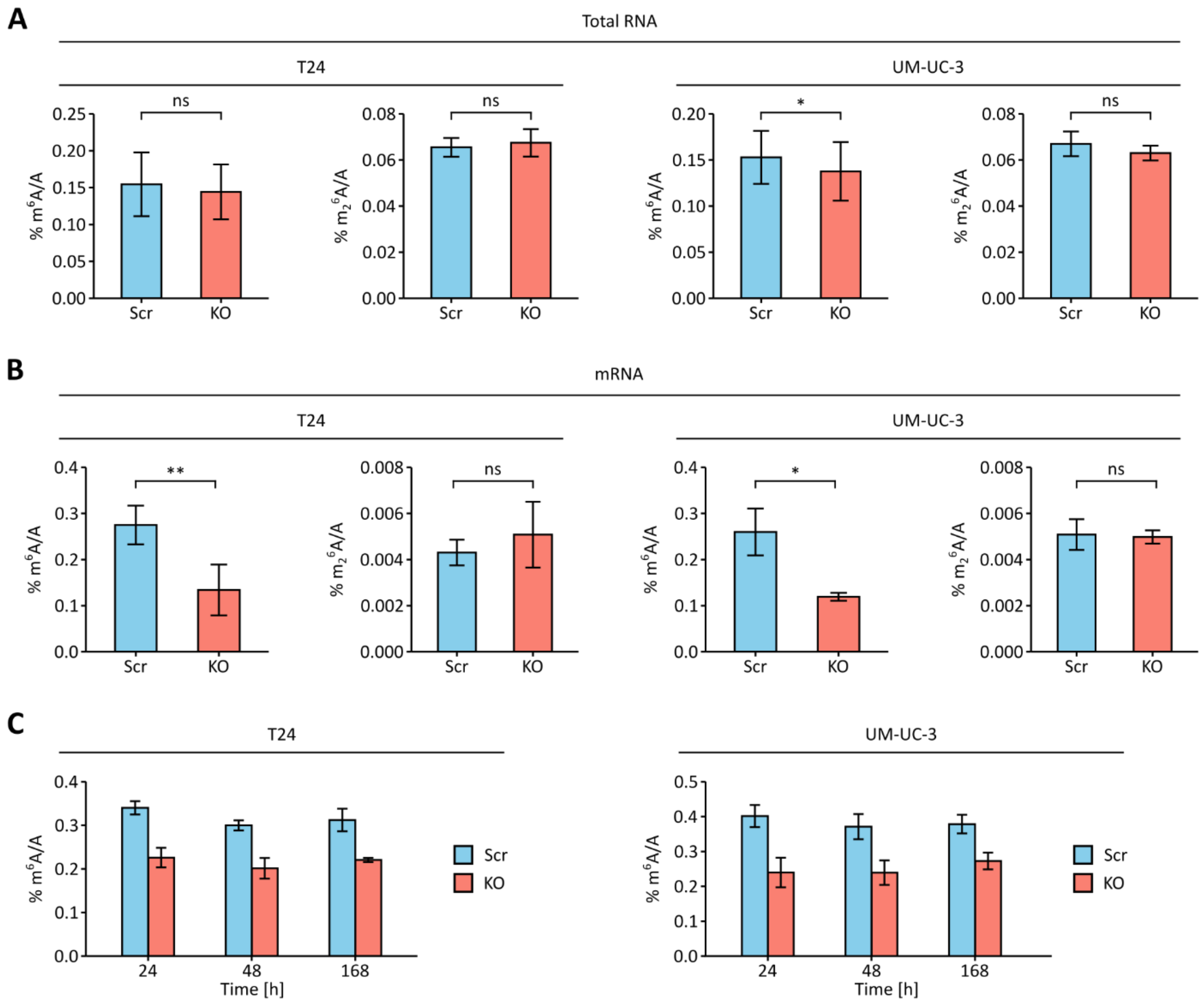

Fig. 6: METTL3 depletion causes a reduction in global m^{6}A mRNA methylation levels. A) Quantification of m^{6}A levels in total RNA from METTL3 KO and Scr cells 24 hours after Cas9 induction. ns = not significant, *$p < 0.05$, t-test. **B)** Quantification of m^{6}A levels in mRNA from METTL3 KO and Scr cells 24 hours after Cas9 induction. *$p < 0.05$, **$p < 0.01$, t-test. **A)** and **B)** Quantification of m$_2^6$A levels in total RNA and mRNA preparations to assess rRNA contaminants. ns = not significant, t-test. **C)** LC-MS/MS time course measurements of m^{6}A levels in mRNA from METTL3 KO and Scr cells. Technical triplicates were analyzed from two biological replicates. m$_2^6$A measurements for assessing the level of contaminating rRNA species are shown in Suppl. Fig. 1. LC-MS/MS analyses were performed in collaboration with Dr. Martina Krämer (Helm lab, Institute of Pharmaceutical and Biomedical Sciences, Johannes Gutenberg University, Mainz). TLCV2 Scr and METTL3 KO cell pools were analyzed.

To investigate these presumable selective forces, I screened multiple METTL3 KO clones generated using the pLentiCRISPR v2 system that allows for the constitutive expression of Cas9. Western blot screenings of T24 cells showed high variability between the clones. Several clones were found to still express the METTL3 wild type (WT) enzyme (Fig. 7A). Interestingly, in multiple lanes of T24 METTL3 KO clones, a novel immunoreactive band was detected that was not present in the T24 Scr lane (e.g., clones H, J, and M, Fig. 7A). This band represented a lower molecular weight (approximately 55 - 60 kDa) compared to the approximately 70 kDa of the METTL3 WT protein. Additionally, this band was observed in all UM-UC-3 clones (Suppl. Fig. 2A). It also seemed that some T24 METTL3 KO clones had a complete depletion for the METTL3 protein (e.g., clones B, C, and E, Fig. 7A). However, enhancing the contrast of the membrane image revealed that none of the clones had a complete KO of METTL3 (Suppl. Fig. 3). Next, clones showing strongest depletion of the METTL3 protein, including clones that were shown to express presumable METTL3 isoforms, were selected for LC-MS/MS experiments to assess their global m^6A mRNA methylation levels. The analyses confirmed that remaining m^6A mRNA methylation levels were detected in all clones (Fig. 7B and Suppl. Fig. 2B). The strongest reduction in m^6A levels was observed in T24 METTL3 KO clones C, L, and O, which showed a global relative reduction of 70% - 75% (Fig. 7B). In the screened UM-UC-3 METTL3 KO clones, a global relative reduction of 40% - 45% was observed (Suppl. Fig. 2B). No major differences in m_2^6A measurements were detected thereby indicating a similar degree of rRNA contamination in the corresponding mRNA preparations (Fig. 7B and Suppl. Fig. 2B). To assess if the METTL3 KO clones also show an impaired oncogenic phenotype like the already investigated cell pools (Fig. 5), three clones per UCB cell line were selected for different functional assays. All clones showed reduced cell proliferation and colony formation as well as increased Caspase 3/7 activity levels (Fig. 7C-E and Suppl. Fig. 2C-E). Taken together, these results suggest that some of the surviving clones bypassed the Cas9-induced KO of the METTL3 WT enzyme and expressed a presumable, shorter METTL3 isoform, which was reported recently for other cell lines [149]. Furthermore, my data indicate that the presumable METTL3 isoforms have catalytic activity and that METTL3 activity, as well as a minimum level of m^6A mRNA methylation, are required for the survival of T24 and UM-UC-3 cells.

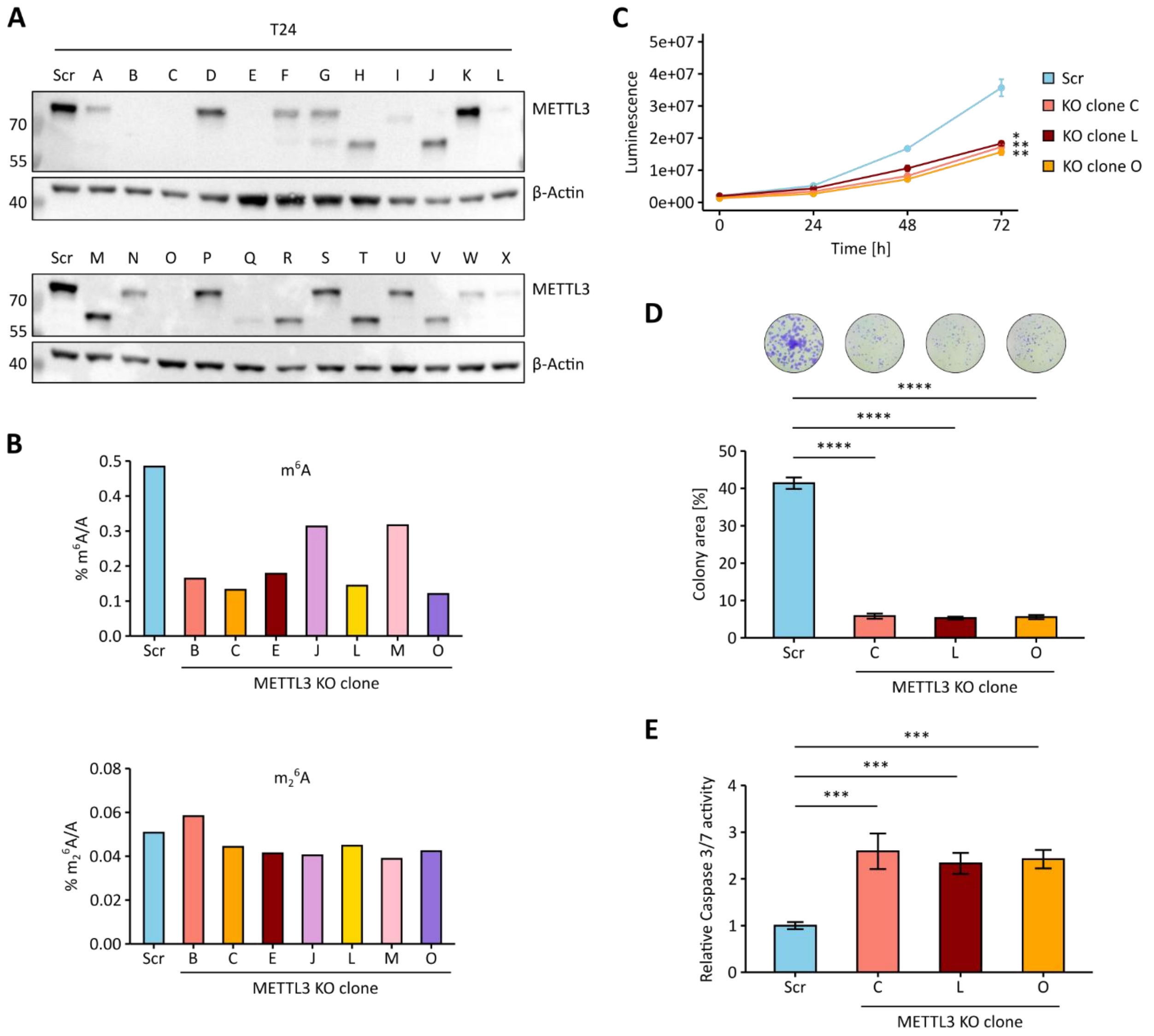

Fig. 7: METTL3 activity is essential for the viability of T24 cells. A) Western blot analysis of T24 METTL3 KO clones. For a membrane image with increased contrast, see Suppl. Fig. 3. **B)** LC-MS/MS quantification of m^6A levels in mRNA from selected T24 METTL3 KO clones. m_2^6A measurements for assessing the level of contaminating rRNA in mRNA preparations from T24 METTL3 KO clones. One biological replicate was analyzed per clone. LC-MS/MS analyses were performed in collaboration with Dr. Martina Krämer (Helm lab, Institute of Pharmaceutical and Biomedical Sciences, Johannes Gutenberg University, Mainz). **C)** Cell proliferation assays of T24 METTL3 KO clones and Scr cells. $^*p < 0.05$, $^{**}p < 0.01$, two-way analysis of variance. **D)** Colony formation assays of T24 METTL3 KO clones and Scr cells. $^{****}p < 0.0001$, one-way analysis of variance. **E)** Caspase 3/7 activity measurements in T24 METTL3 KO clones and Scr cells. $^{***}p < 0.001$, one-way analysis of variance. pLentiCRISPR v2 Scr and METTL3 KO clones were analyzed.

To further validate the role of METTL3 and, more importantly, to directly target its enzymatic function, I employed the METTL3 inhibitor STM2457. Pharmacological inhibition bypasses genetic compensation and allows for an unbiased interrogation of METTL3 catalytic dependency. LC-MS/MS analyses confirmed a relative reduction of m^6A mRNA levels of approximately 75% in T24 and UM-UC-3 cells upon METTL3 inhibition (Suppl. Fig. 4A). STM2457 treatment phenocopied the genetic KO, leading to dose-dependent reductions in cell proliferation, clonogenicity, and a dose-dependent increase in Caspase 3/7 activity (Fig. 8A-C). These results confirmed that the oncogenic effects of METTL3 in T24 and UM-UC-3 UCB cell lines depend on its methyltransferase activity. Notably, METTL3 protein levels were quantified upon STM2457 treatment to ensure that potential effects in the STM2457 response experiment are due to the disturbance of METTL3's methyltransferase activity and not induced by non-methyltransferase activities of the enzyme. Western blot analyses showed that METTL3 protein levels were upregulated in STM2457-treated T24 cells, likely due to cellular compensation mechanisms, while METTL3 levels remained unchanged in UM-UC-3 cells (Suppl. Fig. 4B).

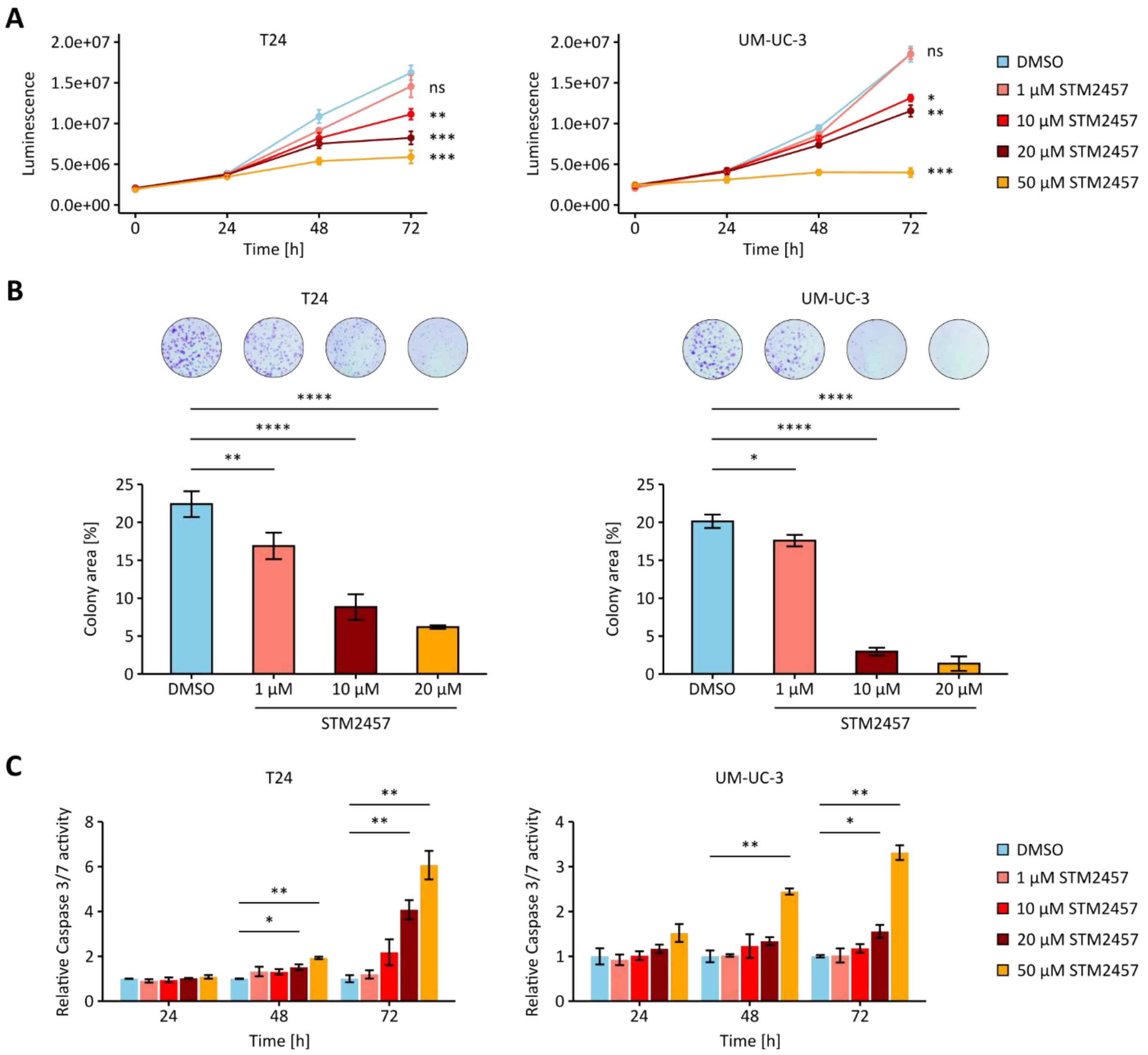

Fig. 8: STM2457 treatment phenocopies the genetic METTL3 KO in T24 and UM-UC-3 cells. A) Cell proliferation measurements of T24 and UM-UC-3 cells treated with DMSO and increasing concentrations of STM2457. ns = not significant, $^*p < 0.05$, $^{**}p < 0.01$, $^{***}p < 0.001$, two-way analysis of variance. **B)** Colony formation assays of T24 and UM-UC-3 cells following DMSO and STM2457 treatment using increasing concentrations. $^*p < 0.05$, $^{**}p < 0.01$, $^{****}p < 0.0001$, one-way analysis of variance. **C)** Caspase 3/7 activity measurements in T24 and UM-UC-3 cells treated with DMSO and increasing concentrations of STM2457. $^*p < 0.05$, $^{**}p < 0.01$, two-way analysis of variance. For visualization reasons, significant results are presented only. All other comparisons were not significant.

While the functional relevance of METTL3 was experimentally validated in the UCB cell lines T24 and UM-UC-3, I next sought to determine whether this dependency extends to additional UCB cell models and more broadly across other cancer types. Thus, I analyzed data from the Cancer Dependency Map (DepMap), which provides so-called dependency probability scores that represent a measurement of the likelihood that a given gene is essential for the viability of a given cell line. These scores are determined from genome-wide CRISPR/Cas9 KO screening data across hundreds of human cancer cell lines [151]. As such, a cell line is dependent on a gene if the gene's dependency probability score exceeds 0.5. Conversely, if the dependency probability score of a given gene is below 0.5, the gene is considered non-essential for the viability of that cell line. From the DepMap Public 22Q2 CRISPR gene dependency data set, dependency probability scores for METTL3, POLR2F (a known essential gene for cell viability), and DNMT2 (a known non-essential gene for cell viability) were extracted, and the score distributions were plotted for UCB cell lines and all other cell lines present in the data bank. The results showed that the majority of UCB and all other cancer cell lines had dependency probability scores greater than 0.5 for METTL3, suggesting that METTL3 has an essential character and is indispensable for cell viability in the majority of cell lines (Fig. 9A and B). These data support the notion that METTL3 is an essential gene for the viability of cancer cells.

Having established that METTL3 is required for UCB cell viability and oncogenic phenotype through both genetic KO and pharmacological inhibition, I next sought to assess the specificity and therapeutic potential of METTL3 inhibition in UCB. In particular, I aimed to determine whether the observed effects were selective to malignant cells or might also affect healthy uroepithelial cells. Thus, I performed an STM2457 response experiment in four UCB cell lines and one uroepithelial cell line. While all UCB lines exhibited dose-dependent sensitivity to STM2457, the uroepithelial UROtsa cell line showed a higher IC50, indicating lower sensitivity to METTL3 inhibition (Fig. 9C). However, the difference between UCB and uroepithelial IC50 values was modest, suggesting potential off-target or on-target toxicity in uroepithelial cells at high doses.

Taken together, the results suggest that uroepithelial cells depend on METTL3 activity for cell viability as well. The partial selectivity observed hints at the existence of a rather narrow therapeutic window. These findings highlight the importance of careful dose optimization and patient stratification for the clinical application of METTL3 inhibitors such as STM2457 in UCB. Moreover, the results reinforce the biological importance of METTL3 not only in cancer but also in the healthy epithelium, underscoring the need for context-dependent targeting strategies and possibly the development of tumor-selective delivery mechanisms to reduce toxicity.

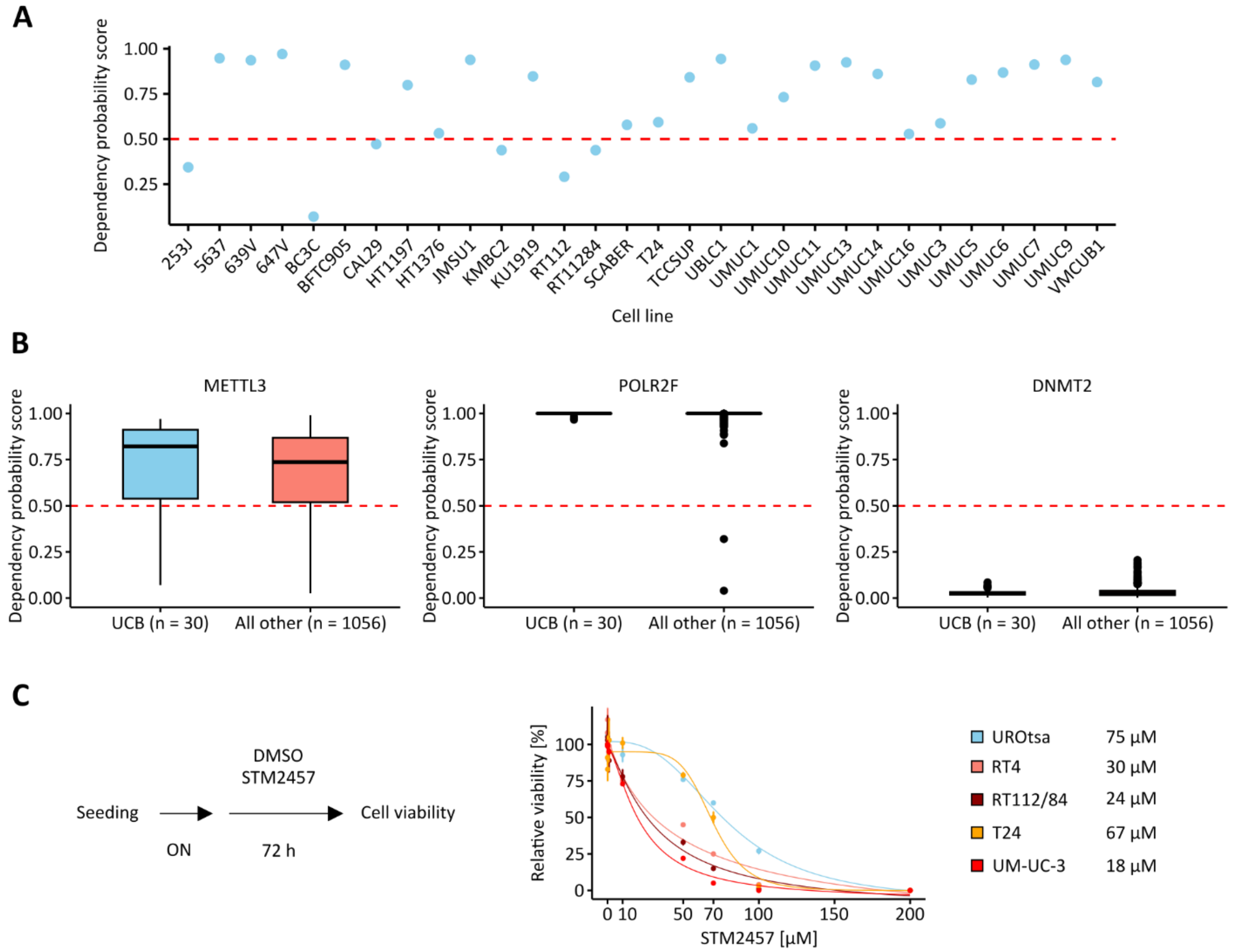

Fig. 9: UCB and uroepithelial cells rely on METTL3 activity for viability. A) Dependency probability scores for METTL3 in a panel of UCB cell lines based on DepMap data. **B)** Distribution of dependency probability scores for METTL3, POLR2F (essential gene control), and DNMT2 (non-essential gene control) in DepMap. **C)** STM2457 response curves of UCB and uroepithelial cell lines treated with DMSO or 0.01 - 200 µM STM2457 for 72 hours. IC50 values are shown next to the cell line labels. ON = attachment of cells overnight.

3.1.3 METTL3 upregulation does not increase global m^{6}A levels

Given these observations in METTL3-deficient UCB cell lines, I next asked whether METTL3 is also dysregulated in patient tumors, as this could reflect a clinically relevant role in UCB. Previous studies have reported that METTL3 expression is upregulated in UCB compared to normal uroepithlium [117,138]. Additionally, LC-MS/MS results suggested an increase in global m^{6}A methylation levels in UCB, although these findings were based on only two samples [117]. Therefore, I aimed to obtain a more reliable assessment of global m^{6}A methylation levels in

UCB by conducting the same analysis on a larger cohort of patient samples. Consequently, 20 tumoral and corresponding paratumoral control tissue samples were analyzed in LC-MS/MS experiments. The clinicopathological data from this cohort are listed in Tab. 2. LC-MS/MS analyses showed a significant decrease in m^6A mRNA methylation levels in UCB tissues, while m_2^6A methylation levels did not significantly differ in quality control measurements (Fig. 10). Global hypomethylation of approximately 70% - 85% were observed in the most extreme cases (Fig. 10). As such, an overexpression of METTL3 in UCB does not consequently lead to an increase in m^6A mRNA methylation levels.

Tab. 2: Clinicopathological information of the LC-MS/MS cohort.

Clinical data	Attribute	LC-MS/MS cohort (n = 20)
Sex	male	15
	female	5
Age	mean	68.85
	min - max	48 - 79
Tissue	n (tumoral)	20
T-stage	Tis	0
	T1	3
	T2	5
	T3	9
	T4	3
N-stage	N0	14
	N+	6

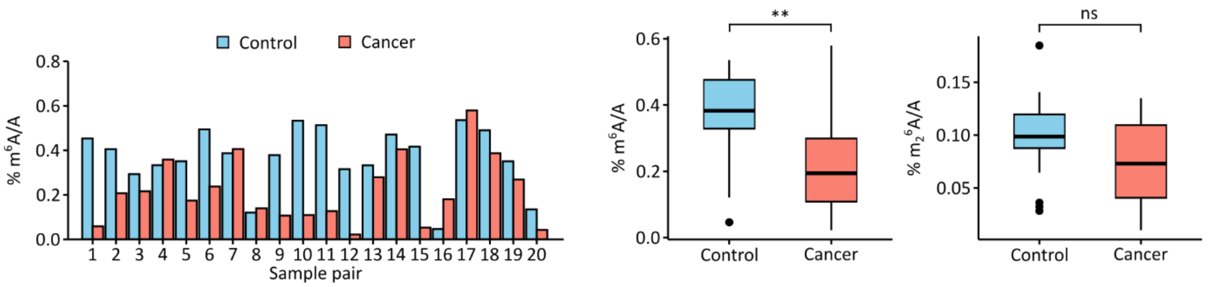

Fig. 10: m^6A methylation levels are decreased in UCB compared to paratumoral tissue. LC-MS/MS quantification of global m^6A levels in mRNA from paired UCB and paratumoral tissues (n = 20). m_2^6A measurements from the same mRNA preparations are included to assess rRNA contamination. ns = not significant, $**p < 0.01$, Mann-Whitney-U test. LC-MS/MS analyses were performed in collaboration with Dr. Martina Krämer (Helm lab, Institute of Pharmaceutical and Biomedical Sciences, Johannes Gutenberg University, Mainz).

Taken together, the role of METTL3 in UCB remains difficult to interpret. Cell-based assays and published METTL3 expression analyses suggest a tumor-promoting role for METTL3 in UCB. Additionally, the clinical potential of the enzyme might lie in biomarker development due to its observed upregulation in UCB compared to paratumoral tissues. Nevertheless, dependency analyses indicated that METTL3 is essential not only for the viability of UCB cell lines but also for uroepithelial cells, which has been consistently reported in other cellular contexts [149]. These observations narrow the therapeutic window for METTL3-interfering drugs and raise the possibility that cancers escape treatments by expressing aberrant METTL3 isoforms. Furthermore, the overexpression of METTL3 does not result in increased global m^6A mRNA methylation. Consequently, the use of METTL3 inhibitors in UCB treatment, which would presumably cause a global decrease in m^6A mRNA methylation, must be questioned and carefully evaluated.

3.2 Implementation of GLORI-seq for quantitative, base-resolution m^{6}A mapping

GLORI-seq is a glyoxal and sodium nitrite-assisted, conversion-based RNA-seq technique that discriminates unmethylated adenosines from m^{6}A to allow its transcriptome-wide detection and quantification [27].

Initially, the efficiency of the sodium nitrite and glyoxal-mediated deamination of adenines was tested using a synthetic RNA oligo. Deaminated or untreated GLORI-PCR amplicons were sent for Sanger Sequencing and revealed complete conversion of adenines into guanines (Fig. 11).

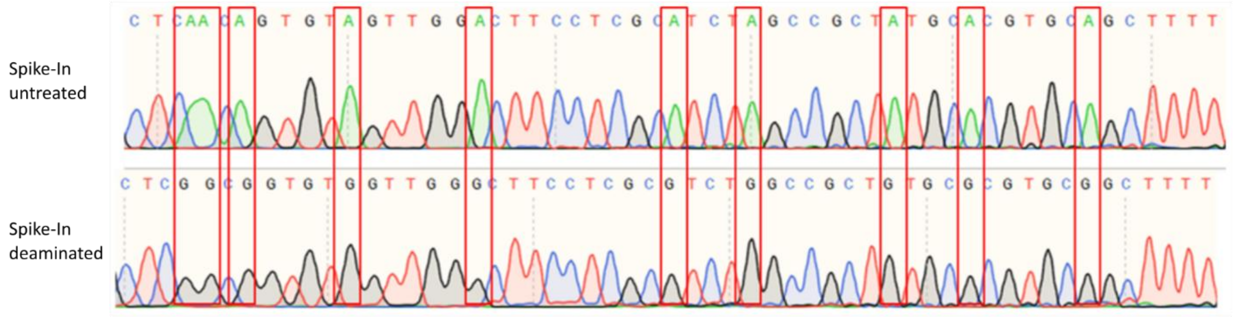

Fig. 11: Assessment of deamination efficiency by GLORI-PCR. A synthetic RNA oligo (later used as Spike-In control for sequencing) was either left untreated or deaminated. Oligos were reverse-transcribed and PCR-amplified. Amplicons were then analyzed by Sanger Sequencing. A representative example is shown.

For the generation of the first cellular mRNA GLORI-seq libraries, HEK293T cells were used as a model for comparability to the published data that were also obtained from the same cell line [27]. Concerning RNA preparation prior to the deamination treatment, total RNA was isolated, small RNA species (< 200 nt) eliminated, and mRNA enriched via two consecutive rounds of oligo-dT beads. mRNAs were further fragmented to resolve RNA secondary structures that potentially shield conversion (Fig. 12A). Fragmented mRNAs were then subjected to sodium nitrite and glyoxal-mediated deamination, and GLORI-seq libraries were prepared. Initially, I faced several problems in removing sequencing adaptor dimers and in generating a sufficient number of sequencing-competent molecules. Sequencing adaptor dimers represent a common problem in the preparation of sequencing libraries, as they contain full-length adaptor sequences that enable them to bind to and cluster on the sequencing flow cell. Thus, sequencing adaptor dimers are sequenced, generate unwanted sequencing data, and reduce the amount of sequencing reads from the library molecules of interest, depending on their quantitative proportion relative to the library molecules. Due to their smaller size of approximately 120 bp, they also cluster more efficiently than the longer library molecules and therefore subtract binding spots on the sequencing flow cell. Causes for the formation and contamination by adaptor dimers comprise insufficient amounts of starting material, quality of the starting material, including degraded nucleic acids or poor RNA 5' end 3'-end labelling for sequencing adaptor attachment, and insufficient library clean-up [152]. For troubleshooting the contamination of libraries with adaptor dimers, new enzymes and ATP for 5' RNA phosphorylation and 3' RNA dephosphorylation (RNA end labelling for attachment of sequencing adaptors) were purchased and tested against the existing lab stock (in use for more than one year). Furthermore, 6% TBE-PAGE gels were compared to 8% TBE-PAGE gels during size-selection of the sequencing libraries for a potentially better separation of the library molecules (160 - 250 bp) and the adaptor dimers (approximately 120 bp). TBE-PAGE analyses confirmed the presence of adaptor dimers in both tested conditions (new reagents for end labelling and 8% TBE-PAGE versus old reagents for end labelling and 6% TBE-PAGE, Fig. 12B). Gel extraction and subsequent TapeStation analyses showed that adaptor dimers (123 bp peak) were predominantly present in the condition “old reagents and 6% TBE-PAGE”, which would result in an over-estimation of the desired library molecules (177 bp peak) concentration (Fig. 12C, upper panel). TapeStation chromatography of the “new reagents and 8% TBE-PAGE” condition revealed the successful depletion of adaptor dimers and an increase in the concentration of the library molecules (Fig. 12C, lower panel), thereby confirming that RNA 5' and 3'-end labelling and library clean-up affect the amount and contamination level of sequencing adaptor dimers. Besides RNA end labeling and library purification, the impact of RNA fragmentation on the concentration of library molecules was also tested. An mRNA fragmentation time course and TapeStation analysis showed a time-dependent decrease in RNA fragment length as expected (Fig. 12D). After deamination and library preparation, the libraries were analyzed via TapeStation. The analysis showed that the fragmentation time does not affect the average fragment length of the libraries. However, the yields of the libraries decreased with longer fragmentation times (Fig. 12E). To investigate the impact of RNA fragmentation on deamination efficiency, the libraries were then sequenced on a MiSeq platform. It was found that different fragmentation times only slightly affected the conversion ratios. Fragmentation of mRNAs for 2 - 3 min returned slightly better conversion ratios (Tab. 3). For these reasons, subsequent mRNA fragmentations were performed for 3 min at 94 °C to ensure (i) sufficient fragmentation for dissolving RNA secondary structures and (ii) higher conversion.

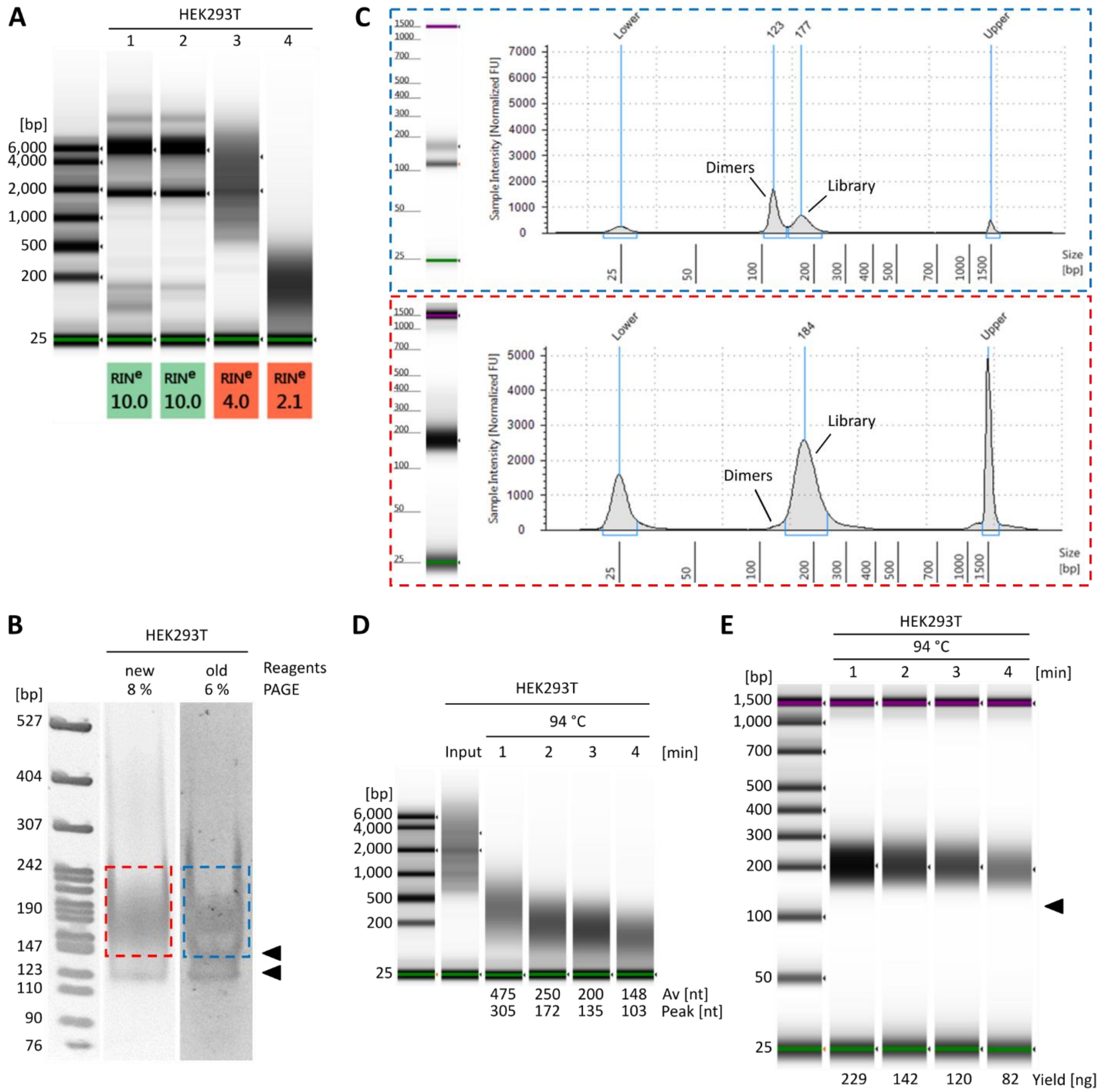

Fig. 12: Troubleshooting the preparation of GLORI-seq libraries. A) Workflow of RNA preparation prior to deamination. 1) Isolation of total RNA. 2) Depletion of small RNA fractions < 200 nt. 3) Enrichment for mRNA. 4) Fragmentation of mRNA. Here, mRNA was fragmented for 3 min at 94 °C. **B)** TBE-PAGE analyses comparing different protocols for RNA 5’ and 3’-end labeling as well as library size-selection. Adaptor dimer contaminants (approximately 120 bp) are marked by the triangle. Dashed lines indicate the cut area for gel extraction and subsequent TapeStation analysis. Representative examples are shown. **C)** TapeStation analyses of the gel-extracted libraries from B). Libraries highlighted in blue and red illustrate differences in adaptor dimer content and overall library signal intensity. **D)** mRNA fragmentation time course analyzed by TapeStation, showing fragment length distributions at different fragmentation times. Average and peak fragment lengths are indicated. **E)** TapeStation analysis of the libraries prepared from the fragmentation time course samples shown in D). Fragmentation-dependent differences in library yields are shown. The theoretical position of adaptor dimers is indicated by a triangle.

Tab. 3: The impact of mRNA fragmentation on conversion ratio. Conversion ratios of mRNA samples fragmented for different time periods. The samples were deaminated using 375 mM $NaNO_2$ and 20 mM MES.

Fragmentation	**Total reads**	**Mapping efficiency [%]**	**Loci**	**Coverage threshold**	**Filtered loci**	**Median conversion [%]**
1 min, 94 °C	166,499	42	mRNA	15	2,125	96
			Spike-In		17	98
2 min, 94 °C	122,351	40	mRNA	15	1,561	97
			Spike-In		15	98
3 min, 94 °C	110,918	40	mRNA	15	1,338	97
			Spike-In		17	98
4 min, 94 °C	65,980	42	mRNA	15	837	96
			Spike-In		11	97

In comparison to the > 98% conversion ratios achieved in the published paper [27], obtained conversion ratios ranged between 96% - 97% for cellular mRNA samples from HEK293T cells (Tab. 3). After feedback from Weiguo Shen, co-author of the published paper [27], it turned out that the published deamination protocol was misinterpreted. In the published study, the deamination reaction is described as “Fifty microliters of deamination buffer was prepared per sample containing 750 mM $NaNO_2$ (Sigma-Aldrich, 31443), 40 mM MES (pH 6.0), 10 µL glyoxal solution (8.8 M in H2O) and nuclease-free water. The 50 µL sample was added to premixed deamination buffer and gently pipetted ten times. The tubes were incubated for 8 h at 16 °C.” [27]. According to my interpretation, the deamination buffer was prepared containing 750 mM $NaNO_2$ and 40 mM MES, resulting in a final concentration of 375 mM $NaNO_2$ and 20 mM MES in the final 100 µL deamination reaction. However, the authors performed the 100 µL deamination reaction using a final concentration of 750 mM $NaNO_2$ and 40 mM MES, meaning that the deamination buffer should contain 1.5 M $NaNO_2$ and 80 mM MES. To investigate if the different deamination protocols affect the conversion ratios, two DMSO-treated and two STM2457-treated HEK293T samples were deaminated and GLORI-seq libraries prepared. The libraries were sequenced on a MiSeq platform. Similar amounts of reads were obtained for both deamination protocols (Fig. 13A), while the mapping efficiency of the 750 mM $NaNO_2$, 40 mM MES was reduced (Fig. 13B). Most importantly, conversion ratios for the Spike-In and mRNAs were found to be increased in the 750 mM $NaNO_2$, 40 mM MES deamination protocol and ranged between 98% - 99% for the Spike-In RNA. mRNA samples showed a median conversion of 100% (Fig. 13C and D). These results are comparable to the published data [27]. Also, the higher conversion ratios obtained in the 750 mM $NaNO_2$ and 40 mM MES deamination protocol potentially explain the observed lower mapping efficiency, as these libraries lose complexity, which impedes read mapping (Fig. 13B). Consequently, further deamination reactions were conducted using the 750 mM $NaNO_2$, 40 mM MES protocol. To prove that GLORI-MiSeq could detect published m^6A sites [27], the methylation levels of individual m^6A sites were investigated. The analysis showed that the detected methylation levels were comparable to the methylation levels obtained in the published data set [27] (Fig. 13E). m^6A methylation levels were found to be reduced in the STM2457-treated samples, thereby supporting the notion that the detected m^6A sites were true positives (Fig. 13E). Note that the MiSeq platform returns a theoretical maximum of 1.5 million reads, resulting in low coverage for the selected m^6A sites, ranging between 5 - 15. This analysis should therefore just provide a preliminary test for the validation of the GLORI implementation.

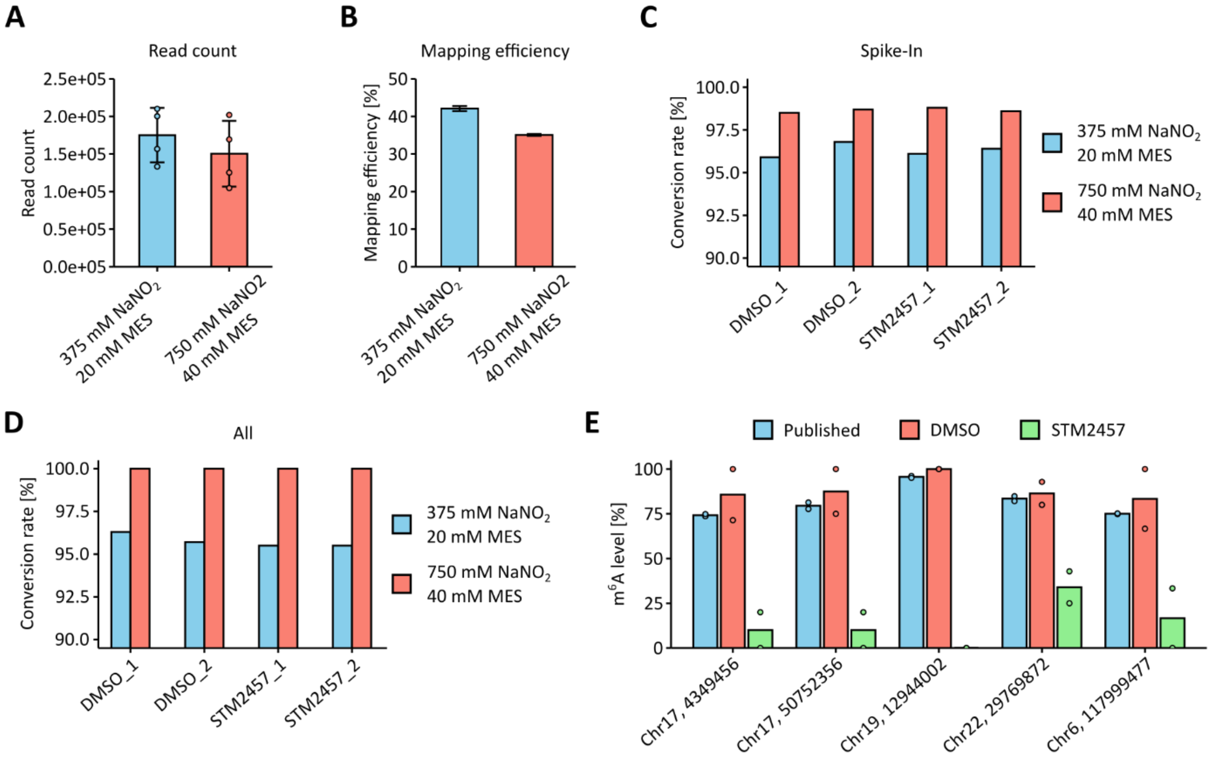

Fig. 13: Testing different deamination protocols for conversion ratio optimization. A) Total read counts obtained from libraries processed with the two deamination protocols. The MiSeq platform has a theoretical maximum output of 1.5 million reads, and more than 1.1 million reads were obtained across libraries. **B)** Mapping efficiencies of libraries generated using the two deamination conditions. **C)** Median conversion ratios calculated for the Spike-

In RNA samples. **D)** Median conversion ratios calculated for cellular mRNA samples. **E)** Quantitative mapping of individual m^{6}A sites in DMSO-treated and STM2457-treated samples. Published methylation levels are included for comparison [27].

3.3 Validation of GLORI-seq

3.3.1 GLORI reproduces published m^{6}A data in HEK293T cells

After implementing GLORI-seq, I next sought to validate the technique by reproducing the published results from the original study and to technically cross-validate GLORI using direct RNA-seq.

To do so, I sequenced three replicates of HEK293T cells by GLORI-seq, and one replicate of the same cell line by direct RNA-seq. For the GLORI-sequenced HEK293T cell replicates, an average of 200 million sequencing reads were generated from which 50% could be mapped for further analyses (Suppl. Tab. 1). Importantly, median A→G conversion ratios of > 99% were obtained (Suppl. Tab. 2), which is similar to the reported conversion ratios and limits the detection of false-positive sites [27]. In total, 69,748 m^{6}A sites were detected in the intersection of the transcriptomes of the three HEK293T cell replicates (Fig. 14A). The majority (86.8%) of these sites overlapped with previously reported sites (Fig. 14B), with differences likely attributable to the higher sequencing depth in the original study [27]. Additionally, the quantification of methylation levels was reproducible across the three replicates (Fig. 14C) and consistent with the mean methylation levels reported in the original study (Fig. 14D). To technically cross-validate my findings from GLORI, I pooled the RNA samples from the three HEK293T cell replicates and sequenced them as one replicate by direct RNA-seq. In total, 47,040 m^{6}A sites were detected. Most of those sites were also detected in the original GLORI data set (71.5%) as well as in my GLORI data set (58.4%, Fig. 14E). Also, the quantified methylation levels of the detected sites were highly similar when comparing the direct RNA-seq and the two GLORI data sets (Fig. 14F).

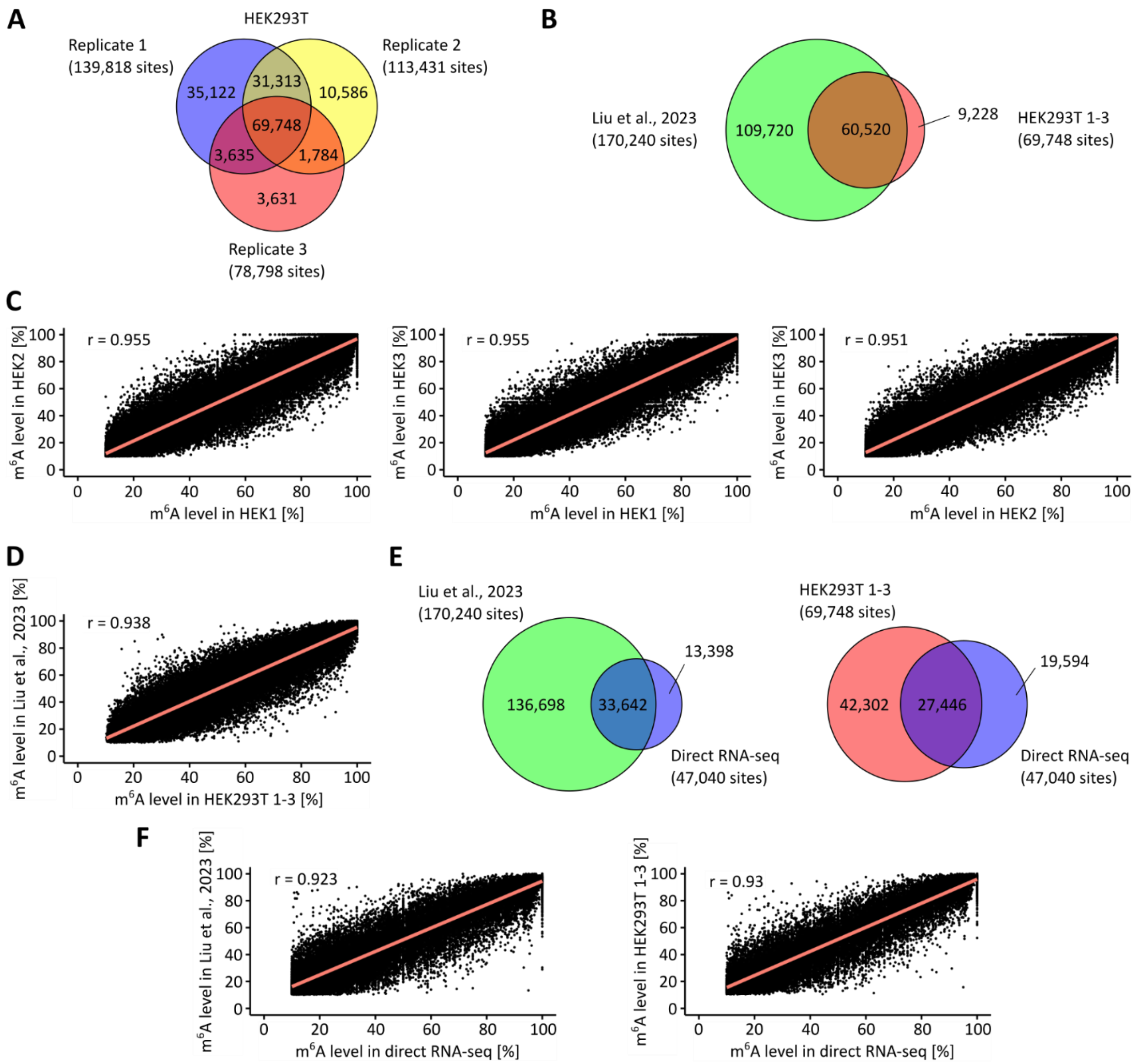

Fig. 14: Reproducible m^6A site detection in HEK293T cells using GLORI and direct RNA-seq. A) Number of m^6A sites detected by GLORI in the intersection of three HEK293T biological replicates. **B)** Proportion of these sites that overlap with the m^6A sites reported in the original study. **C)** Comparison of quantified m^6A levels across the three replicates. **D)** Comparison of mean m^6A levels from the m^6A sites detected in the present study and those reported in the original study. **E)** Overlap of m^6A sites identified by direct RNA-seq with sites from the original study and the present data set. **F)** Comparison of quantified m^6A levels obtained by direct RNA-seq and GLORI. Direct RNA-seq analyses were performed in collaboration with Dr. Panagiotis Provataris (German Cancer Research Center, Heidelberg).

To further validate the reproducibility of GLORI, I then described the quantitative landscape of m^6A in HEK293T cells, as it was done in the original study [27]. To robustly differentiate between genuine methylation signals and low-level deamination artifacts, a computational pipeline for methylation calling was developed. In an initial step, the approximately 70,000 shared m^{6}A sites detected by GLORI were subjected to a sequence motif analysis. This revealed that the m^{6}A sites predominantly occur in the DRAC(H) consensus sequence motif (Fig. 15A). Within the 15 most frequent pentanucleotide motifs, canonical DRAC(H) motifs were strongly overrepresented (Fig. 15B). Also, higher and more evenly distributed m^{6}A methylation levels were detected in the DRAC(H) motifs, while the non-canonical motifs were rather lowly methylated (Fig. 15C). Based on these observations, I considered the m^{6}A sites in DRAC(H) motifs as high confidence methylation marks and restricted all HEK293T downstream analyses to m^{6}A sites detected in DRAC(H) consensus sequence motifs. This revealed that two-thirds of all transcripts in the HEK293T transcriptome were m^{6}A-methylated (Fig. 15D). Longer transcripts were found to contain more m^{6}A sites and to be characterized by higher overall methylation levels (Fig. 15E). The majority of transcripts in HEK293T cells harbored one m^{6}A site, but several transcripts were also found to have multiple m^{6}A sites. The transcript with the most m^{6}A sites was the proliferation marker MKI67 with 87 m^{6}A sites (Fig. 15F). Overall, methylated DRAC(H) motifs showed a bimodal methylation distribution with peaks at 20% and 95% methylation (Fig. 15G) and a median methylation level of 45% (Fig. 15H). Meta gene plots showed that the majority of m^{6}A sites were located in the CDS and 3'-UTR of the transcripts with a characteristic peak around the stop codon (Fig. 15I). This characteristic distribution was also observed for MKI67, for which most m^{6}A sites were detected in a long internal exon and the 3'-UTR of the transcript (Fig. 15J).

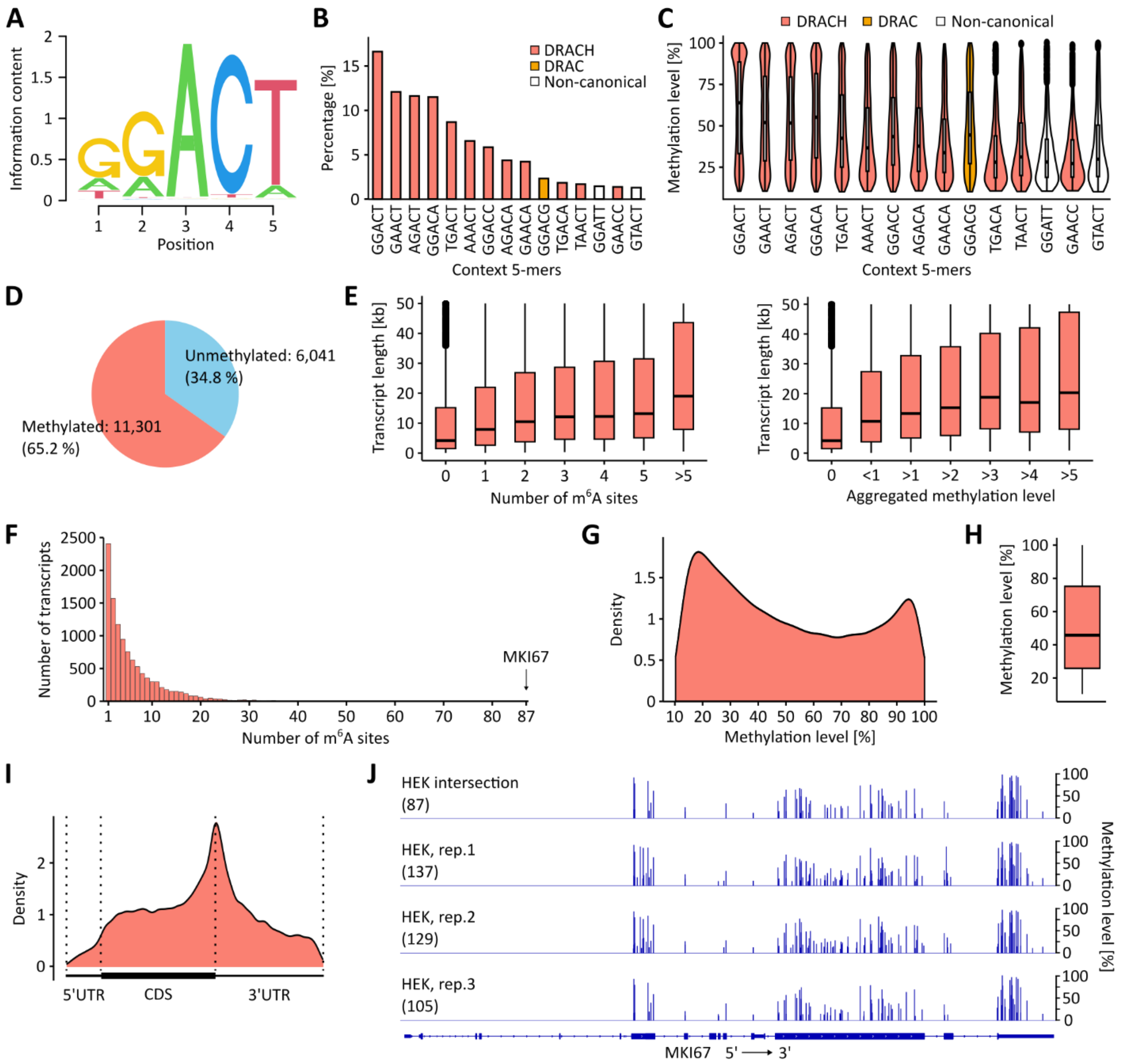

Fig. 15: Reinvestigation of the HEK293T cell m^{6}A landscape. A) Sequence logo representation of the consensus motif surrounding detected m^{6}A sites. **B)** Frequencies of the 15 most observed sequence motifs among detected m^{6}A sites. **C)** m^{6}A level distributions for the 15 most frequently detected sequence motifs. **D)** Proportion of HEK293T transcripts containing at least one detected m^{6}A site. **E)** Relationship between transcript length and the number of detected m^{6}A sites, as well as between transcript length and aggregated methylation level. Note that the y-axes of both plots are restricted to a transcript length of 50 kb. Data points above this limit are displayed in a squished manner. **F)** Distribution of m^{6}A site counts per transcript. With 87 m^{6}A sites, MKI67 represented the transcript with the highest number of detected sites. **G)** Kernel density plot showing a bimodal methylation level distribution for m^{6}A sites. **H)** Distribution of m^{6}A levels, with the median indicated. **I)** Metaplot showing the positional distribution of detected m^{6}A sites across transcript features. **J)** IGV browser visualization of m^{6}A sites detected in the MKI67 transcript, showing individual replicate tracks and their intersection. The number of detected m^{6}A sites is indicated in brackets.

The original study also reported that m^6A sites tend to form clusters within the transcriptome. Clustered sites were shown to have higher methylation levels than non-clustered sites and to preferentially occur near stop codons [27].

When I analyzed the distances between neighboring m^6A sites, I found that m^6A sites indeed tend to cluster within regions of 50 to 100 bp compared to random adenosines that were used as a control (Fig. 16A). Most of the detected clusters were rather short in length and harbored few m^6A sites, but also longer clusters with up to 19 m^6A sites were identified (Fig. 16B). In general, I found two-thirds of the detected sites in clusters (Fig. 16C), which is substantially more than in the original study in which the authors described that one-third of the m^6A sites were found in clusters [27]. Clustered m^6A sites were characterized by higher methylation levels (Fig. 16D and E) and by an enrichment near stop codons (Fig. 16F) when compared to non-clustered sites. The higher fraction of clustered m^6A sites in my data set compared to the original study is likely explained by differences in sequencing depth. Due to lower coverage, my analysis preferentially detected sites with higher methylation levels, particularly those within clusters, while lowly methylated, non-clustered sites were likely underrepresented, leading to an overestimation of clustered m^6A site frequency.

Taken together, these results are comparable to those obtained in the original study, which validates my implementation of GLORI and supports the notion that GLORI-derived data are reproducible and consistent among studies.

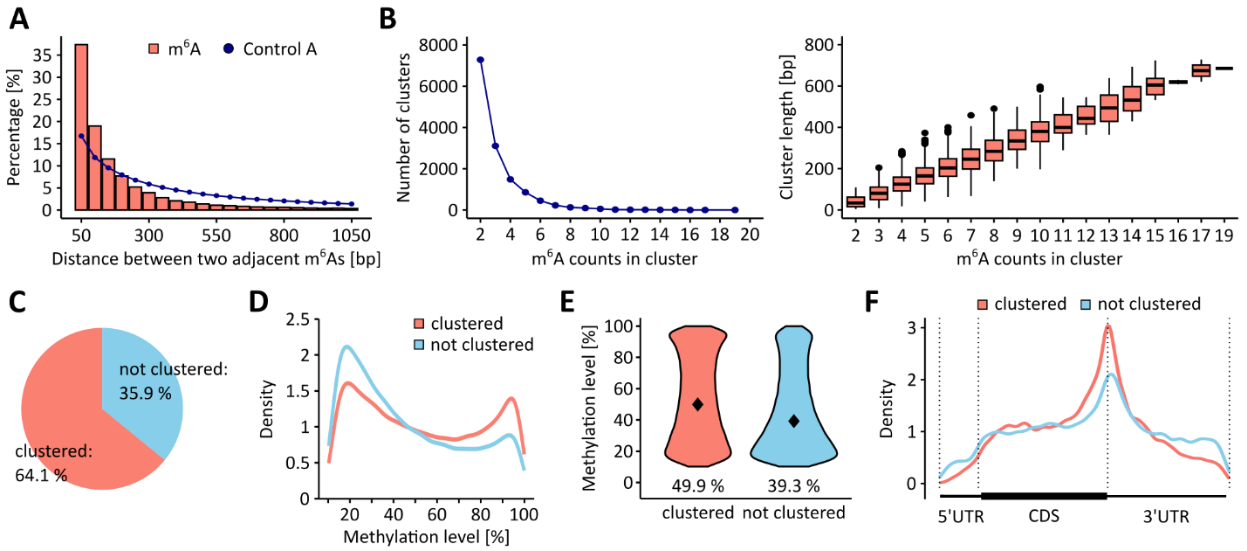

Fig. 16: m^{6}A shows the tendency to form clusters in the transcriptome of HEK293T cells. A) Distribution of distances between neighboring m^{6}A sites, illustrating clustering within regions of approximately 50 - 100 bp. **B)** Number of m^{6}A sites per cluster and corresponding cluster lengths. **C)** Proportion of detected m^{6}A sites assigned to clusters versus non-clustered sites. **D)** Kernel density plot comparing methylation level distributions of clustered and non-clustered sites. **E)** Violin plots showing methylation level distributions for clustered and non-clustered sites, with medians indicated. **F)** Meta gene analysis showing the transcriptomic distribution of clustered and non-clustered sites.

3.3.2 The m^{6}A landscape of the UCB T24 cell line

To further assess the robustness and reliability of GLORI, I sequenced T24 UCB cells treated with the METTL3 inhibitor STM2457 and a T24 UCB METTL3 KO clone. Previous LC-MS/MS analyses confirmed that STM2457 treatment and METTL3 KO led to a global reduction of m^{6}A levels by approximately 80% (Fig. 7B and Suppl. Fig. 4A), providing a suitable model to test whether GLORI can accurately detect loss of methylation. Again, sufficient mapping efficiencies and high conversion rates were obtained (Suppl. Tab. 1 and Suppl. Tab. 2). Notably, more than 85% of reads mapped to mRNAs in T24 cells treated with DMSO, whereas < 0.01% aligned to rRNA loci, confirming efficient mRNA enrichment during RNA preparation (Suppl. Tab. 3).

Sequence motif analysis for T24 cells treated with DMSO again showed that m^{6}A sites were predominantly located within the DRAC(H) consensus sequence motif (Fig. 17A). Among the 15 most frequent pentanucleotide motifs, canonical DRAC(H) variants were strongly overrepresented (Fig. 17B). Moreover, these motifs exhibited higher and more uniformly distributed methylation levels, whereas the non-canonical GGATT motif showed lower methylation levels (Fig. 17C). These results are in line with the observations in the HEK293T cell replicates (Fig. 15A-C). Further in-depth motif analysis showed that approximately 90% of all m^{6}A sites were detected in DRAC(H), while roughly 10% of the sites were found in sequence motifs with one mismatch compared to the DRAC(H) consensus (Suppl. Fig. 5A). m^{6}A sites in motifs with more than one mismatch compared to DRAC(H) were rarely detected (Suppl. Fig. 5A). Among the one-mismatch motifs, 36% were classified as DRACN motifs (retaining the DRAC(H) core in the first four bases), while 64% were non-DRACN motifs (mismatch occurring within the first four bases of the 5-mer, Suppl. Fig. 5B). The fifth position of DRACN motifs was consistently a guanine (Suppl. Fig. 5C). Furthermore, the analysis of methylation level distributions revealed that motifs unrelated to DRAC(H) showed lower methylation levels compared to canonical DRAC(H) (Suppl. Fig. 5D). Data analysis of T24 cells treated with STM2457 or with a METTL3 KO revealed that nearly all m^{6}A sites showed a reduction in methylation signal when comparing the mean methylation levels of methylated DRAC(H) sites across all replicates, both transcriptome-wide (Fig. 17D and Suppl. Fig. 6) and at the level of specific transcripts (Fig. 17E). Comparison of methylation level distributions across motif groups showed that DRAC(H), DRACN, and non-DRACN motifs were characterized by reduced methylation in STM2457-treated samples compared to the DMSO control, whereas methylation levels in motifs with more than one mismatch compared to DRAC(H) remained rather unchanged (Suppl. Fig. 5E). Based on these findings, I considered m^{6}A sites detected in DRAC(H) motifs as high-confidence m^{6}A sites, while the remaining sites were interpreted as variable low-confidence sites, which might be the result of deamination or sequencing artefacts. Therefore, these low-confidence sites were excluded from all downstream analyses. Also, these results validate the sensitivity of GLORI and confirm that the vast majority of detected sites are dependent on METTL3 catalytic activity.

In DMSO-treated T24 cells, the quantification of m^{6}A sites per transcript revealed a median of four sites per transcript, although some transcripts harbored a high number of m^{6}A marks, with up to 154 sites detected (Fig. 17F). DRAC(H) motif methylation levels displayed a bimodal distribution, with peaks around 20% and 95% methylation (Fig. 17G). Metagene analysis showed that m^{6}A sites were predominantly enriched in the CDS and 3′-UTR, with a characteristic accumulation near stop codons (Fig. 17H).

Taken together, the quantitative m^{6}A landscape in T24 cells appears to be similar to that of HEK293T cells, indicating that GLORI yields consistent and comparable methylation profiles when using different cell models. These findings also suggest that the key characteristics of m^{6}A, including its sequence motif preference and distribution, are conserved across different human cell lines.

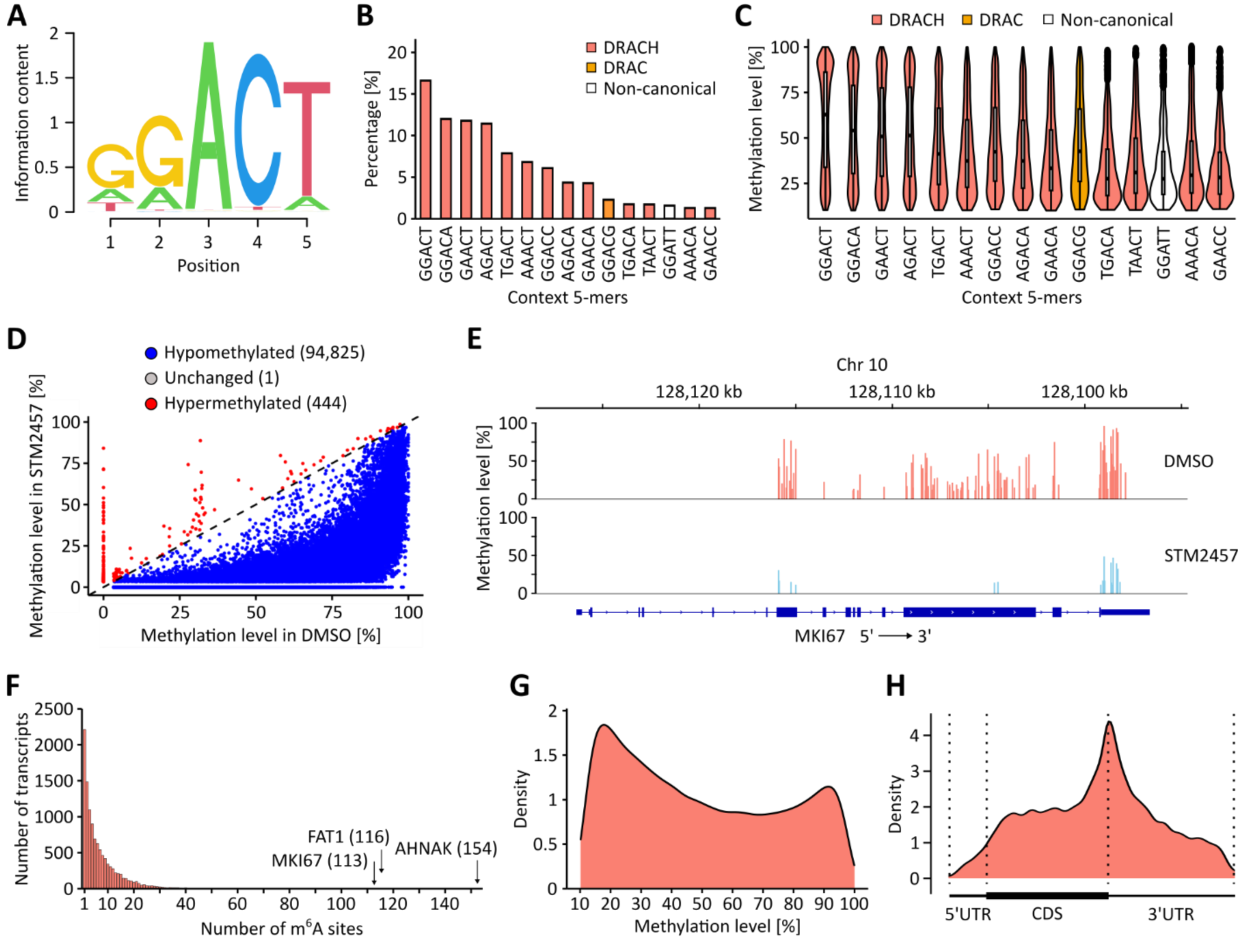

Fig. 17: Analysis of the m^{6}A landscape in T24 UCB cells. A) Sequence motif analysis of detected m^{6}A sites. **B)** Frequency of the 15 most observed sequence motifs among detected m^{6}A sites. **C)** Distributions of m^{6}A levels for the 15 most frequently detected motifs. **D)** Scatter plot comparing mean m^{6}A levels of methylated DRAC(H) sites shared between STM2457-treated and DMSO-treated T24 cells. **E)** IGV browser visualization of m^{6}A levels across the MKI67 transcript in DMSO-treated and STM2457-treated samples. **F)** Distribution of m^{6}A site counts per transcript. **G)** Kernel density plot showing the distribution of methylation levels for DRAC(H)-associated sites. **H)** Metagene plot illustrating the positional distribution of m^{6}A sites across transcript features.

3.4 Analysis of the UCB m^{6}A epitranscriptome

3.4.1 The m^{6}A epitranscriptomic landscape of UCB shows systematic differences

After implementing and validating GLORI, I performed comparative GLORI-seq of nine UCB samples and nine independent paratumoral control samples. The clinicopathological data from the GLORI patient cohort are listed in Tab. 4.

The GLORI-seq data sets generated from the patient samples exhibited high overall quality, comparable to the benchmark data sets previously obtained from the HEK293T and T24 cell lines (Suppl. Tab. 1 and Suppl. Tab. 2). To assess the sequence context of m^{6}A in UCB, a motif analysis was conducted. The majority of methylation events occurred within the canonical DRAC(H) consensus motif in both UCB and control samples (Fig. 18A). Further analysis of pentanucleotide motif frequencies and their associated methylation levels revealed no substantial differences between the two sample groups (Fig. 18B and C), indicating that m^{6}A motif specificity is conserved in UCB.

Tab. 4: Clinicopathological information from the GLORI cohort.

Clinical data	Attribute	Cohort (n=18)
Age	mean	76.9
	min-max	71-85
Tissue	n (uroepithelial)	9
	n (tumoral)	9
T-stage	Ta	6
	T1	0
	T2	3
	T3	0
	T4	0

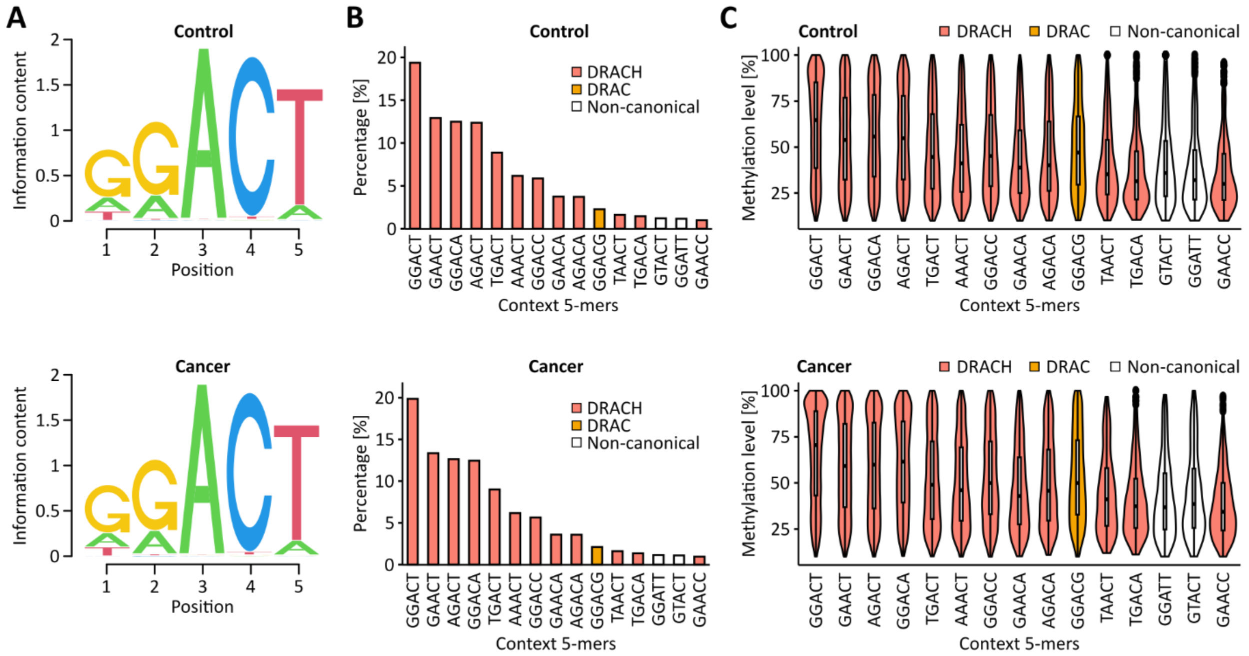

Fig. 18: The DRAC(H) motif is preserved in UCB. A) Sequence motif analysis of m^{6}A sites detected in UCB and control tissue samples. **B)** Bar graph showing the frequencies of the 15 most enriched motifs surrounding m^{6}A sites. **C)** Quantification of m^{6}A levels for the 15 most detected motifs.

Across the analyzed samples, approximately 42,000 m^{6}A sites were consistently detected in UCB tissues, while around 45,000 sites were shared among the control samples. To assess whether differences in m^{6}A site detection across samples could be explained by coverage or non-conversion, I compared coverage and methylation levels between shared and non-shared m^{6}A sites within UCB and control samples. Shared sites (detected in all 9 samples) showed higher median coverage (UCB: 129 vs. 37.7; Control: 87.3 vs. 31.3 reads, Suppl. Fig. 7A and C) and higher median methylation levels (UCB: 0.495 vs. 0.278; Control: 0.491 vs. 0.273, Suppl. Fig. 7B and D) compared to sites detected in fewer samples. These results suggest that robust signals, defined by both high sequencing coverage and high methylation levels, tend to be consistently detected across samples. These overlapping sets of high-confidence methylation sites served as the basis for downstream comparative analyses. Investigation of the quantification of m^{6}A sites per transcript (Fig. 19A), methylation level distributions (Fig. 19B and C), metagene analyses (Fig. 19D), as well as m^{6}A cluster analyses (Suppl. Fig. 8) revealed no major differences between UCB and control tissues. Despite the observed overall similarities, principal component analysis (PCA) demonstrated a separation between UCB and control samples (Fig. 19E). The separation was further supported by additional dimensionality reduction techniques, such as Uniform Manifold Approximation and Projection (UMAP) and t-distributed Stochastic Neighbor Embedding (t-SNE), which confirmed the robust segregation of cancer and control groups (Suppl. Fig. 9A). This finding indicates that, while the fundamental features of m^{6}A are preserved, cancer-specific alterations in methylation patterns exist and suggest the presence of distinct m^{6}A-based epitranscriptomic signatures associated with UCB.

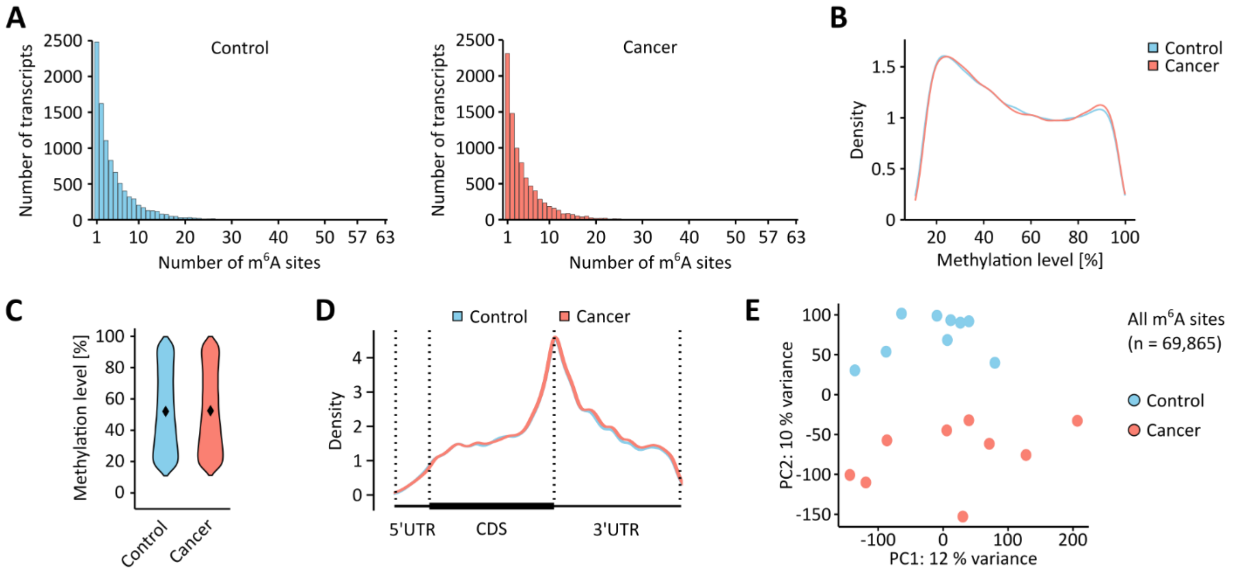

Fig. 19: The m^{6}A landscapes of UCB and control samples show systematic differences. A) Distribution of the number of m^{6}A sites per transcript in UCB and control samples. **B)** Kernel density plot showing the distribution of m^{6}A levels across individual sites in both tissue groups. **C)** Violin plots illustrating methylation level distributions and median values for m^{6}A sites in UCB and control samples. **D)** Metagene profiles depicting the positional distribution of m^{6}A sites across transcript features for both tissue types. **E)** PCA of m^{6}A methylation profiles in UCB and control samples. Notably, PCA was performed on the union of m^{6}A sites detected across all samples.

3.4.2 UCB-related hyper- and hypomethylation are enriched in oncogenic pathways

To further explore the m^{6}A-based epitranscriptomic signatures associated with UCB, I performed a differential methylation analysis to identify m^{6}A sites that were altered in UCB compared to control tissues. To determine a threshold for the absolute methylation difference of a differentially methylated site, a within-group variability analysis of detected DRAC(H) sites was performed. The methylation levels of a DRAC(H) site were found to fluctuate by an average of 1.2% within each sample group (Suppl. Tab. 4). Moreover, 90% of all sites showed a standard deviation (SD) below 6% across replicates (Suppl. Tab. 4). Thus, I decided to set a 10% cutoff for the absolute methylation difference since between-group differences of ≥ 10% exceed the observed within-group variability. Applying these stringent selection criteria (absolute difference in methylation level ≥ 10% and p-value < 0.05), a total of 3,159 differentially methylated sites were identified. Of these, 1,921 sites exhibited increased methylation levels in UCB tissues (hypermethylated), while 1,238 sites showed reduced methylation levels (hypomethylated, Fig. 20A). To assess the overall impact of these differentially methylated sites on sample identity, I performed another PCA and further dimensionality reduction analyses using the 3,159 sites. These analyses again demonstrated a clear separation between UCB and control samples (Fig. 20B and Suppl. Fig. 9B). Next, I mapped the differentially methylated sites to their respective transcripts to investigate transcript-level changes in methylation (Fig. 20C). This revealed 1,186 transcripts that were hypermethylated and 902 transcripts that were hypomethylated in UCB. Only a subset of transcripts showed both hyper- and hypomethylated sites, indicating that the majority of transcripts were consistently hyper- or hypomethylated (Fig. 20C). To gain initial insights into the potential consequences of these methylation alterations, I conducted pathway enrichment analyses based on the transcripts with differentially methylated sites. This analysis highlighted an enrichment in pathways previously implicated in UCB pathogenesis [153-155], including TNFα signaling, NOTCH signaling, the p53 and TGFβ signaling axes, as well as apoptotic pathways and epithelial-mesenchymal transition (Fig. 20D). These findings suggest that altered m^6A methylation may contribute to the dysregulation of critical oncogenic pathways in UCB. Among the differentially methylated transcripts, several notable cancer-associated genes were identified, including MYC, SMAD3, and BTG2, all of which have been previously linked to UCB [117,156-158] (Fig. 20E). These transcripts exhibited prominent hypermethylation within their CDS and 3′-UTRs. Collectively, the results highlight a cancer-specific m^6A methylation signature that distinguishes UCB from paratumoral tissue and is associated with cancer-associated pathways and transcripts.

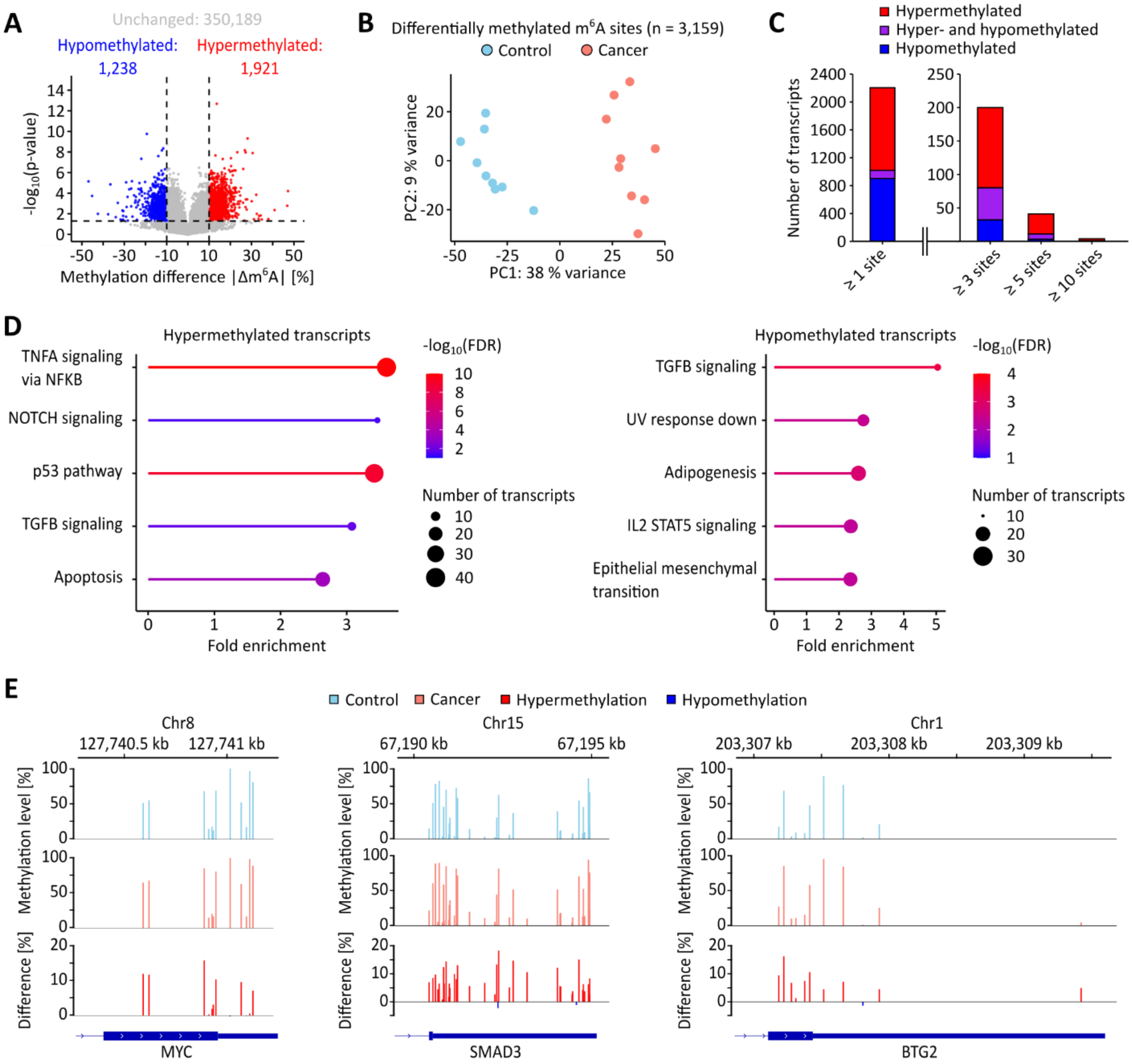

Fig. 20: Differential m^{6}A methylation analysis reveals hyper- and hypomethylation in UCB. A) Overview of differentially methylated m^{6}A sites in UCB samples compared to controls, based on |Δmethylation| ≥ 10% and $p < 0.05$ thresholds. Unmethylated DRAC(H) sites are included in this analysis. **B)** PCA of UCB and control samples using the differentially methylated m^{6}A sites. **C)** Distribution of differentially methylated transcripts in UCB, indicating the numbers of transcripts with hypermethylated sites, hypomethylated sites, or both. **D)** Top five enriched pathways identified from transcripts containing differentially methylated m^{6}A sites. **E)** Selected examples of transcripts showing hypermethylation in UCB.

3.4.3 Global UCB m^{6}A level becomes diluted due to changes in transcript abundance

I have previously used LC-MS/MS to show that UCB is characterized by a global reduction in m^{6}A methylation when compared to control samples (Fig. 10). However, the GLORI results suggested an overall trend toward gain of methylation in UCB (Fig. 20A and C). To resolve this apparent contradiction, I investigated the cancer-associated m^{6}A pattern changes further. When I analyzed the aggregate methylation levels of all m^{6}A sites, no difference between the cancer and the control group was detected (Fig. 21A). As such, the loss of methylation observed in the LC-MS/MS analyses could not be directly recapitulated by site-specific methylation mapping, potentially because the latter does not consider the abundance of transcripts.

To address transcript abundance in my analysis, I analyzed RNA-seq data sets from the same samples that were used for GLORI. PCA of the RNA-seq data revealed a clear separation between UCB and control tissue samples, indicating that the overall gene expression profiles differ substantially between the two groups (Suppl. Fig. 10A). To further explore these differences, a differential gene expression analysis was performed, which uncovered extensive transcriptomic alterations in UCB. In total, 6,091 genes were identified as differentially expressed between UCB and control tissues (Suppl. Fig. 10B). Subsequent cumulative analysis of normalized transcript levels showed that few transcripts made up a high proportion of the total transcriptome (Fig. 21B), with roughly 100 transcripts making up 50% of the transcriptome in both groups. This raised the possibility that methylation and/or expression changes in these highly abundant transcripts could strongly impact the global methylation level. Therefore, I determined the methylation level for each transcript by forming the sum of the methylation levels from individual m^{6}A sites, which was then multiplied by its normalized expression level. These weighted methylation levels were then summed up to obtain a global methylation level. When comparing the weighted global methylation levels of UCB and control tissues, a global hypomethylation of UCB tissue samples was observed (Fig. 21C), which confirmed the results observed in previous LC-MS/MS analyses (Fig. 10). Next, I wanted to identify the fraction of transcripts that underpinned this effect by performing a global expression analysis considering the methylation status of the transcripts. This revealed that unmethylated, highly abundant transcripts were upregulated, while highly methylated, highly abundant transcripts were downregulated in UCB (Fig. 21D), thereby indicating that the observed reduction of m^{6}A was primarily caused by the fraction of the most abundant transcripts. For instance, several transcripts with high cumulative m^{6}A methylation levels (aggregate methylation > 2), such as EGR1, JUN, JUNB, and FOS, were downregulated in UCB samples (Fig. 21E). In contrast, several transcripts from the S100 gene family, which were found to be unmethylated, were upregulated in UCB (Fig. 21F).

Together, these observations support the notion that the overall abundance of m^{6}A marks is not reduced in the cancer transcriptome but becomes diluted as a result of the upregulation of unmethylated transcripts and concurrent downregulation of highly methylated transcripts.

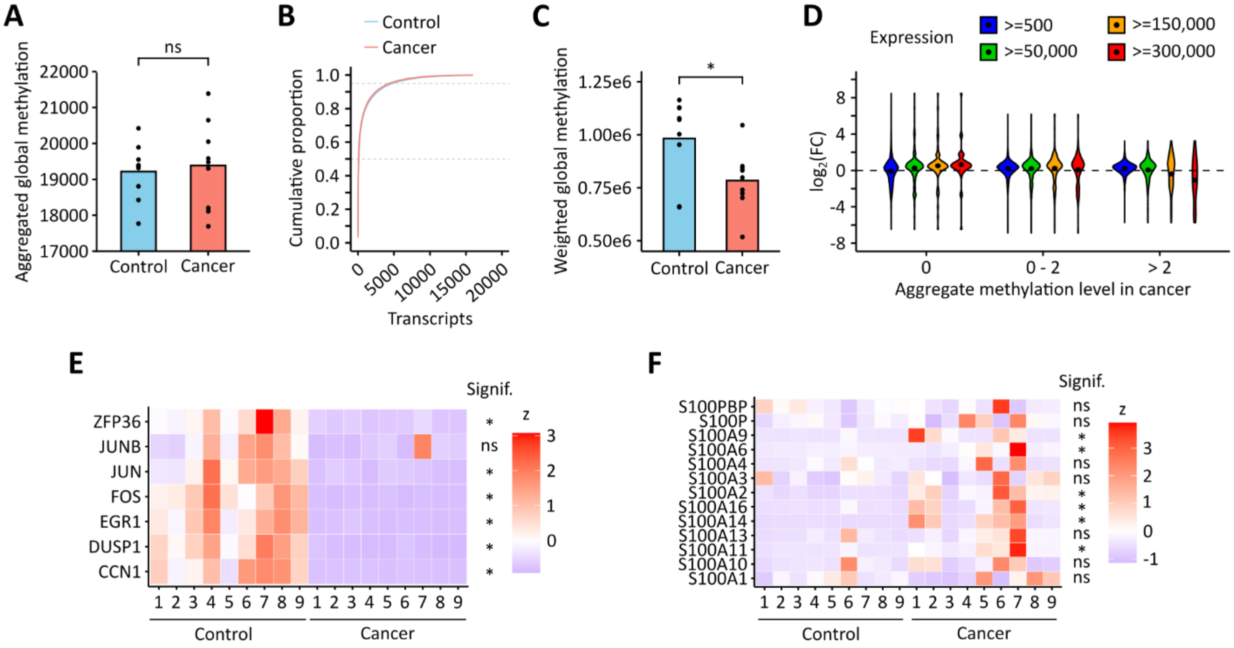

Fig. 21: Global m^{6}A hypomethylation in UCB is driven by changes in transcript abundance. **A)** Aggregated methylation levels of UCB and control tissues. ns = not significant, t-test. **B)** Cumulative proportion plot showing transcript abundance distributions in UCB and control samples. **C)** Weighted global m^{6}A levels in UCB and control tissues. *p < 0.05, t-test. **D)** Global expression analysis of transcripts grouped by their methylation status. Analyses are shown for all transcripts and for more abundant transcripts (normalized expression values are shown). **E)** Expression heatmap of selected transcripts that were highly methylated and abundant in both conditions. ns = not significant, *q < 0.05. **F)** Heatmap showing the expression of the unmethylated S100 family transcripts. ns = not significant, *q < 0.05.

3.4.4 Local stop codon m^6A hypermethylation is associated with VIRMA upregulation

To further investigate the impact of the differentially methylated m^6A sites on transcript regulation, I conducted a differential expression analysis. Integrated data analysis revealed that the majority of transcripts with hypermethylated m^6A sites was upregulated, while no clear tendency for transcripts with hypomethylated m^6A sites was identified (Suppl. Fig. 11A). A correlation analysis found no correlation between differential methylation and expression in UCB (Suppl. Fig. 11B). These results suggest that the impact of m^6A is transcript-specific and that the modification cannot be generalized as a stabilization or degradation mark in UCB.

To investigate whether specific sequence contexts were associated with differential m^6A methylation in cancer, sequence motif analyses were performed. These analyses revealed that hypermethylated m^6A sites were most frequently found within the GGACT motif, suggesting an enrichment of methylation in this sequence motif in the cancer samples (Fig. 22A). In contrast, hypomethylated sites were more commonly associated with TGACT and AAACT motifs (Fig. 22A). To complement these findings, I performed metagene analyses to examine the distribution of differentially methylated m^6A sites along transcript features. This analysis demonstrated that hypermethylated sites were predominantly enriched in the 3′-UTR, with an accumulation near the stop codon, while hypomethylated m^6A sites did not display any pronounced positional preference, suggesting that the observed methylation loss may occur without region-specific targeting (Fig. 22B).

A previous study has linked the enrichment of m^6A around stop codons to the regulatory activity of VIRMA, particularly in HeLa cells [20]. Based on these observations, I hypothesized that a similar mechanism may contribute to the cancer-associated hypermethylation patterns observed in my data set. Therefore, I first quantified VIRMA mRNA expression levels across the sample set. The analysis revealed a statistically significant upregulation of VIRMA in UCB samples compared to control tissue (Fig. 22C). To validate this finding in a larger cohort, the expression analysis was extended to a combined data set from The Cancer Genome Atlas (TCGA) and Genotype-Tissue Expression (GTEx), which includes transcriptomic profiles of both tumor and healthy bladder tissues. This cohort confirmed the initial observation, showing that VIRMA is significantly overexpressed in UCB relative to paratumoral tissue (Fig. 22D). These consistent findings suggest that VIRMA expression is increased in UCB. Next, I sought to understand the potential mechanisms driving VIRMA overexpression in UCB. By examining genomic data from UCB patients to assess the frequency of genetic alterations affecting the VIRMA locus, I found that VIRMA gene amplification occurs in approximately 6% of UCB tumors (Suppl. Fig. 12). This frequency is comparable to that of other oncogenes implicated in UCB, such as MYC (amplified in 2.9% - 3.3% of tumors [159,160]), FGFR1 (3.7% - 7% [161,162]), and HER2 (8% - 8.7% [161,163]), suggesting that VIRMA amplification may be biologically relevant. To determine whether this genomic amplification translates into elevated expression, a correlation analysis between VIRMA copy number variation and its mRNA expression levels across tumor samples was performed. This analysis revealed a highly significant positive correlation, supporting the notion that copy number gains contribute to VIRMA overexpression in UCB (Fig. 22E).

To further dissect the functional relevance of VIRMA in shaping the m^6A landscape in UCB, I generated UM-UC-3 and RT4 VIRMA KD cell lines using shRNA-mediated silencing (Fig. 22F and Suppl. Fig. 13A). Consistent with the role of VIRMA as a key component of the m^6A writer complex, depletion of VIRMA led to a marked global reduction in m^6A levels when comparing the mean methylation levels of methylated DRAC(H) sites across all replicates (Fig. 22G and Suppl. Fig. 13B). Differential methylation analysis revealed VIRMA-dependent m^6A sites and widespread hypomethylation upon VIRMA KD (Fig. 22H and Suppl. Fig. 13C). Notably, when examining the positional distribution of these hypomethylation events, I observed that the strongest and densest methylation level reductions localized to regions surrounding the stop codon (Fig. 22I and Suppl. Fig. 13D). This corresponds to the inverse signature detected in patient tumor samples, where hypermethylation near stop codons was associated with VIRMA upregulation, and reinforces the notion that VIRMA is a regulator of 3'-UTR-proximal m^6A methylation in UCB.

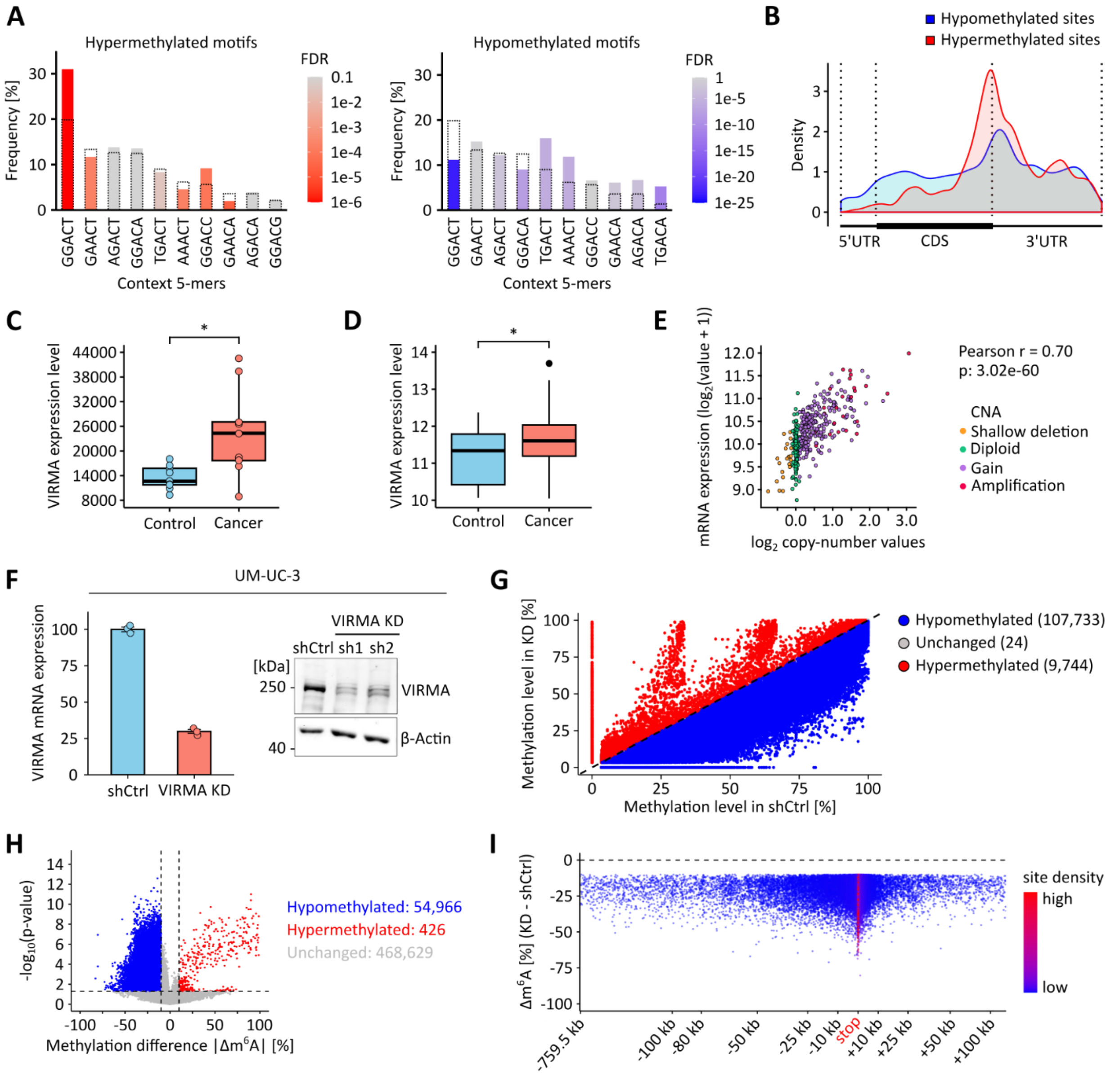

Fig. 22: VIRMA upregulation in UCB is linked to stop codon m^{6}A hypermethylation. A) Motif enrichment analysis of hyper- and hypomethylated m^{6}A sites. Dashed bars indicate overall motif frequency in cancer samples. Colored bars show frequencies among differentially methylated sites. **B)** Metagene plot showing the positional distribution of hyper- and hypomethylated m^{6}A sites. **C)** VIRMA expression levels in UCB and control tissues based on RNA-seq data. *$p < 0.05$, Mann-Whitney-U test. **D)** VIRMA expression in combined TCGA and GTEx data sets compared to control tissues (UCB, n = 407; control, n = 28). *$p < 0.05$, Mann-Whitney-U test. **E)** Correlation between VIRMA copy number and mRNA expression. $p = 3.02 \times 10^{-60}$, Pearson correlation. CNA = copy number alteration. **F)** RNA-seq and Western blot analyses of VIRMA expression levels in UM-UC-3 VIRMA KD and shCtrl cells. **G)** Scatter plot comparing mean m^{6}A levels of methylated DRAC(H) sites shared between UM-UC-3 VIRMA KD and shCtrl cell lines. **H)** Overview of differentially methylated m^{6}A sites in VIRMA-depleted UM-UC-3 cells, based on |Δmethylation| ≥ 10% and $p < 0.05$ thresholds. Unmethylated DRAC(H) sites are included in this analysis. **I)** Δm^{6}A levels (UM-UC-3 VIRMA KD - shCtrl) for differentially hypomethylated m^{6}A sites were plotted across transcript regions surrounding the stop codon.

Additionally, the clinical relevance of VIRMA in UCB was investigated by conducting a Kaplan-Meier survival analysis. The results demonstrated that patients with high VIRMA expression exhibited significantly poorer overall survival compared to those with lower expression levels (Fig. 23A). This analysis was performed in collaboration with Dr. Jinyun Xu (Division of Epigenetics, German Cancer Research Center, Heidelberg). In functional assays, VIRMA-depleted UCB cells were characterized by reduced cell proliferation and colony formation as well as increased Caspase 3/7 activity (Fig. 23B-D). These findings align with the pro-oncogenic expression pattern of VIRMA observed in UCB patient cohorts, where elevated VIRMA levels correlate with poor prognosis, and support a functional role for VIRMA in promoting tumor cell growth and survival.

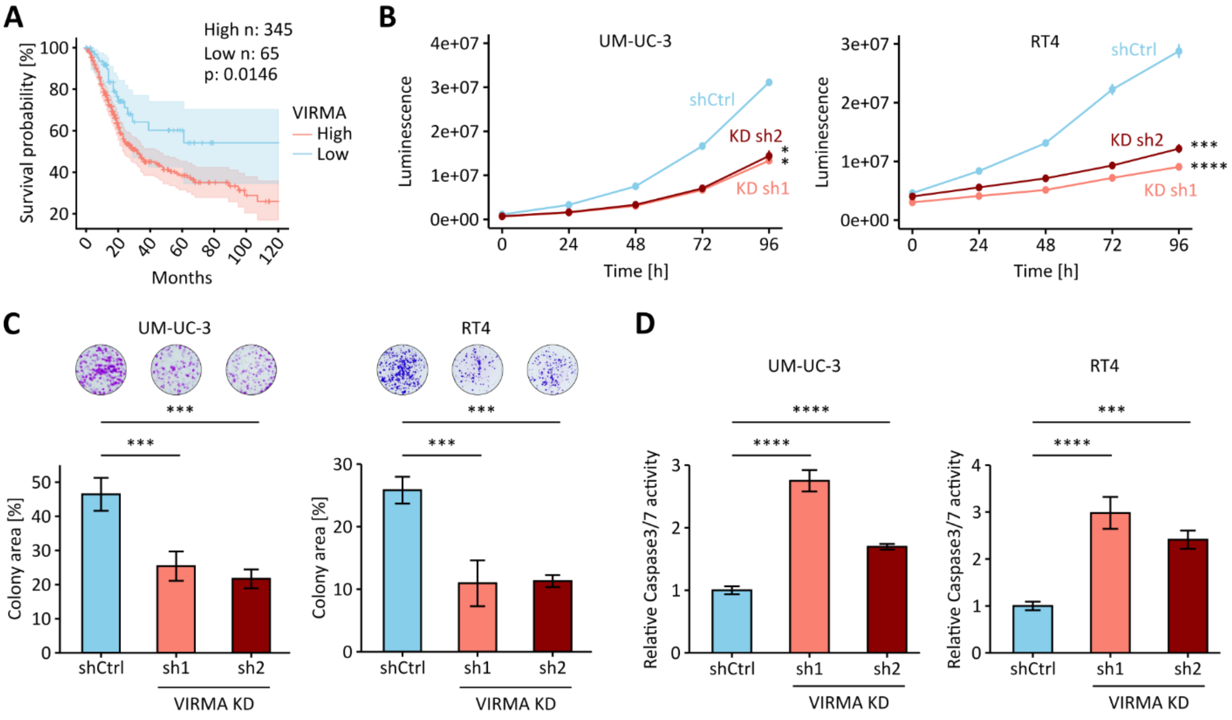

Fig. 23: Knockdown of VIRMA reduces the oncogenic phenotype of UCB cells. A) Kaplan-Meier survival analysis comparing VIRMA-high and VIRMA-low patient samples. p = 0.0146, log-rank test. **B)** Cell proliferation of VIRMA KD and control cells. *p < 0.05, ***p < 0.001, ****p < 0.0001, two-way analysis of variance. **C)** Colony formation results of VIRMA KD and control cells. ***p < 0.001, one-way analysis of variance. **D)** Caspase 3/7 activity measurements in VIRMA KD and control cells. ***p < 0.001, ****p < 0.0001, one-way analysis of variance.

Since m^6A and VIRMA have also been implicated in the regulation of mRNA polyadenylation [20], I finally sought to explore whether the UCB-associated changes in m^6A and VIRMA expression patterns might be linked to alterations in APA. Thus, I analyzed the RNA-seq patient data sets for changes in the usage of proximal and/or distal polyadenylation sites by calculating the difference in Percentage of Distal polyA site Usage Index (ΔPDUI) using the Dapars algorithm [164]. This analysis revealed that the majority of transcripts exhibited negative ΔPDUI values, indicating a preferential usage of proximal polyadenylation sites and thus a general trend toward 3'-UTR shortening in UCB (Fig. 24A). The comparison of the proportion of m^6A-methylated transcripts that are 3'-UTR lengthened or shortened showed that shortened transcripts are more likely to be m^6A-methylated (Fig. 24B). To investigate if m^6A or VIRMA could influence APA, I similarly performed further global alternative polyadenylation profiling analyses in the VIRMA- and METTL3 depletion cell models. The analysis of VIRMA KD cell models showed a tendency toward transcript 3'-UTR lengthening, indicative of positive ΔPDUIs. This effect was robust in UM-UC-3 VIRMA KD cells (Fig. 24C) and detectable, although less pronounced, in the RT4 VIRMA KD cell line (Suppl. Fig. 14A), eventually reflecting variable KD efficiency. Regarding the METTL3 depletion models, I analyzed UCB cell clones with a KO of METTL3 (T24 clone O with a global relative reduction of m^6A by 75% (Fig. 7B); UM-UC-3 clone N with a global relative reduction of m^6A by 45% (Suppl. Fig. 2B)), and UCB cell lines treated with the METTL3 inhibitor STM2457 (global relative reduction of m^6A by 75%, Suppl. Fig. 4A). In these models, RNA-seq data again showed a predominant shift toward longer 3'-UTRs, as reflected by positive ΔPDUI values across most transcripts (Fig. 24D and Suppl. Fig. 14B). Together, these results strengthen the link between m^6A and polyadenylation site selection, suggesting that m^6A methylation or the m^6A writer complex promote proximal polyadenylation site usage under standard conditions and thereby contribute to the shaping of the UCB transcriptome.

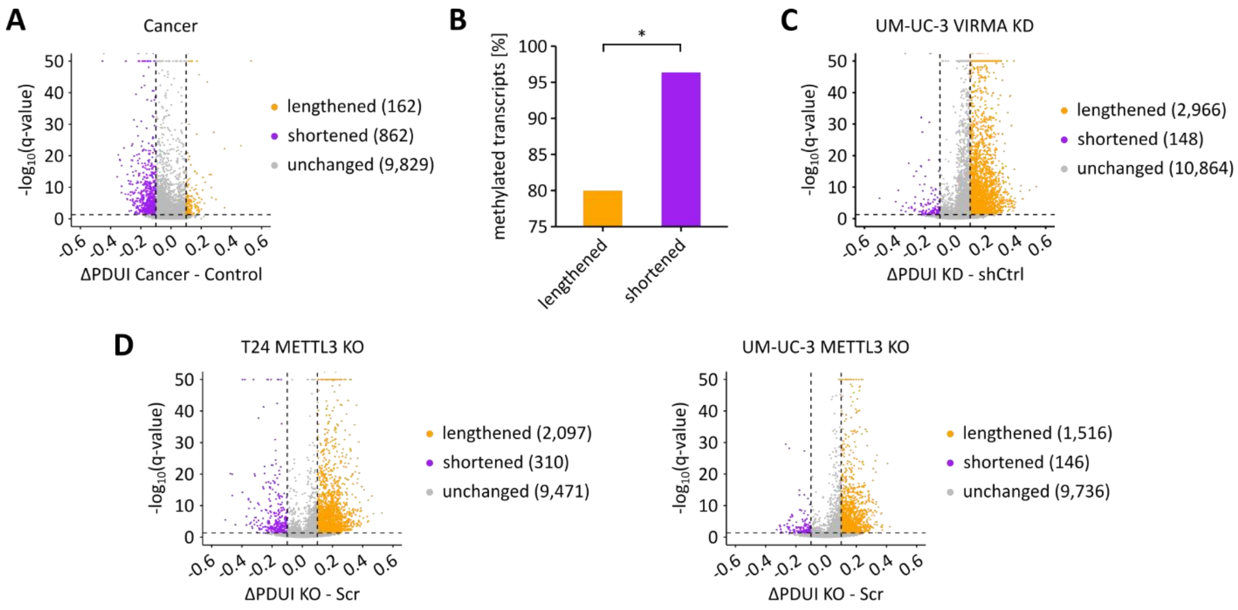

Fig. 24: m^{6}A promotes the selection of proximal polyadenylation sites. A) DaPars-based analysis of APA showing ΔPDUI for the UCB patient samples compared to the paratumoral control patient samples. **B)** Comparison of the proportion of m^{6}A methylation in 3'-UTR lengthened or shortened transcripts. *p = 6.301e-10, Fisher's exact test. **C)** DaPars-based analysis of APA showing ΔPDUI for UM-UC-3 VIRMA-depleted cells compared to shCtrl cells. **D)** DaPars-based analysis of APA showing ΔPDUI for T24 and UM-UC-3 METTL3 KO cells compared to Scr cells.

4 Discussion

m^6A represents the most prevalent internal modification found within eukaryotic mRNAs, playing a central role in post-transcriptional gene regulation. This RNA modification influences all stages of the mRNA life cycle, including splicing, APA, nuclear export, translation, and decay, thereby regulating the stability, localization, and translational efficiency of target transcripts [165]. In recent years, several studies highlighted the significance of m^6A and its associated machinery in a broad range of physiological and pathological contexts [166,167]. Notably, growing evidence suggests that cancer development is accompanied by alterations in the m^6A epitranscriptome. These include dysregulated expression of m^6A writer, eraser, and reader proteins, as well as aberrant methylation of individual transcripts implicated in tumor progression [104], including in the context of UCB [168].

Given the oncogenic functions attributed to METTL3, the catalytic core component of the m^6A writer complex, in a variety of cancer types, the enzyme has emerged as a candidate for targeted therapeutic intervention [56]. Preclinical studies showed that treatment with a selective small-molecule METTL3 inhibitor led to a significant reduction in m^6A methylation on key leukemogenic transcripts [127]. This impaired their translation, resulting in reduced leukemic cell proliferation and engraftment. In a leukemia mouse model, METTL3 inhibition not only delayed disease progression but also significantly prolonged overall survival without inducing major toxicities or adverse effects, thereby underscoring the potential of METTL3-targeted therapies in oncology [127]. In UCB, however, METTL3 has been described as both an oncogene and a tumor suppressor by independent studies [117,118]. These contradictory findings point to an unresolved controversy regarding the precise role of METTL3 in UCB pathogenesis.

Moreover, most prior efforts to map m^6A modifications in the transcriptome have relied on antibody-based enrichment methods, which are limited in resolution, prone to cross-reactivity, and do not provide quantitative information on methylation stoichiometry [76,79]. Thus, the precise, cancer-associated changes in m^6A deposition and the regulatory mechanisms driving alterations in the cancer m^6A epitranscriptome have remained largely undefined. Additionally, much of the evidence is derived from *in vitro* or *in vivo* model systems, which cannot completely capture the molecular complexity of human cancer.

In this study, the role of METTL3 in UCB was revisited, with a particular emphasis on its relevance for cell viability and its potential as a clinical target in UCB patients. Interestingly, despite the observed increased METTL3 expression in UCB [117,138], global m^6A levels were found to be reduced, revealing an apparent contradiction that prompted a more detailed investigation of the cancer-associated m^6A landscape. To explore these alterations, GLORI-seq, a technique that enables site-specific, absolute quantification of m^6A modifications using an antibody-independent chemical deamination approach, was applied to a set of patient samples. This finally enabled the description of the first quantitative, transcriptome-wide, single-nucleotide resolution atlas of m^6A in UCB, as well as the characterization of cancer-associated m^6A signatures.

4.1.1 The role of METTL3 in UCB and its potential as a therapeutic target

METTL3 is the catalytic core of the m^6A writer complex and, therefore, important for maintaining RNA metabolism in eukaryotic cells. Given this fundamental role, the dysregulation of METTL3 has been implicated in the pathogenesis of various cancers. However, its function appears to be highly context-dependent, with studies reporting both oncogenic and tumor-suppressive roles depending on the tumor entity [56]. In some malignancies, such as endometrial and thyroid cancer, METTL3 has been described as a tumor suppressor, where its loss promotes tumor progression through altered gene expression programs [124,125]. Conversely, METTL3 was shown to function as an oncogene in other cancer types, such as colorectal and lung cancer, promoting tumor growth and survival by m^6A-dependent stabilization and translation of oncogenic transcripts [74,169].

The situation in UCB is particularly complex, as the role of METTL3 has been interpreted in contradictory ways. While several independent studies have classified METTL3 as an oncogene in UCB through the m^6A-dependent upregulation of oncogenic transcripts (e.g., MYC, ITGA6) or the downregulation of tumor-suppressive transcripts (e.g., SETD7, KLF4) [117,138,140-142,144], another report pointed toward a tumor-suppressive function [118]. Notably, the choice of cell line does not appear to explain the contradictory findings. For instance, the study that described METTL3 as a tumor suppressor used 5637 and T24 cells [118], yet these same cell lines were also used in studies that demonstrated oncogenic functions of METTL3 [140,141]. In this study, this controversy was investigated by generating T24 and UM-UC-3 METTL3 KO cell lines and by characterizing their phenotypic changes compared to control cells. Upon METTL3 KO, the cell lines showed a substantial reduction in cell proliferation, impaired clonogenicity, and increased apoptosis signaling when compared to control cells. These observations are consistent with the majority of published studies and support the notion that METTL3 is more likely to act as an oncogene in UCB.

While these initial functional assays clearly suggested an oncogenic role of METTL3 in UCB, first insights from LC-MS/MS experiments raised the question of whether METTL3 is an essential gene required for the viability of UCB cells. Since METTL3 is considered to be responsible for > 95% of m^6A methylation in mRNA [170], the remaining m^6A methylation levels in METTL3 KO cell pools pointed toward selection processes for cells expressing catalytically active METTL3. To investigate these presumable selection processes, individual METTL3 KO clones from both cell lines were screened via Western blots. The results showed that surviving clones expressed either WT METTL3 or shortened METTL3 variants. No clones with a complete loss of WT METTL3 protein were isolated. These findings are consistent with a previous study reporting the emergence of alternatively spliced METTL3 isoforms in KO cells that bypass CRISPR/Cas9-induced mutations [149]. Further LC-MS/MS analyses revealed that even clones with the strongest depletion of WT METTL3, as well as those clones expressing aberrant METTL3 variants, retained residual m^6A methylation levels. These findings suggest that the shorter METTL3 variants still exert methyltransferase activity and that a minimum level of METTL3 activity is required for viability. This is further supported by a previous study showing that a homozygous METTL3 KO in mice leads to early embryonic lethality, thereby highlighting the essential role of METTL3 [148]. The dependency of the UCB cells on METTL3's catalytic activity was also strengthened by pharmacological inhibition experiments using the small-molecule METTL3 inhibitor STM2457, which showed a dose-dependent reduction of the oncogenic phenotype of UCB cells. Further *in silico* analyses using the DepMap databank supported the findings from *in vitro* studies using T24 and UM-UC-3 cells and extended them to other UCB cell models and to other cancer entities, thereby reinforcing the notion that cancer cells depend on METTL3 for cell viability and proposing METTL3 to be an essential gene in cancer [149].

As METTL3 was identified to be essential for the viability of UCB cells, the question arose whether METTL3 is likewise essential for uroepithelial cells. This consideration is critical when evaluating the therapeutic potential of METTL3, as any candidate drug target must ideally show a degree of cancer-specific dependency to avoid toxicity in healthy tissues. To address this question, the small-molecule METTL3 inhibitor STM2457 was applied across a panel of UCB cell lines as well as the uroepithelial UROtsa cell line. Drug-response curves revealed that UROtsa cells showed the highest IC50 value (75 µM), indicating lower sensitivity to METTL3 inhibition compared to the panel of UCB cell lines. However, the difference in sensitivity between UROtsa cells and at least one of the UCB cell lines (T24, 67 µM) was only moderate. Also, the UROtsa cells showed reduced viability at higher STM2457 concentrations, suggesting that uroepithelial cells depend on METTL3 activity as well. These findings imply that the therapeutic window for METTL3 inhibition in UCB may be narrow, with only limited selectivity toward malignant cells due to the pan-essential character of METTL3. Pan-essential genes have been frequently misclassified as tumor-selective in preclinical studies, particularly when the model systems cannot sufficiently represent the complexity of normal tissues. Consequently, drugs targeting pan-essential genes often exhibit a low therapeutic index [171,172].

In my LC-MS/MS analyses, a pronounced global reduction in m^6A methylation levels in UCB tissues compared to matched paratumoral tissues was revealed. These findings substantially expand upon previously published LC-MS/MS results, which had reported a 2-3-fold increase in m^6A levels in UCB [117]. However, this study relied on data from only two tumor samples and did not include appropriate controls to assess potential rRNA contamination, which may have affected the results. Thus, despite its upregulation in UCB [117,138], METTL3 does not appear to drive an increase in global m^6A mRNA methylation levels. These contradictory findings likely reflect the complex role of METTL3 in UCB, which underscores the need for more models to fully elucidate METTL3's functional relevance in UCB. Furthermore, to address this inconsistency and reveal cancer-associated alterations in the m^6A landscape of UCB, the implementation of a robust m^6A detection technique was essential for generating high-resolution m^6A maps.

4.1.2 Implementation of GLORI-seq for quantitative, base-resolution m^6A mapping

A major challenge in studying m^6A is the specific and robust detection of modification sites across the transcriptome. Although widely used, the antibody-dependent m^6A detection techniques have been repeatedly criticized for several limitations, including the requirement for large amounts of input RNA, low resolution, and the detection of false positives due to unspecific antibodies. Moreover, these methods do not allow for the absolute quantification of methylation levels, limiting their usability for studying m^6A alterations [76,79]. Additionally, enzyme-assisted m^6A detection methods depend on enzymatic efficiency and have limited applicability to clinical samples [82,84,85]. Therefore, a main goal of this study was the implementation, evaluation, and application of an antibody- and enzyme-independent technique for m^6A detection.

GLORI-seq was implemented, offering transcriptome-wide, base-resolution, and quantitative detection of m^6A modifications through selective deamination of unmodified adenosines. To test if the underlying chemical reaction was functional, an initial validation was performed by deaminating a synthetic RNA oligonucleotide, which was used as a Spike-In control in all subsequent sequencing experiments. This experiment confirmed that the deamination chemistry worked as expected, thereby establishing a basis for further method development. Subsequently, the preparation of GLORI-seq libraries should be tested. One of the critical challenges involved reducing the formation of sequencing adaptor dimers, which can compromise library complexity and reduce sequencing efficiency. This issue was addressed by optimizing the end-repair steps of the input RNA and by implementing a precise fragment size selection strategy via TBE-PAGE purification. Additional optimization steps were undertaken to maximize the deamination efficiency. Conditions were established under which > 99% of unmodified adenosines were reliably converted to guanosines, which is comparable to the published conversion rates and enables accurate discrimination between m^{6}A-modified and unmodified sites [27]. To assess the performance of the implemented GLORI-seq protocol, MiSeq experiments were conducted using HEK293T cells. In these trials, published m^{6}A sites could be detected. Also, methylation levels were found to be reduced in STM2457-treated cells, thereby confirming the method's sensitivity to detect changes in methylation.

Following the initial validation of GLORI-MiSeq in HEK293T cells, the method was further evaluated using three biological replicates, which were deep-sequenced on the NovaSeq 6000 platform. The objective of this experiment was to assess the reproducibility and accuracy of GLORI-seq by comparing the results with the originally published m^{6}A map derived from the same cell line [27]. To provide an orthogonal validation and to assess cross-platform consistency, the RNA from the three biological replicates was pooled and subjected to direct RNA-seq. The results demonstrated that GLORI detected the majority (86.8%) of previously reported m^{6}A sites in HEK293T cells [27]. A substantial overlap (71.5%) was also observed when using the direct RNA-seq data. Moreover, the quantification of methylation levels was found to be highly reproducible across the three GLORI-seq biological replicates, as well as with the direct RNA-seq data, indicating that GLORI-seq reliably quantifies m^{6}A methylation levels. To further validate the implementation of GLORI, the data were subjected to a series of analyses matching those in the original study, including a sequence motif analysis, metagene profiling, global quantification of methylation distribution, and a m^{6}A cluster analysis. Each of these analyses revealed strong concordance with the published results [27], thereby confirming the reproducibility of GLORI-seq and its suitability for transcriptome-wide m^{6}A mapping at high resolution and quantitative accuracy.

After validating GLORI-seq using HEK293T cells, the method was next applied to the T24 UCB cell line. T24 cells were treated with either DMSO or with STM2457. Upon STM2457 treatment, almost all m^{6}A sites detected under control conditions showed either complete loss or a reduction in methylation, thereby confirming the sensitivity of GLORI-seq and supporting the notion that METTL3 is the primary m^{6}A mRNA methyltransferase. Further investigation of the

m^6A sites revealed an enrichment within the DRAC(H) motif, consistent with the known sequence specificity of the m^6A writer complex. To increase confidence in downstream analyses, only sites located within canonical DRAC(H) motifs were retained, while those found in non-canonical motifs were excluded to reduce the likelihood of including deamination or sequencing artifacts. Metagene analyses further revealed that m^6A sites in T24 cells are predominantly localized within the CDS and 3'-UTR of transcripts. The methylation level landscape showed a bimodal distribution, as previously described in the HEK293T cell data set of this study and the original data set [27]. Collectively, these results demonstrate that the core characteristics of m^6A, including its sequence motif preference and regional enrichment, are largely conserved between T24 and HEK293T cell lines. These results suggest that core properties of m^6A methylation are likely preserved across diverse cellular contexts [17,173].

4.1.3 Two epitranscriptomic signatures define the UCB m^6A landscape

m^6A plays an important role in the post-transcriptional regulation of gene expression by influencing the fate of its target mRNAs. The dysregulation of m^6A and its key regulatory proteins has been implicated in a range of oncogenic processes. Numerous studies across various cancer types have reported aberrant m^6A signatures and altered expression patterns of m^6A regulators, suggesting that m^6A epitranscriptomic remodeling contributes to tumorigenesis [56,174]. However, the vast majority of these studies relied on error-prone antibody-dependent m^6A mapping techniques. Further efforts included the use of direct RNA-seq to infer m^6A sites and their stoichiometry in cancers, such as clear cell renal cell carcinoma [175] and MIBC [150]. While these studies represent a conceptual advance toward antibody-free m^6A detection, the conclusions drawn from them remain preliminary since these approaches relied on supervised machine learning algorithms trained on plant data sets [176] and applied low-stringency cutoffs for calling differential methylation ($p < 0.1$), often in the context of very low read coverage at potential m^6A sites (> 2 reads). As a result, the understanding of the precise cancer-associated m^6A signatures and functional consequences remained incomplete.

To date, no study has provided a base-resolution, transcriptome-wide, and quantitative map of m^6A in cancer. The present study fills this gap by providing the first comprehensive m^6A map in UCB using GLORI-seq. GLORI-seq was applied to compare nine UCB tumor samples against nine independent paratumoral samples. Sequence motif analyses revealed that the majority of m^6A sites were detected within DRAC(H) consensus motifs. These findings are consistent with the established substrate specificity of the m^6A writer complex [25,26,34], and indicate that m^6A deposition specificity is preserved in UCB. Also, the results support the notion that m^6A profiles are robust in different tissue types [17,173] and extend them to cancer. Notably, a recent report showed that cancer-associated mutations in METTL14 cause m^6A deposition in non-canonical motifs [35]. Although the mutational status of the writer complex components was not investigated in the UCB cohort, this represents an important question for future research. GLORI-seq could serve as a powerful tool to directly assess whether such genetic alterations lead to changes in sequence specificity or redistribution of m^6A across the transcriptome.

Yet, systematic differences in the m^6A landscapes between UCB and paratumoral tissue were identified, which allowed for their separation in dimensionality reduction analyses. Differential methylation analyses found that the oncogenic MYC transcript, which is a known m^6A-regulated transcript in UCB [117], was hypermethylated in its CDS and 3'-UTR. Also, hypermethylation in other cancer-relevant transcripts, including SMAD3 and BTG2, was identified [156-158]. Furthermore, gene ontology analyses found both hypermethylation and hypomethylation of transcripts associated with oncogenic pathways, including TNFα, NOTCH, p53, and TGFβ signaling pathways, as well as pathways related to apoptosis and epithelial-mesenchymal transition [153-155]. These findings point toward the biological relevance of altered m^6A methylation in oncogenic pathways and raise the possibility that transcript-specific m^6A signatures could serve as novel biomarkers for UCB diagnosis or stratification. Given the current lack of robust molecular biomarkers for UCB, m^6A profiling may offer a promising alternative to address this unmet clinical need [6].

To enable a more accurate and biologically meaningful comparison of global m^6A methylation levels between UCB and paratumoral tissues, a novel computational approach was developed that integrates mRNA abundance data from RNA-seq into the GLORI analyses. Transcript methylation levels were weighted by the abundance of the same transcript, thereby accounting for the influence of highly expressed or lowly expressed transcripts, which would otherwise introduce bias into global methylation estimates. A comparison between the weighted global methylation levels revealed a global reduction in m^6A methylation levels in UCB, consistent with the findings from LC-MS/MS-based quantifications. Further analyses of the underlying transcriptomic changes indicated that this reduction was not caused by decreased methylation levels but rather resulted from alterations in the transcriptome composition. Specifically, the upregulation of abundant, unmethylated transcripts was found to dilute the global methylation level, while the downregulation of abundant, methylated transcripts reduced the overall contribution of methylated mRNAs to the global methylation level. These results support the hypothesis that apparent changes in global m^6A methylation levels across tissues, conditions, or treatments may often arise from altered mRNA metabolism rather than the regulation of the m^6A machinery itself [41]. Importantly, this analysis also highlights a key limitation of standard m^6A quantification approaches that do not adjust for transcript abundance, which may lead to misleading interpretations of global methylation levels.

In parallel, the data revealed a high density of hypermethylated sites near stop codons in UCB samples, a pattern that has previously been linked to the m^6A writer complex component VIRMA and the regulation of APA [20]. To investigate whether VIRMA contributes to this methylation pattern in UCB, two independent VIRMA KD cell lines were generated and profiled by GLORI-seq. Both KD models showed a pronounced global reduction in m^6A methylation levels, consistent with LC-MS/MS results from VIRMA-depleted breast cancer cells [177]. Notably, the decrease in methylation was most pronounced at sites near transcript stop codons, supporting a model in which VIRMA is the regulator of 3’-UTR m^6A deposition [20]. APA is a post-transcriptional mechanism by which multiple mRNA isoforms are generated from the same gene through the selective usage of proximal or distal polyadenylation sites. This process results in transcripts with alternative 3’-UTRs, which can differ substantially in terms of stability, subcellular localization, and translational efficiency [178]. APA has been increasingly recognized as a key mechanism in cancer biology, contributing to tumorigenesis and tumor progression [179]. In the patient cohort, analysis of APA patterns revealed pronounced 3’-UTR shortening in UCB transcripts, in line with previous findings from UCB and other cancers [164]. In contrast, VIRMA depletion as well as pharmacological or genetic depletion of METTL3 promoted lengthening of 3’-UTRs, indicating a shift toward distal polyadenylation site usage. These findings are consistent with earlier reports suggesting that m^{6}A-modified transcripts preferentially utilize proximal polyadenylation sites [20,80]. Furthermore, VIRMA has been shown to interact with the polyadenylation factors CPSF5 and CPSF6 in an RNA-dependent manner [20]. Since mRNA 3’-UTR shortening is a common feature of cancer transcriptomes, often allowing transcripts to escape from post-transcriptional repression [164], the common upregulation of VIRMA [180] and METTL3 [56] in cancers may contribute to 3’-UTR remodeling in the malignant context.

Supportive of this model, VIRMA depletion decreased cell proliferation as well as colony formation, and increased apoptosis signaling in two UCB cell lines, suggesting that VIRMA promotes an oncogenic cellular phenotype. Similar findings were reported in other cancer entities, including breast cancer [177,181], head and neck squamous cell carcinoma [182], nasopharyngeal carcinoma [183], and pancreatic cancer [184]. Additionally, VIRMA has been reported to be genomically amplified and frequently upregulated across a variety of cancer types, with elevated expression correlating with poor patient prognosis [180,185]. VIRMA expression and survival analyses presented in this study are consistent with these findings and support a functional role for VIRMA in shaping the UCB-specific m^{6}A landscape, particularly in mediating hypermethylation near stop codons, and in promoting the oncogenic phenotype of UCB cells.

Taken together, this GLORI-based analysis identified two distinct signatures remodeling the m^{6}A landscape in UCB (Fig. 25). First, a global dilution of methylation levels caused by mRNA abundance changes. Second, local VIRMA-associated hypermethylation near stop codons potentially influencing alternative 3’-UTR usage and transcript isoform diversity.

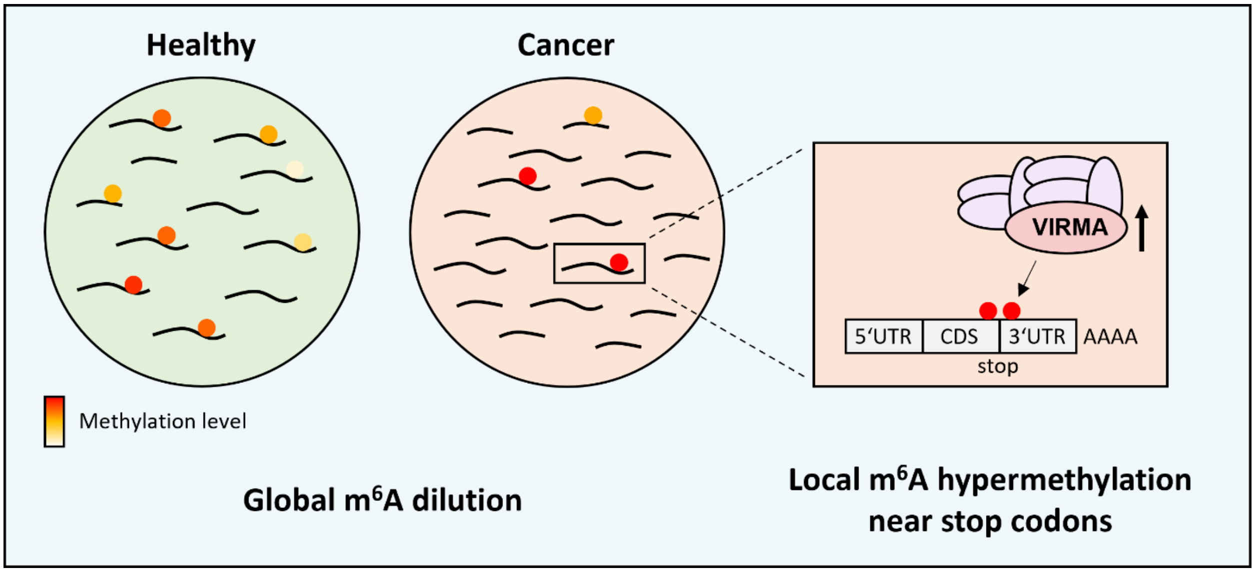

Fig. 25: The UCB m^{6}A epitranscriptome is characterized by two signatures. Global methylation dilution is driven by increased abundance of unmethylated transcripts and reduced abundance of highly methylated transcripts. Local hypermethylation near stop codon regions is associated with the upregulation of VIRMA.

5 Conclusion and outlook

This study reinvestigated the role of the m^6A methyltransferase METTL3 in UCB and provides novel insights into its m^6A epitranscriptomic landscape. Functional characterization of METTL3-deficient cells revealed that METTL3 is more likely to act as an oncogenic driver in UCB. However, LC-MS/MS, drug-response, and dependency analyses showed that METTL3 was also essential for cell viability in both cancerous and uroepithelial cells, which limits its therapeutic potential. Additional work in primary urothelial cultures, three-dimensional models, or *in vivo* systems will be necessary to determine to what extent METTL3 activity can be inhibited in uroepithelial tissue without causing adverse effects. The finding that METTL3 is an essential gene increases the likelihood of systemic toxicity upon inhibition, supposing a rather narrow therapeutic window. Strategies to improve the safety profile of METTL3-targeting therapies may involve approaches that limit systemic exposure, including tumor-targeted delivery systems, local administration, or the development of prodrugs that are selectively activated within the tumor microenvironment [171,172].

This thesis also established the first quantitative, base-resolution, transcriptome-wide m^6A maps of UCB and control tissues using GLORI-seq. This comparative analysis revealed systematic differences in the m^6A signatures between UCB and paratumoral tissue, including local m^6A hypermethylation near stop codons, which was associated with an upregulation of VIRMA. The VIRMA-associated hypermethylation signature is of particular interest, as it may affect APA, a post-transcriptional mechanism often dysregulated in cancer and known to affect transcript stability and isoform diversity. However, the underlying molecular mechanism linking m^6A, its regulators, and the polyadenylation machinery remains unresolved, particularly considering previously reported inconsistencies [20,33,72,80]. Future studies will be needed to investigate whether m^6A directly regulates the recruitment of polyadenylation factors or changes the accessibility of polyadenylation sites by affecting RNA structures. These questions could be addressed by combining METTL3 or VIRMA-deficient cell models with CLIP-seq of key polyadenylation factors, and by using structure-probing tools targeting polyadenylation sites [186]. To firmly establish the role of VIRMA in APA, 3’-UTR targeted sequencing methods (e.g.

3’READS or PolyA-seq) or reporter assays utilizing selectively mutated 3’-UTR m^6A sites could be applied to VIRMA-depleted UCB cells to assess changes in polyadenylation site usage [187,188].

Furthermore, the GLORI-seq data highlighted the diagnostic potential of m^6A profiling, as the m^6A profile alone was sufficient to clearly distinguish tumor from control samples. Given the limited availability of robust molecular biomarkers for UCB, m^6A profiling represents a promising alternative to address this unmet clinical need [6]. Notably, the development of GLORI 2.0 [189], which includes a PCR-based assay for the rapid and quantitative detection of m^6A at individual sites, offers the opportunity for clinically feasible applications. Since uroepithelial cells are continuously shed into urine, GLORI 2.0-PCR could be adapted for the non-invasive detection of m^6A biomarker sites in urinary RNA, offering a novel strategy for early diagnosis or monitoring of UCB. To advance the translational potential of m^6A profiling, future efforts should therefore focus on the clinical validation of presumable m^6A biomarker sites identified in this study. This could involve testing GLORI 2.0-PCR in urine samples from a large patient cohort to develop a non-invasive diagnostic assay for UCB. Preliminary experiments presented in the Expanded View Data section 7.3.1 demonstrated that m^6A can be detected by GLORI 2.0-PCR in total RNA from urine, highlighting the potential of this approach for developing non-invasive, urinary biomarkers for UCB.

In addition to exploring METTL3 and VIRMA as therapeutic targets, a more tumor-selective therapeutic approach could be the targeting of m^6A-dependent, pathophysiological condensates [56]. Recent studies have shown that m^6A-modified transcripts, such as MYC, can be sequestered and stabilized within nuclear condensates through interactions with m^6A readers like YTHDC1, thereby promoting tumor progression, as demonstrated in AML [127]. These pathophysiological condensates may offer more selective therapeutic entry points, especially if they are specific to the malignant context. Functional dissection of these structures, using tools such as live-cell imaging, mutant constructs of m^6A readers, or condensate-disrupting compounds, may uncover cancer-specific vulnerabilities that can be exploited therapeutically [190,191].

In support of this concept, a method for the enrichment of P-bodies, a class of phase-separated condensates involved in mRNA storage and decay, was developed in this study (Expanded View Data section 7.3.2). As a future line of investigation, this method could be employed to isolate P-bodies or other condensates, extract their RNA, and apply GLORI-seq to characterize the m^6A landscape of phase-separated compartments. This would offer novel insight into how m^6A modifications influence the localization, stability, and regulation of transcripts within condensates, and may help identify cancer-specific and condensate-associated m^6A targets for therapeutic intervention.

6 Materials and methods

6.1 Materials

Tab. 5: Chemicals, reagents, and enzymes.

Name	Manufacturer	Reference
Acetic acid glacial	Thermo Fisher Scientific	11337558
Agar	Fluka Analytical	05039
Agarose	Sigma-Aldrich	A9539
AKASOLV Aqua Care	Roth	KAC5.1
Ampicillin	Roth	HP62.1
Antarctic phosphatase	New England Biolabs	M0289S
ATP	Thermo Fisher Scientific	R0441
BamHI, FastDigest	Thermo Fisher Scientific	FD0054
Boric acid	Sigma-Aldrich	B0394
BshTI, FastDigest	Thermo Fisher Scientific	FD1464
Buffer solution pH 4	Roth	A517.2
Buffer solution pH 7	Roth	A518.3
Buffer solution pH 9.18	Roth	4294.1
Chloroform	VWR	22711.290
cOmplete Protease Inhibitor Cocktail	Roche	11697498001
Crystal violet	Sigma-Aldrich	C3886
D1000 ScreenTape reagents	Agilent Technologies	5067-5583
Distilled, DNase/RNase-free water	Thermo Fisher Scientific	10977035
DMSO	AppliChem	A3672,0250
DNA Gel Loading Dye (6x)	Thermo Fisher Scientific	R0611
dNTP mix 100 mM (25 mM each)	VWR	6100850-1000
Doxycycline	Sigma-Aldrich	D5207
DTT	Thermo Fisher Scientific	R0861
EcoRI, FastDigest	Thermo Fisher Scientific	FD0274
EDTA disodium salt dihydrate	Gerbu	1034
Esp3I, FastDigest	Thermo Fisher Scientific	FD0454
Ethanol absolute	Sigma-Aldrich	32205-M
Ethidium bromide solution (1%)	Roth	2218.2
FastAP Thermosensitive Phosphatase	Thermo Fisher Scientific	EF0651
Formamide deionized	Roth	P040.1
Glyoxal solution	Sigma-Aldrich	50649
HEPES	Gerbu	1009
Hydrochloric acid (37%)	Sigma-Aldrich	30721
Igepal CA-630 (Nonidet P40)	Sigma-Aldrich	I3021
Immobilon Western HRP Substrate	Merck	WBKLS0500
Isopropanol	Merck	1096341011

Lipofectamine 2000	Thermo Fisher Scientific	11668019
Magnesium chloride solution	Sigma-Aldrich	M1028
MES	Thermo Fisher Scientific	J60763.AP
Mesa Green qPCR MasterMix Plus for SYBR	Eurogentec	RT-SY2X-03+WOU
Methanol	Thermo Fisher Scientific	M-4000-PC17
Milk powder	Gerbu	1602.0500
NheI, FastDigest	Thermo Fisher Scientific	FD0973
PBS pH 7.4 (10x)	Gibco	70011-036
Phanta Max master Mix (Dye Plus, 2x)	Vazyme	P525-02
Ponceau S solution	Sigma-Aldrich	P7170
Potassium chloride	Roth	6781.1
Potassium chloride electrolyte solution	Hanna instruments	HI7082
primaAMP Taq DNA polymerase	Steinbrenner	SL-9601/02-smp
ProLong Gold Antifade Mountant with DNA Stain DAPI	Thermo Fisher Scientific	P36941
Protein Assay Dye Reagent Concentrate	Bio-Rad	5000006
Puromycin	Thermo Fisher Scientific	A1113803
Q5 High-Fidelity DNA Polymerase	New England Biolabs	M0491
RiboRuler Low Range RNA Ladder	Thermo Fisher Scientific	SM1831
RNA Gel Loading Dye (2x)	Thermo Fisher Scientific	R0641
RNAlater Stabilization Solution	Thermo Fisher Scientific	AM7021
RNA ScreenTape ladder	Agilent Technologies	5067-5577
RNA ScreenTape sample buffer	Agilent Technologies	5067-5578
RNaseOUT	Thermo Fisher Scientific	10777019
SDS pellets	Roth	CN30.3
Sodium acetate	Roth	6773.2
Sodium azide	Sigma-Aldrich	S2002
Sodium chloride	Thermo Fisher Scientific	15855188
Sodium hydroxide pellets	Sigma-Aldrich	30620
Sodium nitrite	Thermo Fisher Scientific	15633430
STM2457	MedChemExpress	HY-134836
Sucrose	MP Biomedicals	821713
SYBR Green I Nucleic Acid Gel Stain	Lonza Bioscience	50513
T4 DNA Ligase	New England Biolabs	M0202S
T4 Polynucleotide Kinase	New England Biolabs	M0201S
Triethylammonium acetate buffer	Thermo Fisher Scientific	90358
Triton X-100	Sigma-Aldrich	X100
Trizma base	Sigma-Aldrich	T1503
TRIzol Reagent	Thermo Fisher Scientific	15596026
Tryptone (peptone from casein)	VWR	84610.0500

Tween 20	Sigma-Aldrich	P1379
Yeast extract	Gerbu	1133.0500

Tab. 6: Commercial kits.

Name	Manufacturer	Reference
Caspase-Glo 3/7 Assay kit	Promega	G8091
Cell Titer-Glo Luminescent Cell Viability Assay kit	Promega	G7571
Direct RNA-seq Kit	Oxford Nanopore	SQK-RNA004
Dynabeads mRNA Purification Kit	Thermo Fisher Scientific	61006
GFP-Trap Magnetic Particles M-270 Kit	Proteintech	gtdk-20
HiSpeed Plasmid Midi Kit	Qiagen	12643
Monarch PCR & DNA Cleanup Kit (5 µg)	New England Biolabs	T1030
NEBNext Magnesium RNA Fragmentation Module	New England Biolabs	E6150S
NEBNext Multiplex Oligos for Illumina (Index Primer Set 1)	New England Biolabs	E7335S
NEBNext Multiplex Oligos for Illumina (Index Primer Set 3)	New England Biolabs	E7710S
NEBNext Small RNA Library Prep Set for Illumina	New England Biolabs	E7330S
Plasmid Maxi Kit	Qiagen	12163
Plasmid Midi Kit	Qiagen	12143
QIAprep Spin Miniprep Kit	Qiagen	27106
QIAquick Gel Extraction kit	Qiagen	28704
RNA Clean & Concentrator-5 Kit	Zymo Research	R1013
SuperScript III First-Strand Synthesis System	Thermo Fisher Scientific	18080-044
ZR Urine RNA Isolation Kit	Zymo Research	R1038

Tab. 7: Consumables and labware.

Name	Manufacturer	Reference
1 mL syringe	Thermo Fisher Scientific	10017781
10 cm petri dish	Greiner	664160
10 mL serological pipettes	Greiner	607180
10 mL syringe	Becton Dickinson	9.410 403
10 µL filter tips	Nerbe plus	06-602-5300
1000 µL filter tips	Nerbe plus	06-693-5300
15 cm petri dish	Greiner	639960
15 mL Falcon tube	Greiner	188271
20 mL syringe	Becton Dickinson	6.052 157
20 µL filter tips	Nerbe plus	06-622-5300

200 µL filter tips	Nerbe plus	06-662-5300
24-well-plate	Greiner	662160
25 mL serological pipette	Corning	4489
5 mL serological pipettes	Greiner	606180
5 mL syringe	Becton Dickinson	7.619 784
50 mL Falcon tube	Greiner	227261
50 mL serological pipette	Corning	4490
50 mL syringe	Becton Dickinson	300865
6-well-plate	Greiner	657160
96-well-plate	Thermo Fisher Scientific	2900136101
Bio-Dot SF Filter Paper	Bio-Rad	1620161
Cell Counting slides for TC10	Bio-Rad	1450011
Cell scraper	Faust Lab Science	TPP99004
Cell strainer (70 µm)	Corning	352350
Cellulose acetate filters (0.45 µm)	Sartorius	1110647ACN
ClipTip Filtered 384-Format Pipette Tips	Thermo Fisher Scientific	94420153
Cryotube vials	Thermo Fisher Scientific	377267
D1000 ScreenTape	Agilent Technologies	5067-5582
Duran bottle, 100 mL	Schott	218012409
Duran bottle, 1000 mL	Schott	218015406
Duran bottle, 250 mL	Schott	218013602
Duran bottle, 500 mL	Schott	218014401
Duran measuring cylinder, 100 mL	Schott	213962408
Duran measuring cylinder, 1000 mL	Schott	213965405
Duran measuring cylinder, 500 mL	Schott	213964409
E1-ClipTip Electronic Multichannel Pipettes	Thermo Fisher Scientific	4671040BT
Flow cell for direct RNA-seq	Oxford Nanopore	FLO-MIN004RA
FrameStar 384 Well Skirted PCR Plate	4titude	4ti-0381
Funnel	VITLAB	709
Gel releaser	Bio-Rad	1653320
Kimtech precision wipes	Roth	AA64.1
Laboratory film	Amcor Limited	PM-996
Magnetic stir bar, 12 mm length	Roth	XA17.1
Magnetic stir bar, 25 mm length	Roth	XA18.1
Microcuvettes	Sigma-Aldrich	BR759015
Micro tube 1.5 mL	Sarstedt	72.690.001
Micro tube, 2.0 mL	Sarstedt	72.691
Midisart 2000	Sartorius	17804NPE
Mini Cell Buffer Dam	Bio-Rad	1653130
Mini-PROTEAN Tetra Companion Running Module	Bio-Rad	1658038

Mini-PROTEAN Tetra Electrode Assembly	Bio-Rad	1658037
Mini-PROTEAN TGX Precast Gels, 12%, 10-well comb, 50 µL	Bio-Rad	4561044
Mini-PROTEAN TGX Precast Gels, 12%, 12-well comb, 20 µL	Bio-Rad	4561045
Mini-PROTEAN TGX Precast Gels, 7.5%, 15-well comb, 15 µL	Bio-Rad	4561026
Novex TBE Gels, 8%	Thermo Fisher Scientific	EC6215BOX
Pasteur pipettes	BRAND	747720
PCR tubes	Kisker Biotech	G003-SF
Pellet pestles, RNase-free and disposable	DWK Life Sciences	749521-1590
Pipette, 0.2 - 2 µL	Gilson	FA10001M
Pipette, 100 - 1000 µL	Gilson	FA10006M
Pipette, 2 - 20 µL	Gilson	FA10003M
Pipette, 20 - 200 µL	Gilson	FA10005M
primaSeal-qPCR	Steinbrenner	SL-PS-qPCR2
QuadriPERM chamber	Sarstedt	94.6077.307
Reagent reservoir	Gilson	GILSF267660
RNA ScreenTape	Agilent Technologies	5067-5576
Rubber bulb for Pasteur pipettes	Sigma-Aldrich	Z615927
Scalpel (No. 21)	Feather safety razor	02.001.30.021
Spin-X Centrifuge Tube Filters	Sigma-Aldrich	CLS8162-96EA
StarGuard Comfort gloves	Starlab Group	SG-C-S
TissueRuptor Disposable Probes	Qiagen	990890
Trans-Blot Turbo Transfer Pack	Bio-Rad	1704158
Tweezer	Merck	11714474
Weighing boats (90x115 mm)	Macherey-Nagel	186002

Tab. 8: Technical devices.

Name	Manufacturer
2200 TapeStation	Agilent Technologies
Agarose gel electrophoresis cell	Bio-Rad
Automated Cell Counter TC10	Bio-Rad
Axio microscope	Zeiss
Bio-Dot Microfiltration Apparatus	Bio-Rad
Cell Culture hood HERA safe KS	Thermo Fisher Scientific
EV265/EV835 Electrophoresis Power Supply	Consort
GloMax Explorer Multimode Microplate Reader	Promega
Heracell 150i CO2 Incubator	Thermo Fisher Scientific
IKA MS 3 vortexer	IKA
Inverter microwave	Sharp
LightCycler 480	Roche
M6 ECL ChemoStar fluorescence imaging system	Intas
Mini centrifuge 3-1810	neoLab Migge

Mini-PROTEAN Tetra Vertical Electrophoresis Cell	Bio-Rad
MinION Mk1B	Oxford Nanopore
NanoDrop 2000/2000c spectrophotometer	Thermo Fisher Scientific
pH/ORP Meter HI 2211	Hanna instruments
Pipetboy 2	Integra Biosciences
Thermocycler T3000	Biometra
TissueRuptor II	Qiagen
Trans-Blot Turbo Transfer System	Bio-Rad
Transluminator U:GENIUS3	Syngene
TW12 Water bath	Julabo
Z1 Coulter Particle Counter	Beckman Coulter

Tab. 9: Buffers and solutions.

Application	Name	Composition
Agarose gel electrophoresis	TAE (50x)	40 mM Tris 2 mM EDTA 20 mM acetic acid Adjusted to pH 8.5
CFAPP	Fractionation buffer	10 mM HEPES (pH 7.9) 10 mM KCl 1.5 mM $MgCl_2$ 340 mM Sucrose 10% Glycerol 1 mM DTT 0.1% Triton-X-100 Prepared in water; Buffer was supplemented with cOmplete Protease Inhibitor Cocktail and RNaseOUT (80 U/mL)
CFAPP	Washing buffer	10 mM Tris 150 mM NaCl 0.5 mM EDTA (pH 8.0) 0.018% sodium azide 0.05% Igepal CA-630 Prepared in water
Colony formation assay	0.5% crystal violet solution	0.5% Crystal violet 20% Methanol Prepared in water
GLORI	Deamination buffer (V = 50 µL)	1.5 M $NaNO_2$ 80 mM MES (pH 6.0) 1.76 M Glyoxal solution Prepared in water
GLORI and GLORI 2.0	Deprotection buffer (V = 50 µL)	500 mM Triethylammonium acetate (pH 8.6) 47.5% Deionized formamide Prepared in water
GLORI	Protection buffer	1.32 M Glyoxal solution

	(V = 40 µL)	50% DMSO Prepared in water
GLORI	TBE buffer	1.0 M Tris 1.0 M Boric acid 20 mM EDTA (pH 8.0) Prepared in water
GLORI 2.0	Deamination buffer (V = 50 µL)	1.0 M $NaNO_2$ 40 mM MES (pH 6.0) 2.28 M Glyoxal solution 5 µL saturated boric acid Prepared in water
Western blotting	Lysis buffer	20 mM Tris-HCl (pH 7.5) 150 mM NaCl 1 mM EDTA 1% Triton-X-100 Buffer was supplemented with cOmplete Protease Inhibitor Cocktail

Tab. 10: Antibodies.

Name	Application	Working concentration	Manufacturer	Reference
4E-T (B-3)	Immunofluorescence Western blotting	1:500 1:100	Santa Cruz Biotechnology	sc-393788
β-Actin monoclonal antibody	Western blotting	1:1,000	Sigma-Aldrich	A5316
Chicken anti-Rabbit IgG (H+L) Cross-Adsorbed Secondary Antibody, Alexa Fluor 594	Immunofluorescence	1:500	Thermo Fisher Scientific	A-21442
CRISPR/Cas9 monoclonal antibody	Western blotting	1:1,000	Epigentek	A-9000
DCP1A Polyclonal antibody	Western blotting	1:1,000	Proteintech	22373-1-AP
DDX6 Polyclonal antibody	Western blotting	1:1,000	Proteintech	14632-1-AP
DDX6 / RCK (E-12)	Immunofluorescence	1:500	Santa Cruz Biotechnology	sc-376433
Donkey anti-goat IgG-HRP	Western blotting	1:10,000	Santa Cruz Biotechnology	sc-2020
Donkey anti-Mouse IgG (H+L) Secondary Antibody, HRP	Western blotting	1:10,000	Thermo Fisher Scientific	A16011
Donkey anti-rabbit	Western blotting	1:10,000	Santa Cruz	sc-2313

IgG-HRP			Biotechnology	
EDC4 Polyclonal antibody	Western blotting	1:1,000	Proteintech	17737-1-AP
Goat anti-Mouse IgG (H+L) Cross-Adsorbed Secondary Antibody, Alexa Fluor 594	Immunofluorescence	1:500	Thermo Fisher Scientific	A-11005
LSM14A Polyclonal antibody	Western blotting	1:1,000	Proteintech	18336-1-AP
METTL3 polyclonal antibody	Western blotting	1:1,000	Proteintech	15073-1-AP
VIRMA Polyclonal antibody	Western blotting	1:1000	Proteintech	25712-1-AP
YTHDF2 Polyclonal antibody	Immunofluorescence	1:500	Proteintech	24744-1-AP

Tab. 11: Bacterial strains.

Name	Application	Source
One Shot Stbl3 Chemically Competent *E. coli*	Cloning	Thermo Fisher Scientific

Tab. 12: Cell lines.

Name	Cell type	Source
HEK293T	Human embryonic kidney cell line	European Collection of Authenticated Cell Cultures (ECACC)
RT112/84	UCB cell line	ECACC
RT4	UCB cell line	ECACC
T24	UCB cell line	ECACC
UM-UC-3	UCB cell line	ECACC
UROtsa	Uroepithelial cell line	ECACC

Tab. 13: Cell culture media and supplements.

Name	Manufacturer	Reference
DMEM, high glucose, pyruvate medium	Gibco	41966052
DMSO	AppliChem	A3672,0250
Fetal bovine serum	Gibco	10500064
McCoy's 5A (Modified) medium	Gibco	26600023
PBS pH 7.4 (1x)	Gibco	10010-015
Penicillin-Streptomycin (P/S,	Gibco	15140-122

10,000 U/mL)		
RPMI 1640 medium	Gibco	A1049101
Trypsin-EDTA (0.25%)	Gibco	25200056

Tab. 14: Primers and oligonucleotides. Primers were purchased from Sigma-Aldrich.

Name	**Application**	**Sequence (5'→3')**
28S_rRNA_F	GLORI 2.0	ACACTCTTTCCCTACACGACGCTCTTCCGATCTNNNNGGGCGGTGCGCCTGTC
28S_rRNA_R	GLORI 2.0	GACTGGAGTTCAGACGTGTGCTCTTCCGATCTGAGCCCGCCCCAGGACA
28S_rRNA_Ctrl_F	GLORI 2.0	ACACTCTTTCCCTACACGACGCTCTTCCGATCTNNNNCGGTGGCCTCCGTTGCC
28S_rRNA_Ctrl_R	GLORI 2.0	GACTGGAGTTCAGACGTGTGCTCTTCCGATCTCCGGGGACCCGAACCCGA
Anti-METTL3 sgRNA1_F	Cloning for METTL3 KO	AGACTAGGATGTCGGACACG
Anti-METTL3 sgRNA1_R	Cloning for METTL3 KO	CGTGTCCGACATCCTAGTCT
Anti-METTL3 sgRNA2_F	Cloning for METTL3 KO	CTGGTGGCCCTAAGCCCAGC
Anti-METTL3 sgRNA2_R	Cloning for METTL3 KO	GCTGGGCTTAGGGCCACCAG
Anti-METTL3 sgRNA3_F	Cloning for METTL3 KO	ATGCTGACCATTCCAAGCTC
Anti-METTL3 sgRNA3_R	Cloning for METTL3 KO	GAGCTTGGAATGGTCAGCAT
Anti-METTL3 sgRNA4_F	Cloning for METTL3 KO	AAGTGCAAGAATTCTGTGAC
Anti-METTL3 sgRNA4_R	Cloning for METTL3 KO	GTCACAGAATTCTTGCACTT
Anti-VIRMA shRNA1	VIRMA KD	TTCTTCTAAAGCTGTTACC
Anti-VIRMA shRNA2	VIRMA KD	ATTCTCATCATATTCCAGG
CAND1_F	GLORI 2.0	ACACTCTTTCCCTACACGACGCTCTTCCGATCTNNNNGTCTGCTGGCTTGGGGTC
CAND1_R	GLORI 2.0	GACTGGAGTTCAGACGTGTGCTCTTCCGATCTCGGCGAACAAACACCCAAC
CCP110_F	CFAPP	CTTCACAGAGCAGAGTGCCT
CCP110_R	CFAPP	ATTGTCGCAACATTTGGCCG
EIF2A_F	GLORI 2.0	ACACTCTTTCCCTACACGACGCTCTTCCGATCTNNNNTGCGGCCTGCTGTGGC
EIF2A_R	GLORI 2.0	GACTGGAGTTCAGACGTGTGCTCTTCCGATCTCAAACCCAGCCAACACCAAC
GLORI2.0_RT_R	GLORI 2.0	d(VVVVVVVV), V = A, G, or C
GLORI_Sanger	GLORI 2.0	AATGATACGGCGACCACCGAG
GLORI-Spike-In_F	GLORI	ACGGCGACCACCGAGATCTACACTCTTTCCCTGGCGCGGCGGGCGTGGCGC

GLORI-Spike-In_R	GLORI	GAGTCAGGTCCATTGATGCACCAAACCAACCAACCAAAAGCCGCACGCGCACAGCGGCCA
GNB2L1_F	CFAPP	GTACGGAAGACGGGACTGTG
GNB2L1_R	CFAPP	GGCGAGCCCCATGATACATT
HIST1H1E_F	CFAPP	CGTATCTTTGGCCGCTCTCA
HIST1H1E_R	CFAPP	GCTCTTGAGACCCAGCTTGA
ILF3_F	GLORI 2.0	ACACTCTTTCCCTACACGACGCTCTTCCGATCTNNNNGCCCGTCCTGTGGCCC
ILF3_R	GLORI 2.0	GACTGGAGTTCAGACGTGTGCTCTTCCGATCTAACGGCAACCAACAAACCA
Illumina_Primer_F	GLORI 2.0	AATGATACGGCGACCACCGAGATCTACACTCTTTCCCTACACGACGCTCTTCCGATCT
Illumina_Primer_Index	GLORI 2.0	CAAGCAGAAGACGGCATACGAGATCGTGATGTGACTGGAGTTCAGACGTGTGCTCTTCCGATCT
KMT2C_F	CFAPP	CTTGCCTGTTCTCAGTGTGG
KMT2C_R	CFAPP	TGCACTCAAGACACCTCCAA
LSM14A_Eco_F	Cloning for CFAPP	ATAGTGAATTCATGAGCGGGGGCACCCCTTA
LSM14A_Bam_R	Cloning for CFAPP	AATAGGATCCTTAGGGTCCAAAAGCTGTGG
METTL3_F	METTL3 expression analysis	CAGGCTCAACATACCCGTACT
METTL3_R	METTL3 expression analysis	ACATTCTCTCCCCAACTCCA
Non-targeting Scr sgRNA_F	Cloning for METTL3 KO	GCTGACGGCGAGCTTTAGGC
Non-targeting Scr sgRNA_R	Cloning for METTL3 KO	GCCTAAAGCTCGCCGTCAGC
RAD21_F	CFAPP	GAGCAGCGTGGAGAGTATCA
RAD21_R	CFAPP	GTCTGCAAGAAGGTATTTGGCT
SMC3_F	CFAPP	ACCTCCTTGAAAGCGCTGG
SMC3_R	CFAPP	GCTGTTGCCATCTGGTTGAT
SPEN_F	CFAPP	GGACGTTATGAGCGGAGACT
SPEN_R	CFAPP	GTCCGATCAAATCCTCCCGT
Spike-In_F	GLORI	ACGGCGACCACCGAGATCTACACTCTTTCCCTAGCGCAGCGAACATGACAC
Spike-In_R	GLORI	GAGTCAGGTCCATTGATGCACCAAACCAACCAACCAAAAGCTGCACGTGCATAGCGGCTA
Spike-In RNA	GLORI	AGCGCAGCGAACAUGACACGUGCUCAACAGUGUAGUUGGACUUCCUCGCAUCUAGCCGCUAUGCACGUGCAGCU
Spike-In_Sanger	GLORI	ACGGCGACCACCGAGATCTA
TUBA1B_F	CFAPP	TCGCCTCCTAATCCCTAGCC
TUBA1B_R	CFAPP	CCGTGTTCCAGGCAGTAGAG

Tab. 15: Plasmids.

Name	Application	Source
pLentiCRISPR v2	Cloning for METTL3 KO, Lentivirus production	Addgene (Plasmid #52961)
pLVX-GFP-HA-FLAG	Cloning for CFAPP	Provided by Dr. Simge Kelekci (Division of Cancer Epigenomics, German Cancer Research Center, Heidelberg), vector map in Appendix 7.4.1
pMD2.G	Lentivirus production	Addgene (Plasmid #12259)
psPAX2	Lentivirus production	Addgene (Plasmid #12260)
TLCV2	Cloning for METTL3 KO, Lentivirus production	Addgene (Plasmid #87360)

Tab. 16: Software and computational tools.

Name	Version	Application
2200 TapeStation Controller		Gel electrophoresis
bedtools getfasta	2.25.0	Extract sequences from FASTA files based on genomic coordinates
bowtie	1.3.0	Alignment of sequencing reads
ChemoStarTS		Image acquisition and analysis
DaPars		Analysis of APA events
DeSeq2	1.42.0	Differential gene expression analysis
DiffLogo	2.20.0	Sequence motif analysis
Dorado	7.2.13	Base-calling from direct RNA-seq
EnsDb.Hsapiens.v86	2.99.0	Provides human gene annotations
featureCounts	2.0.6	Counting of aligned sequencing reads
GloMax Explorer Multimode Microplate Reader Software		Measurements for Cell Titer-Glo Luminescent Cell Viability Assay and Caspase-Glo 3/7 Assay kits (Promega)
GLORI-tools	1.0.0	GLORI-seq analysis
GraphPad Prism	10	Data analysis and statistics
HISAT2	2.2.1	Alignment of sequencing reads
HOMER	4.11	Sequence motif analysis
ImageJ		Image analysis
ImageJ plugin ColonyArea [192]		Colony formation assay analysis
LightCycler 480 Software		qRT-PCR analysis
methylSig	1.7.0	Differential methylation analysis
Modkit	0.2.6	Modification calling from direct RNA-seq
Microsoft Office Standard 2016	2311	Data analysis and writing
MinKNOW	23.11.5	Direct RNA-seq analysis
NanoDrop 2000		DNA and RNA concentration measurements
Python	3.19.1	Computational analysis
R	4.1.3	Computational analysis
RStudio	2022.02.1	Computational analysis

samtools	1.19	Handling sequencing alignment files
ShinyGO [193]	0.82	Gene ontology analysis
STAR	2.7.10a	Alignment of sequencing reads
TapeStation Analysis		Gel electrophoresis analysis
Trim Galore	0.6.6	Sequencing read trimming
uGenius		Gel electrophoresis analysis

6.2 Methods

6.2.1 Patient samples

All patient samples were provided by Dr. Malin Nientiedt, Dr. Katja Nitschke, Dr. Manuel Neuberger, and Prof. Dr. Philipp Erben (Department of Urology and Urosurgery, Medical Faculty Mannheim, University of Heidelberg, Mannheim). Samples were diagnosed by a uropathologist, and tumors were characterized according to the TNM classification for bladder cancer by the Union for International Cancer Control (UICC 2017). Tumors with variant histopathological findings other than urothelial carcinoma were excluded.

For the LC-MS/MS analyses, UCB tissue samples were obtained and analyzed as described in Koch *et al.*, 2023 [194]. For the comparative GLORI analyses, tumor samples were obtained from TURBT specimens. Paratumoral tissue was taken from cystectomy specimens. Patient samples were stored at - 20 °C in RNAlater stabilization solution (Thermo Fisher Scientific) until further processing (section 6.2.8). Clinicopathological data of all cohorts used in this work are provided in Tables 2 and 4.

The study was performed in adherence to the Declaration of Helsinki, and all patients gave approval to participate in the study. Approval of the Ethics Committee II of Heidelberg University (reference numbers 2013-845R-MA and 2015-549N-MA) was obtained.

6.2.2 Cell culture

All cell lines were authenticated and cultured according to ATCC guidelines. UROtsa cells were cultured in RPMI 1640 medium supplemented with 5% FBS and 1% penicillin/streptomycin (P/S). HEK293T, RT112/84, and UMUC-3 cell lines were cultured in DMEM, high glucose, pyruvate medium supplemented with 10% FBS and 1% P/S. RT4 and T24 cells were cultured in McCoy’s 5A (modified) medium supplemented with 10% FBS and 1% P/S. The cell culture media and supplements were purchased from Gibco. All cell lines were cultivated as adherent monolayers in a humidified incubator at 37 °C and an atmosphere of 5% CO_2.

6.2.3 Generation of METTL3 KO and VIRMA KD cell lines

For inserting the anti-METTL3 sgRNAs into the TLCV2 and pLentiCRISPR v2 vectors, the vectors were cut and dephosphorylated using the Esp3I (Thermo Fisher Scientific) and FastAP Thermosensitive Phosphatase (Thermo Fisher Scientific) enzymes. The digestion reactions were separated by agarose gel electrophoresis, and the target bands were extracted using the QIAquick Gel Extraction kit (Qiagen). Anti-METTL3 and non-targeting Scr sgRNAs (designated as anti-METTL3 sgRNAs1-4_F/R and non-targeting Scr sgRNA_F/R in Tab. 14) were phosphorylated by the T4 Polynucleotide Kinase (New England Biolabs) and annealed ON at 37 °C. Then, the anti-METTL3 sgRNAs were ligated into the cut vector backbones using the T4 DNA Ligase (New England Biolabs). Ligations were transformed into One Shot Stbl3 Chemically Competent *E. coli* cells (Thermo Fisher Scientific) by heat-shock. Transformed clones were selected using LB agar plates supplemented with ampicillin. Plasmid constructs from single clones were purified using Mini, Midi, and Maxi Prep Kits (Qiagen). Cloning was verified by Sanger Sequencing (Eurofins).

Lentiviral shRNA constructs for VIRMA KD were purchased from Horizon Discovery. Sequences for the anti-VIRMA shRNAs are given in Tab. 14 and comprise clones V2LHS_96736 (RHS4430-200156255, Horizon Discovery) and V2LHS_96733 (RHS4430-200172168, Horizon Discovery). Sequence information for the non-targeting shRNA control construct was not provided by the manufacturer. Constructs were obtained as bacterial glycerol stocks. Plasmid constructs from single clones were purified using Mini, Midi, and Maxi Prep Kits (Qiagen).

For lentivirus production, HEK293T cells were transfected with the recombinant plasmid constructs using Lipofectamine 2000 (Thermo Fisher Scientific). Transfected HEK293T cells were cultured for 48 hours. Virus-containing medium supernatants from transfected HEK293T cells were filtered using cellulose acetate filters (0.45 µm, Sartorius) and added to target cells for transduction. Transduction was performed for 48 hours. Cells that were transduced with the TLCV2 constructs were selected for one week using puromycin (Thermo Fisher Scientific). Cells that were transduced with the pLentiCRISPR v2 constructs were sorted by Dr. Monika Langlotz (Flow Cytometry and FACS Core Facility, Center for Molecular Biology Heidelberg).

6.2.4 Cell proliferation, colony formation, and Caspase 3/7 activity assays

In cell proliferation assays using TLCV2 Scr and METTL3 KO cell pools, 8 * 10^3 T24 cells and 12 * 10^3 UM-UC-3 cells per well were seeded into 12-well plates. Cells were counted for a total of 96 hours in 24-hour intervals using the Z1 Coulter Particle Counter (Beckman Coulter).

In cell proliferation assays using WT as well as pLentiCRISPR v2 Scr and METTL3 KO clones, 750 T24 cells and 1,500 UM-UC-3 cells per well were seeded into opaque 96-well plates. In cell proliferation assays using shCtrl and VIRMA KD cells, 1,500 RT4 cells and 1,000 UM-UC-3 cells per well were seeded into opaque 96-well plates. Cells were counted for a total of 72 - 96 hours in 24-hour intervals using the Cell Titer-Glo Luminescent Cell Viability Assay kit (Promega) on a GloMax Explorer Multimode Microplate Reader (Promega).

In colony formation assays using WT, TLCV2 Scr and METTL3 KO cells as well as pLentiCRISPR v2 Scr and METTL3 KO cells, 500 T24 cells and 1,000 UM-UC-3 cells per well were seeded into 6-well plates. In colony formation assays using shCtrl and VIRMA KD cells, 1,000 RT4 cells and 500 UM-UC-3 cells per well were seeded into 6-well plates. Cells were incubated for 1.5 weeks and fixed using methanol for 10 min on ice. Colonies were stained by incubation in 0.5% crystal violet solution (Tab. 9) at RT for 10 min. Colony formation was quantified using ColonyArea [192].

In Caspase 3/7 activity assays using WT, TLCV2 Scr and METTL3 KO cells as well as pLentiCRISPR v2 Scr and METTL3 KO cells, 10^4 T24 and UM-UC-3 cells per well were seeded into opaque 96-well plates. In Caspase 3/7 activity assays using shCtrl and VIRMA KD cells, 10^4 RT4 and UM-UC-3 cells per well were seeded into opaque 96-well plates. Assays were quantified after 48 hours of incubation using the Caspase-Glo 3/7 Assay kit (Promega). To compensate for differences in cell numbers, a cell proliferation measurement was performed for normalization of the Caspase 3/7 activity measurements by using the Cell Titer-Glo Luminescent Cell Viability Assay kit (Promega). All measurements were conducted on a GloMax Explorer Multimode Microplate Reader (Promega).

In all functional assays using the inducible TLCV2 METTL3 KO system, cells were induced after attachment using 100 ng/mL doxycycline.

In all functional assays using the STM2457 METTL3 inhibitor (MedChemExpress), cells were treated with DMSO or STM2457 after attachment.

6.2.5 STM2457 response assay

In inhibitor response assays, $4 * 10^3$ UROtsa, $5 * 10^3$ RT4, $3.5 * 10^3$ RT112/84, $2 * 10^3$ T24, and $2.5 * 10^3$ UM-UC-3 WT cells per well were seeded into opaque 96-well plates. After attachment, cells were treated with DMSO or STM2457 (0.01 – 200 µM) and cultured for 72 hours. Cell viability was quantified using the Cell Titer-Glo Luminescent Cell Viability Assay kit (Promega) on a GloMax Explorer Multimode Microplate Reader (Promega). Also, another cell viability measurement was performed after attachment for normalization in order to compensate for differences during cell seeding.

6.2.6 Liquid chromatography-tandem mass spectrometry (LC-MS/MS)

LC-MS/MS experiments and analyses were performed by Dr. Martina Krämer (Helm lab, Institute of Pharmaceutical and Biomedical Sciences, Johannes Gutenberg University, Mainz) as described in Koch *et al.*, 2023 [194].

6.2.7 Direct RNA-seq

300 ng of non-fragmented HEK293T cell mRNA were sequenced using a direct RNA-seq kit on the MinION Mk1B platform (Oxford Nanopore). From the raw data, base-calling was performed using Dorado (version 7.2.13). Dorado is available on GitHub: https://github.com/nanoporetech/dorado. Dorado-based base-calling was performed by Dr. Panagiotis Provataris (German Cancer Research Center, Heidelberg). Modification sites were detected using Modkit (version 0.2.6). Modkit is available on GitHub: https://github.com/nanoporetech/modkit. All analysis steps were performed in R (version 4.1.3) using RStudio (version 2022.02.1).

6.2.8 RNA isolation and preparation for GLORI

Principally, RNA isolation and preparation for GLORI were performed as described in Liu *et al.*, 2023 [27].

For sequencing trials using cell line samples, total RNA was isolated using TRIzol. Small RNA fractions were depleted using the MEGAclear Transcription Clean-Up Kit (Thermo Fisher Scientific). Enrichment of mRNA was performed twice using the Dynabeads mRNA Purification Kit (Thermo Fisher Scientific). mRNA was then fragmented by incubation for 3 min at 94 °C using the NEBNext Magnesium RNA Fragmentation Module (New England Biolabs). The fragmentation step was performed differently from the published version of the protocol, which described mRNA fragmentation for 4 min at 94 °C [27]. Fragmented mRNA was then DNase I-treated and purified by the RNA Clean & Concentrator-5 kit (Zymo Research). The concentration, as well as the average and peak mRNA fragment lengths, were determined by TapeStation (Agilent Technologies).

For sequencing trials using patient samples, tissue samples were homogenized by disruption using the TissueRuptor II (Qiagen) and total RNA isolated with TRIzol. All subsequent processing steps were performed as described above for cell line samples.

6.2.9 GLORI – RNA protection, deamination, and deprotection

Principally, the following steps were performed as described in Liu *et al.*, 2023 [27].

For RNA protection, 100 - 200 ng of fragmented mRNA supplemented with a synthetic Spike-In RNA (Tab. 14) or 100 ng of pure Spike-In RNA were added into the protection buffer (Tab. 9) and incubated for 30 min at 50 °C in a thermal cycler. The RNA was further stabilized by adding 10 µL of freshly prepared saturated boric acid at RT, followed by incubation for 30 min at 50 °C in a thermal cycler. Protected RNA was then added to 50 µL of freshly prepared deamination buffer (Tab. 9), mixed by pipetting, and incubated for 8 hours at 16 °C in a thermal cycler. After deamination, RNA was purified by ethanol precipitation overnight at - 80 °C. Pelleted RNA was washed twice using 75% ethanol and air-dried for 5 min at RT. Then, the RNA pellet was resuspended in 50 µL of deprotection buffer (Tab. 9) and incubated for 10 min at 95 °C in a thermal cycler. Deprotected RNA was purified by ethanol precipitation for 30 min at - 80 °C. Pelleted RNA was washed twice using 75% ethanol and air-dried for 5 min at RT. The RNA pellet was then resuspended in 50 µL of water and further purified using the RNA Clean & Concentrator-5 kit (Zymo Research).

6.2.10 Assessing A→G conversion by GLORI-PCR using a synthetic RNA oligo

Untreated, GLORI-treated, or GLORI 2.0-treated RNA were mixed with 1 µL of 2 µM specific reverse primers that either considered A→G conversion or not, depending on the treatment of the RNA (designated as GLORI-Spike-In_R and Spike-In_R in Tab. 14). RNA was reverse-transcribed into cDNA by the SuperScript III First-Strand Synthesis System (Thermo Fisher Scientific). Then, cDNAs were further amplified via PCR using the primaAMP Taq DNA polymerase (Steinbrenner) and forward primers that either considered A→G converted or not, depending on the treatment of the RNA (designated as GLORI-Spike-In_F and Spike-In_F in Tab. 14), as well as reverse primers that were already used for the previous reverse transcription reaction. During PCR, the forward primers also attached a sequence complementary to a sequencing primer that was used for subsequent Sanger Sequencing analysis (designated as Spike-In_Sanger in Tab. 14). The PCR reactions were separated by agarose gel electrophoresis, and the target bands extracted using the QIAquick Gel Extraction kit (Qiagen). Amplicons were then sent for Sanger Sequencing (Eurofins).

6.2.11 Preparation and sequencing of GLORI libraries

For sequencing library preparation, a two-step RNA end-repair protocol was pursued. RNA 3'-end dephosphorylation was performed by Antarctic phosphatase (New England Biolabs) treatment in a total reaction volume of 20 µL. The reaction was incubated for 30 min at 37 °C and inactivated for 2 min at 80 °C. Subsequently, RNA 5'-end phosphorylation was performed by T4 Polynucleotide Kinase (New England Biolabs) treatment in a total reaction volume of

50 µL. The reaction was incubated for 30 min at 37 °C, inactivated for 20 min at 65 °C, and purified using the RNA Clean & Concentrator-5 kit (Zymo Research). GLORI-seq libraries were then prepared using the NEBNext Small RNA Library Prep Set for Illumina in combination with the NEBNext Multiplex Oligos for Illumina (Index Primer Sets 1 and 3, New England Biolabs). Size selection of the libraries was performed via TBE-PAGE (Tab. 9) using 8% TBE polyacrylamide gels (Thermo Fisher Scientific), selecting sequencing competent molecules in a size range of 160 - 250 bp. Average peak size and concentration of the libraries were determined by TapeStation (Agilent Technologies). Libraries were either sequenced on a MiSeq platform (Illumina) applying a 150 bp paired-end sequencing protocol or sequenced on a NovaSeq 6000 platform (Illumina) applying a 100 bp paired-end sequencing protocol. Sequencing was performed by the Next Generation Sequencing Core Facility of the German Cancer Research Center, Heidelberg. Raw sequencing data were then trimmed using Trim Galore (version 0.6.6) and further processed by the GLORI-tools pipeline (version 1.0.0) as described [27]. GLORI-tools is available on GitHub: https://github.com/liucongcas/GLORI-tools. Parameters for the selection of m^{6}A sites were set as follows: ≥ 5 variant nucleotides, ≥ 15 coverage of A and G bases, ≥ 0.1 A rate (methylation level ≥ 10%). GLORI-tools was executed using the following software: Python (version 3.10.1), samtools (version 1.19), STAR (version 2.7.10a), and bowtie (version 1.3.0). The reference files from the human genome (GRCh38) and human transcriptome (GCF_000001405.39) were obtained from UCSC. All analysis steps were performed in R (version 4.1.3) using RStudio (version 2022.02.1).

6.2.12 Sequence motif analysis using HOMER

The coordinates and flanking sequences of GLORI-derived m^{6}A sites were extracted using bedtools getfasta (version 2.25.0) and the human genome reference file (GRCh38). Sequence motifs were identified using Hypergeometric Optimization of Motif EnRichment (HOMER, version 4.11). For visualization, the motif representations were converted into position weight matrices using DiffLogo (version 2.20.0).

6.2.13 m^{6}A cluster analysis

To investigate cluster distances, the transcriptomic coordinates of the detected m^{6}A sites were identified using EnsDb.Hsapiens.v86 (version 2.99.0). Then, the m^{6}A sites were mapped to the longest transcript of every corresponding gene. Within each transcript, the distances between individual m^{6}A sites were calculated. As a control, distances between random adenosines were determined. Here, sequence information of the longest transcripts and adenosine locations were obtained from a human gene annotation file (Homo_sapiens.GRCh38.cdna.all.fa), which was downloaded from Ensembl. Within each transcript, distances between several random adenosines, which were identical to the number of m^{6}A sites detected in the same transcript, were calculated. This procedure was repeated until an overall set of 1,000 random adenosine distances was obtained. To identify m^{6}A modification clusters, a 100 bp window was moved by steps of 10 bp through the transcripts. For each transcript, the coordinates of the m^{6}A sites were extracted, and for every window, the number of m^{6}A sites was determined. Individual windows were merged into m^{6}A clusters in case they shared at least one m^{6}A site. Cluster lengths were determined by calculating the distance between the first and the last m^{6}A site of the cluster.

6.2.14 Weighted global methylation level analysis

For the determination of the weighted global methylation level in the individual samples, m^{6}A methylation data from GLORI-seq and transcript expression data from bulk RNA-seq were integrated. The methylation level of each transcript was aggregated and then multiplied by the Transcripts Per Kilobase Million (TPM-)normalized expression level of the same transcript. These individual, weighted methylation levels were then summed up to compute the weighted global methylation level.

6.2.15 Differential methylation analysis

The R package methylSig (version 1.7.0) was used to identify differentially methylated m^6A sites from GLORI comparing control and UCB tissues. An absolute methylation level cutoff of 10% and a p-value cutoff of 0.05 were selected. Statistical significance was determined using beta binomial models.

6.2.16 Gene ontology analysis

Gene ontology (GO) analysis was conducted via ShinyGO (version 0.82) [193] using the Kyoto Encyclopedia of Genes and Genomes (KEGG) pathway database and a $p < 0.05$ cutoff.

6.2.17 Bulk RNA-seq and differential gene expression analysis

For bulk RNA-seq, total RNA from patient tissue and cell lines was extracted using TRIzol, DNase I-treated, and purified by the RNA Clean & Concentrator-5 kit (Zymo Research). For cell lines, three biological replicates were analyzed. STM2457 treatment was performed for 48 hours using 50 µM STM2457. Library preparation and sequencing were performed by the Next Generation Sequencing Core Facility of the German Cancer Research Center, Heidelberg. The samples were sequenced on a NovaSeq 6000 platform (Illumina) applying a 100 bp paired-end sequencing protocol. Reads were trimmed using Trim Galore (version 0.6.6) and mapped to the human reference genome (GRC38.p13 assembly) using HISAT2 (version 2.2.1). Aligned reads were counted by the featureCounts function (2.0.6), normalized, and differential gene analysis performed via DESeq2 (version 1.42.0) [195]. Only transcripts with read counts ≥ 10 in every sample were considered for downstream analyses. All analysis steps were performed in R (version 4.1.3) using RStudio (version 2022.02.1).

6.2.18 Analysis of APA events

For the *de novo* identification of APA sites, aligned reads from bulk RNA-seq experiments were analysed using the DaPars algorithm [164]. For the analyses, a coverage cutoff of 30, an FDR cutoff of 0.05, an absolute PDUI difference cutoff of 0.1, and an absolute fold change cutoff of 0.59 were selected.

6.2.19 DepMap databank analysis

Dependency probability scores for METTL3, POLR2F, and DNMT2 were extracted from the DepMap Public 22Q2 CRISPR gene dependency data set that can be downloaded from https://depmap.org/portal/download/all/. The dependency probability scores represent a measurement for the likelihood that a given gene is essential for cell proliferation and survival of a given cell line. If a given cell line has a dependency probability score > 0.5 for a given gene, the cell line is considered to be dependent on the gene for cell proliferation and survival.

6.2.20 *In silico* VIRMA expression analyses

VIRMA mRNA expression data were obtained from the UCSC database for the combined TCGA bladder urothelial carcinoma (BLCA) cohort and the GTEx project (https://xenabrowser.net/). Expression data were DESeq2-normalized and $\log_2$-transformed ($\log_2$(value + 1)). *In silico* VIRMA expression analysis was performed by Dr. Jinyun Xu (Division of Epigenetics, German Cancer Research Center, Heidelberg).

6.2.21 Association analysis of VIRMA genomic alterations and expression

VIRMA genetic alteration data and mRNA expression data were obtained from cBioPortal (https://www.cbioportal.org/) for the TCGA-BLCA cohort. mRNA expression values were preprocessed from RNA-seq by Expectation-Maximization (RSEM) data generated by the TCGA

RNASeqV2 pipeline (Illumina), which were batch-normalized and $\log_2$-transformed ($\log_2$(value + 1)). Different copy-number alterations were identified based on the Genomic Identification of Significant Targets in Cancer (GISTIC) method. Pearson correlation analysis was performed to assess the association between VIRMA $\log_2$ copy-number values and mRNA expression levels. This analysis was performed by Dr. Jinyun Xu (Division of Epigenetics, German Cancer Research Center, Heidelberg).

6.2.22 Kaplan-Meier survival analysis

Kaplan-Meier overall survival analysis was performed using the lifelines Python package. Patients were stratified into VIRMA-high and VIRMA-low mRNA expression groups using maximally selected log-rank statistics. The Kaplan-Meier survival analysis was performed by Dr. Jinyun Xu (Division of Epigenetics, German Cancer Research Center, Heidelberg).

6.2.23 Western blotting

Target cells were lysed in Western blot lysis buffer (Tab. 9) and protein lysates quantified by Bradford assays. Proteins were separated by sodium dodecyl sulfate-polyacrylamide gel electrophoresis (SDS-PAGE) and transferred to nitrocellulose membranes using a Trans-Blot Turbo Transfer System (Bio-Rad). Successful transfer was verified by Ponceau staining. Membranes were blocked in 0.1% PBST containing 5% milk powder for 1 hour at RT. Primary antibody incubation was performed overnight at 4 °C using the antibodies listed in Tab. 10. Membranes were washed three times using 0.1% PBST. Secondary antibody incubation occurred for 1 hour at RT using the antibodies listed in Tab. 10. Primary and secondary antibodies were diluted in 0.1% PBST containing 5% milk powder. Again, membranes were washed three times using 0.1% PBST. Finally, membranes were imaged using the Immobilon Western HRP Substrate (Merck), and signals detected using an M6 ECL Chemostar fluorescence imaging system (Intas). Images were analyzed by ImageJ software.

6.2.24 m^{6}A detection in urine RNA by GLORI 2.0-PCR

50 mL of urine was collected, and total RNA was isolated using the ZR Urine RNA Isolation Kit (Zymo Research). Urine total RNA was then DNase I-treated and purified by the RNA Clean & Concentrator-5 kit (Zymo Research). The concentrations were determined by TapeStation (Agilent Technologies).

Principally, the GLORI 2.0-related steps were performed as described in Sun *et al.*, 2025 [189].

For RNA protection, 50 ng of DNase I-digested total RNA from the T24 cell line (control) and from a urine sample were added to the GLORI 2.0 deamination buffer (Tab. 9) and incubated for 10 min at 50 °C in a thermal cycler. After deamination, RNA was purified by ethanol precipitation overnight at - 80 °C. Pelleted RNA was washed twice using 75% ethanol and air-dried for 5 min at RT. Then, the RNA pellet was resuspended in 50 µL of deprotection buffer (Tab. 9) and incubated for 10 min at 95 °C in a thermal cycler. Deprotected RNA was purified by ethanol precipitation for at least 30 min at - 80 °C. Pelleted RNA was washed twice using 75% ethanol and air-dried for 5 min at RT. The RNA pellet was then resuspended in 11 µL of water and reverse-transcribed into cDNA by the SuperScript III First-Strand Synthesis System (Thermo Fisher Scientific). During cDNA synthesis, 1 µL of a 10 µM reverse primer designated as GLORI2.0_RT_R was used (Tab. 14). Then, cDNAs were further amplified via two consecutive PCRs using the Phanta Max Master Mix (Vazyme). In the first PCR, target site regions were amplified. In the second PCR, primers were used to attach a sequence complementary to a sequencing primer utilized for subsequent Sanger Sequencing analysis. For the detection of a control site and a known m^{6}A site in the 28S rRNA, primers designated as 28S_rRNA_Ctrl_F/R and 28S_rRNA_F/R were used. For the detection of known m^{6}A sites in the CAND1, EIF2A, and ILF3 transcripts, primers designated as CAND1_F/R, EIF2A_F/R, and ILF3_F/R were used. For the second PCR, primers designated as Illumina_Primer_F and Illumina_Primer_Index were used for all amplicons generated in the first PCR reactions. All PCR reactions were separated by agarose gel electrophoresis, and the target bands were extracted using the QIAquick Gel Extraction kit (Qiagen). Amplicons were sent for Sanger Sequencing (Eurofins) and sequenced using a primer designated as GLORI_Sanger. All primers used are listed in Tab. 14.

6.2.25 Immunofluorescence staining

Target cells were seeded on cover slips and fixed for 10 minutes at RT using 4% PFA prepared in PBS. Then, cells were permeabilized for 15 minutes at RT in 0.3% Triton-X-100 prepared in PBS. Fixed and permeabilized cells were washed three times using PBS and blocked using 10% FBS prepared in 0.1% PBST for 1 hour at RT in a humid chamber. Primary antibody incubation was performed overnight at 4 °C in a humid chamber using the antibodies listed in Tab. 10. Cover slips were then washed three times using 0.1% PBST. Secondary antibody incubation occurred for 1 hour at RT in a humid chamber using the antibodies listed in Tab. 10. Primary and secondary antibodies were diluted in 10% FBS prepared in 0.1% PBST. Again, membranes were washed three times using 0.1% PBST. Cover slips were mounted onto microscopy slides using ProLong Gold Antifade Mountant with DNA Stain DAPI (Thermo Fisher Scientific) and dried in the dark for 24 hours. Images were acquired on an Axio microscope (Zeiss).

6.2.26 Cloning of GFP-LSM14A for generating cell lines forming labeled P-bodies

From UM-UC-3 cDNA, LSM14A was amplified via PCR using the Q5 High-Fidelity DNA Polymerase (New England Biolabs). In the PCR reactions, primers with EcoRI and BamHI restriction site overhangs (designated as LSM14A_Eco_F and LSM14A_Bam_R in Tab. 14) were used to attach the restriction sites to the synthesized amplicon, thereby making the amplicon suitable for restriction enzyme-based cloning in the next step. PCR reactions were separated by agarose gel electrophoresis, and the target bands were extracted using the QIAquick Gel Extraction kit (Qiagen).

For replacing the MNX1 cassette of the pLVX-GFP-HA-FLAG vector (provided by Dr. Simge Kelekci (Cancer Epigenomics division, German Cancer Research Center, Heidelberg), Tab. 15 and section 7.4.1), pLVX-GFP-HA-FLAG and the PCR-amplified LSM14A amplicon were cut using EcoRI and BamHI restriction enzymes (Thermo Fisher Scientific). Digestions were separated by agarose gel electrophoresis, and the target bands were extracted using the QIAquick Gel Extraction kit (Qiagen). The cut LSM14A amplicon was ligated into the cut pLVX-GFP-HA-FLAG vector backbone using the T4 DNA Ligase (New England Biolabs), yielding a closed pLVX-GFP-HA-FLAG-LSM14A vector. Ligations were transformed into One Shot Stbl3 Chemically Competent *E. coli* cells (Thermo Fisher Scientific) by heat-shock. Transformed clones were selected using LB agar plates supplemented with ampicillin. Plasmid constructs from single clones were purified using Mini, Midi, and Maxi Prep Kits (Qiagen). Cloning was verified by analytical restriction digestions and Sanger Sequencing (Eurofins).

For lentivirus production, HEK293T cells were transfected with the recombinant plasmid construct using Lipofectamine 2000 (Thermo Fisher Scientific). Transfected HEK293T cells were cultured for 48 hours. Virus-containing medium supernatants from transfected HEK293T cells were filtered using cellulose acetate filters (0.45 µm, Sartorius) and added to target cells for transduction. Transduction was performed for 48 hours. Cells that were transduced with the pLVX-GFP-HA-FLAG-LSM14A construct were selected for one week using puromycin (Thermo Fisher Scientific).

6.2.27 Cellular fractionation and affinity purification of P-bodies (CFAPP)

GFP-LSM14A expressing cells were grown in 15 cm cell culture dishes. Cells were washed twice using PBS and detached by a cell scraper. Cells were spun down, resuspended in 1 mL fractionation buffer (Tab. 9), and incubated for 8 minutes on ice to promote cell lysis. For pelleting the nuclei, lysates were spun for 5 minutes at 1,300 g in a cooled centrifuge. The supernatant (cytoplasmic fraction) was transferred to a new tube, and the centrifugation step was repeated. To obtain an insoluble, organelle-enriched fraction, the cytoplasmic fraction was spun for 8 minutes at 16,000 g in a cooled centrifuge. The supernatant (soluble cytosolic fraction) was discarded. The pelleted insoluble, organelle-enriched fraction was washed twice using fractionation buffer. The final pellet was resuspended in 400 µL fractionation buffer. To prepare the samples for subsequent anti-GFP bead-based affinity purification, 100 µL of 5x dilution buffer (from GFP-Trap Magnetic Particles M-270 Kit, Proteintech) was added, yielding a total volume of 500 µL. The resuspended insoluble, organelle-enriched fraction was either subjected to Fluorescence-activated particle sorting (FAPS) [196] (sorting was performed by Dr.

Monika Langlotz (Flow Cytometry and FACS Core Facility, Center for Molecular Biology Heidelberg)) or subjected to affinity purification using the GFP-Trap Magnetic Particles M-270 Kit (Proteintech). In brief, 25 µL of beads were washed three times using washing buffer (Tab. 9). For sample binding, 500 µL of input sample was added to the beads and incubated for 1 hour at 4 °C while rotating. Beads were washed three times using washing buffer. Washed beads were then resuspended in Laemmli buffer for Western blotting analysis or resuspended in TRIzol for RNA isolation. For qRT-PCR analysis, RNA was DNase I-treated and purified using the RNA Clean & Concentrator-5 kit (Zymo Research). 50 ng of RNA were then reverse-transcribed into cDNA by the SuperScript III First-Strand Synthesis System (Thermo Fisher Scientific) using random hexamers for priming. qRT-PCRs were performed on a LightCycler 480 thermocycler (Roche) using the Mesa Green qPCR MasterMix Plus for SYBR (Eurogentec) and primers targeting P-body-enriched or P-body-depleted transcripts taken from Hubstenberger *et al.*, 2017 [196] (Tab. 14). Ct values were measured in triplicate and analyzed using the GraphPad Prism software. Note that a reference gene could not be used for normalization, as I did not analyze total RNA or mRNA, but potentially P-body-associated RNA for which no reference is known. My data rely on the assumption that reverse transcription reactions were performed with the same amount of input RNA and are therefore comparable.

6.2.28 Data availability

GLORI and bulk RNA-seq data generated in this study have been deposited in the GEO database under the accession numbers GSE281749 and GSE281750.

6.2.29 Statistics

Statistical analyses were conducted in GraphPad Prism software and R. Detailed statistics for all experiments are provided in the figure legends. A p-value < 0.05 was considered significant in all analyses.

Unless otherwise stated, cell culture experiments were performed in biological and technical triplicates, and data are reported as mean ± SD. Cell proliferation assays were analyzed by two-way analysis of variance. Colony-formation assays, apoptosis assays, and LC-MS/MS measurements were compared using t-tests for pooled cell populations or one-way analysis of variance for cell clones. DepMap data were analyzed with the Mann-Whitney-U test. Western blots of STM2457-treated UCB cell lines were analyzed by one-way analysis of variance. VIRMA expression as well as m^6A mRNA methylation in patient samples were assessed with the Mann-Whitney-U test. Aggregated and weighted global m^6A methylation levels were analyzed using t-tests. Kaplan-Meier curves were compared by the log-rank test. The assessment of the statistical significance for RNA-seq, GLORI-seq, and differential m^6A methylation analyses is described in the respective methods sections.

7 Appendix

7.1 Supplementary Tables

Suppl. Tab. 1: Read counts and mapping efficiencies in GLORI samples.

Sample	Number of input reads	Mapping efficiency [%]
HEK293T I	300922280	52.18
HEK293T II	222200609	50.84
HEK293T III	111741441	51.8
Paratumoral I	210134684	50.05
Paratumoral II	114142354	50.9
Paratumoral III	194060112	50.95
Paratumoral IV	202742613	50.41
Paratumoral V	252247624	48.63
Paratumoral VI	163084610	48.56
Paratumoral VII	210997476	49.52
Paratumoral VIII	149997503	50.07
Paratumoral IX	125859823	49.83
RT4 shCtrl I	307603811	50.85
RT4 shCtrl II	345624521	51.16
RT4 shCtrl III	301014538	50.67
RT4 VIRMA KD I	273857674	47
RT4 VIRMA KD II	192310642	52.12
RT4 VIRMA KD III	169403065	50.71
T24 DMSO I	260940137	46.67
T24 DMSO II	309220350	45.85
T24 DMSO III	266191689	46.28
T24 METTL3 KO I	153120482	47.37
T24 METTL3 KO II	247227846	47.8
T24 METTL3 KO III	168304579	47.58
T24 Scr I	160077497	47.01
T24 Scr II	86744399	45.66

T24 Scr III	223175415	47.06
T24 STM2457 I	233509215	46.2
T24 STM2457 II	137268107	46.94
T24 STM2457 III	180422209	46.18
UCB I	224895670	49.42
UCB II	230506398	49.71
UCB III	207737049	50.33
UCB IV	269625826	51.4
UCB V	301150528	50.86
UCB VI	292801112	51.33
UCB VII	546199419	46.21
UCB VIII	104346379	48.29
UCB IX	179928871	47.86
UM-UC-3 shCtrl I	269840589	50.25
UM-UC-3 shCtrl II	204550065	51.12
UM-UC-3 shCtrl III	193087828	51.22
UM-UC-3 VIRMA KD I	210084132	51.20
UM-UC-3 VIRMA KD II	144803795	51.27
UM-UC-3 VIRMA KD III	127291683	51.20

Suppl. Tab. 2: Conversion rates obtained in GLORI samples.

Sample	Loci	Median conversion [%]
HEK293T I	Spike-in	99
	All	100
HEK293T II	Spike-in	99
	All	100
HEK293T III	Spike-in	99
	All	100
Paratumoral I	Spike-in	99.5
	All	100
Paratumoral II	Spike-in	100

	All	98.9
Paratumoral III	Spike-in	99.5
	All	98.9
Paratumoral IV	Spike-in	99
	All	100
Paratumoral V	Spike-in	99
	All	100
Paratumoral VI	Spike-in	99
	All	100
Paratumoral VII	Spike-in	99
	All	100
Paratumoral VIII	Spike-in	99
	All	100
Paratumoral IX	Spike-in	99
	All	100
RT4 shCtrl I	Spike-in	98.2
	All	99.3
RT4 shCtrl II	Spike-in	98.3
	All	99.2
RT4 shCtrl III	Spike-in	98.4
	All	99.3
RT4 VIRMA KD I	Spike-in	98.4
	All	99.4
RT4 VIRMA KD II	Spike-in	98.4
	All	99.2
RT4 VIRMA KD III	Spike-in	98.4
	All	99.6
T24 DMSO I	Spike-in	98.8
	All	100
T24 DMSO II	Spike-in	98.8
	All	100
T24 DMSO III	Spike-in	98.9

	All	100
T24 METTL3 KO I	Spike-in	98.8
	All	100
T24 METTL3 KO II	Spike-in	98.9
	All	100
T24 METTL3 KO III	Spike-in	98.8
	All	100
T24 Scr I	Spike-in	98.9
	All	100
T24 Scr II	Spike-in	98.9
	All	100
T24 Scr III	Spike-in	98.9
	All	100
T24 STM2457 I	Spike-in	98.9
	All	100
T24 STM2457 II	Spike-in	98.8
	All	100
T24 STM2457 III	Spike-in	99
	All	100
UCB I	Spike-in	99.5
	All	98.9
UCB II	Spike-in	99.5
	All	98.9
UCB III	Spike-in	99.5
	All	98.9
UCB IV	Spike-in	99.5
	All	98.9
UCB V	Spike-in	99.5
	All	99
UCB VI	Spike-in	99.4
	All	98.9
UCB VII	Spike-in	99

	All	100
UCB VIII	Spike-in	99
	All	100
UCB IX	Spike-in	9968
	All	100
UM-UC-3 shCtrl I	Spike-in	98.4
	All	99.2
UM-UC-3 shCtrl II	Spike-in	98.2
	All	99
UM-UC-3 shCtrl III	Spike-in	98.2
	All	98.8
UM-UC-3 VIRMA KD I	Spike-in	98.4
	All	99
UM-UC-3 VIRMA KD II	Spike-in	98.3
	All	99
UM-UC-3 VIRMA KD III	Spike-in	98.5
	All	99.2

Suppl. Tab. 3: Distribution of GLORI-seq reads across transcriptomic features in T24 cells. Feature quantification was performed using featureCounts.

Feature	Average read count	Percentage [%]
protein-coding	119,588,441	85.4
pseudogene (all types)	17,502,095.3	12.5
long non-coding RNA (lncRNA)	2,791,594.3	2.0
(small) non-coding RNA	77,803	< 0.1
TEC (to be experimentally confirmed)	66,698.7	< 0.1
ribosomal RNA (rRNA)	5,804.3	< 0.01
Immunoglobulin/T-cell receptor genes	3,510.7	< 0.01
artifact / low-confidence	2,650	< 0.01
mitochondrial RNA (mtRNA)	0	0

Suppl. Tab. 4: Within-group variability of detected DRAC(H) sites in patient samples.

Group	Number of DRAC(H) sites	Mean SD [%]	P90 SD [%]	Mean range [%]
Cancer	353,348	1.21	5.92	3.53
Control	353,348	1.15	5.52	3.32

7.2 Supplementary Figures

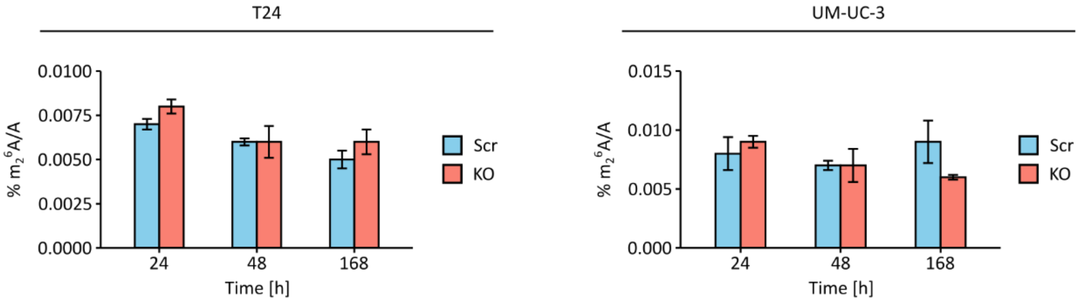

Suppl. Fig. 1: Assessment of rRNA contaminants in mRNA preparations. Related to Fig. 6. m$_2^6$A measurements from LC-MS/MS time course analyses of mRNA preparations from TLCV2 Scr and METTL3 KO pools. Technical triplicates were analyzed from two biological replicates.

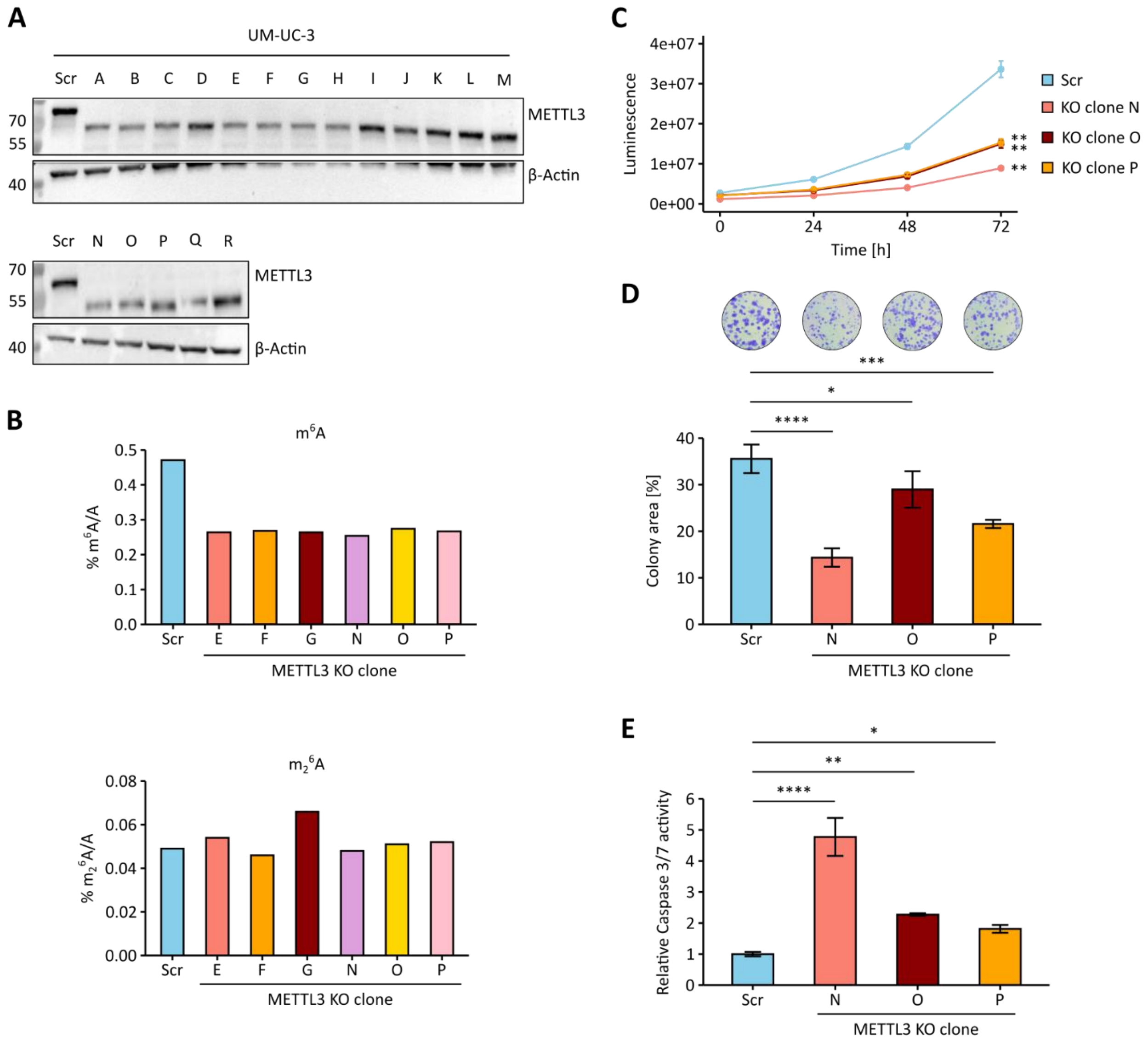

Suppl. Fig. 2: METTL3 activity is essential for the viability of UM-UC-3 cells. Related to Fig. 7. **A)** Western blot analysis of UM-UC-3 METTL3 KO clones. **B)** LC-MS/MS quantification of m^{6}A and m$_2{}^6$A levels in mRNA from selected UM-UC-3 METTL3 KO clones. One biological replicate was analyzed per clone. LC-MS/MS analyses were performed in collaboration with Dr. Martina Krämer (Helm lab, Institute of Pharmaceutical and Biomedical Sciences, Johannes Gutenberg University, Mainz). **C)** Cell proliferation assays of UM-UC-3 METTL3 KO clones and Scr cells. $**p < 0.01$, two-way analysis of variance. **D)** Colony formation assays of UM-UC-3 METTL3 KO clones and Scr cells. $*p < 0.05$, $***p < 0.001$, $****p < 0.0001$, one-way analysis of variance. **E)** Caspase 3/7 activity measurements in UM-UC-3 METTL3 KO clones and Scr cells. $*p < 0.05$, $**p < 0.01$, $****p < 0.0001$, one-way analysis of variance. pLentiCRISPR v2 Scr and METTL3 KO clones were analyzed.

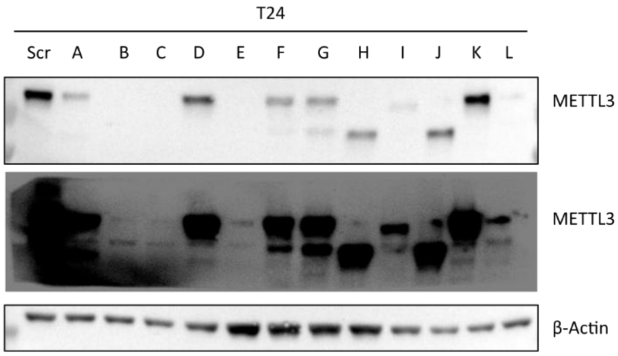

Suppl. Fig. 3: Quality control of T24 METTL3 KO screening. Related to Fig. 7. Western blot analysis of T24 METTL3 KO clones with an enhanced-contrast version of the membrane shown in Fig. 7A. pLentiCRISPR v2 Scr and METTL3 KO clones were analyzed.

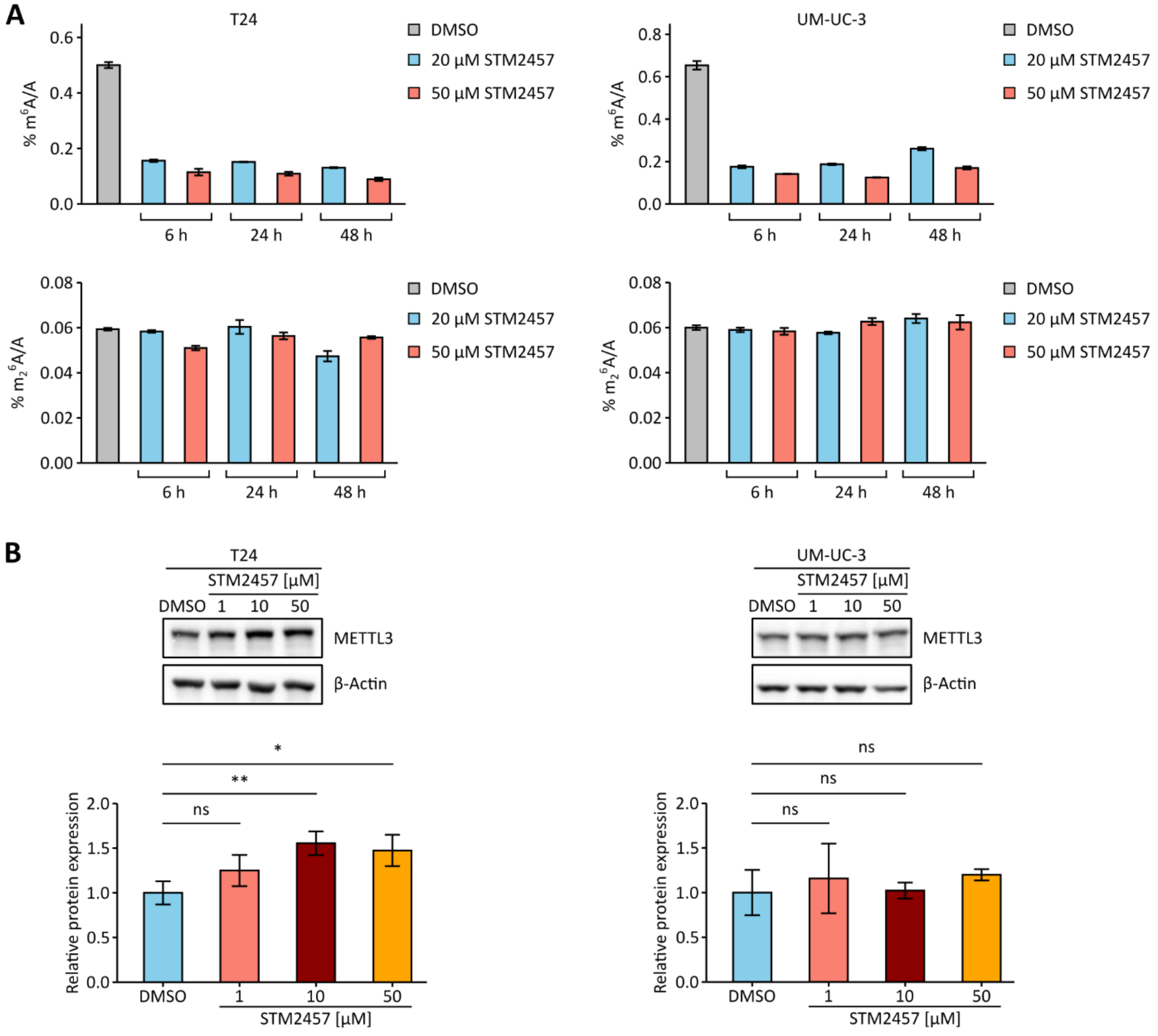

Suppl. Fig. 4: Effect of STM2457 treatment on global m^{6}A levels and METTL3 expression. Related to Fig. 8. **A)** LC-MS/MS analysis of m^{6}A in mRNA from T24 and UM-UC-3 cells treated with 20 µM or 50 µM STM2457, or with DMSO, for the indicated time points. m$_2^6$A measurements are included to assess rRNA contamination in the mRNA preparations. Technical triplicates were performed from one biological replicate. LC-MS/MS analyses were performed in collaboration with Dr. Martina Krämer (Helm lab, Institute of Pharmaceutical and Biomedical Sciences, Johannes Gutenberg University, Mainz). **B)** METTL3 protein levels in cells treated with 1 µM, 10 µM, and 50 µM STM2457, or with DMSO, for 48 hours. ns = not significant, *$p < 0.05$, **$p < 0.01$, one-way analysis of variance.

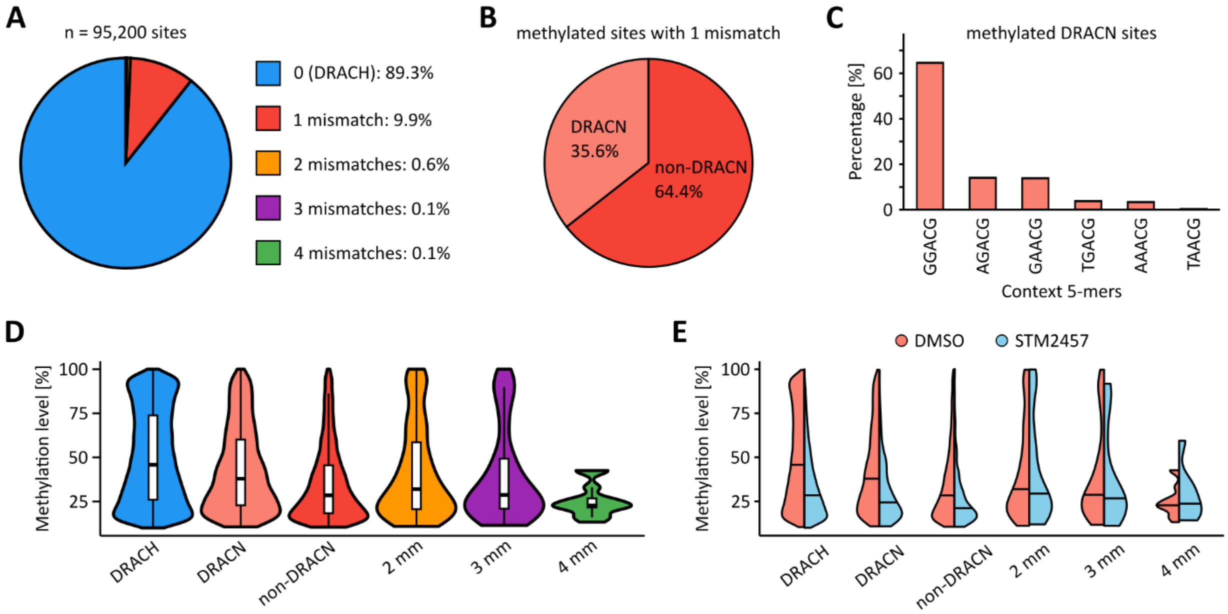

Suppl. Fig. 5: m^{6}A sites detected in DRAC(H) motifs are the most robust GLORI-seq signals. Related to Fig. 17. **A)** Distribution of detected m^{6}A sites across sequence motifs containing the indicated number of mismatches relative to the canonical DRACH consensus. **B)** Distribution of m^{6}A sites within 5-mer motifs containing a single mismatch relative to DRACH. In DRACN motifs, the first four bases are conform to DRACH. In non-DRACN motifs, the mismatch occurs within the first four positions. **C)** Frequency of detected DRACN motifs. **D)** Distribution of methylation levels across the different motif categories. **E)** Methylation level distributions of m^{6}A sites detected in the different motif categories in the T24 cell line treated with STM2457 or DMSO. (mm = mismatches compared to DRACH consensus).

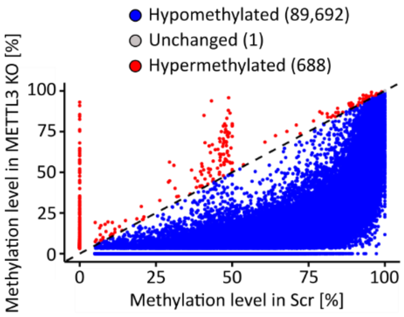

Suppl. Fig. 6: GLORI detects loss of m^{6}A methylation in T24 METTL3 KO cells. Related to Fig. 17. Scatter plot comparing mean m^{6}A levels of methylated DRAC(H) sites shared between T24 METTL3 KO and Scr cells.

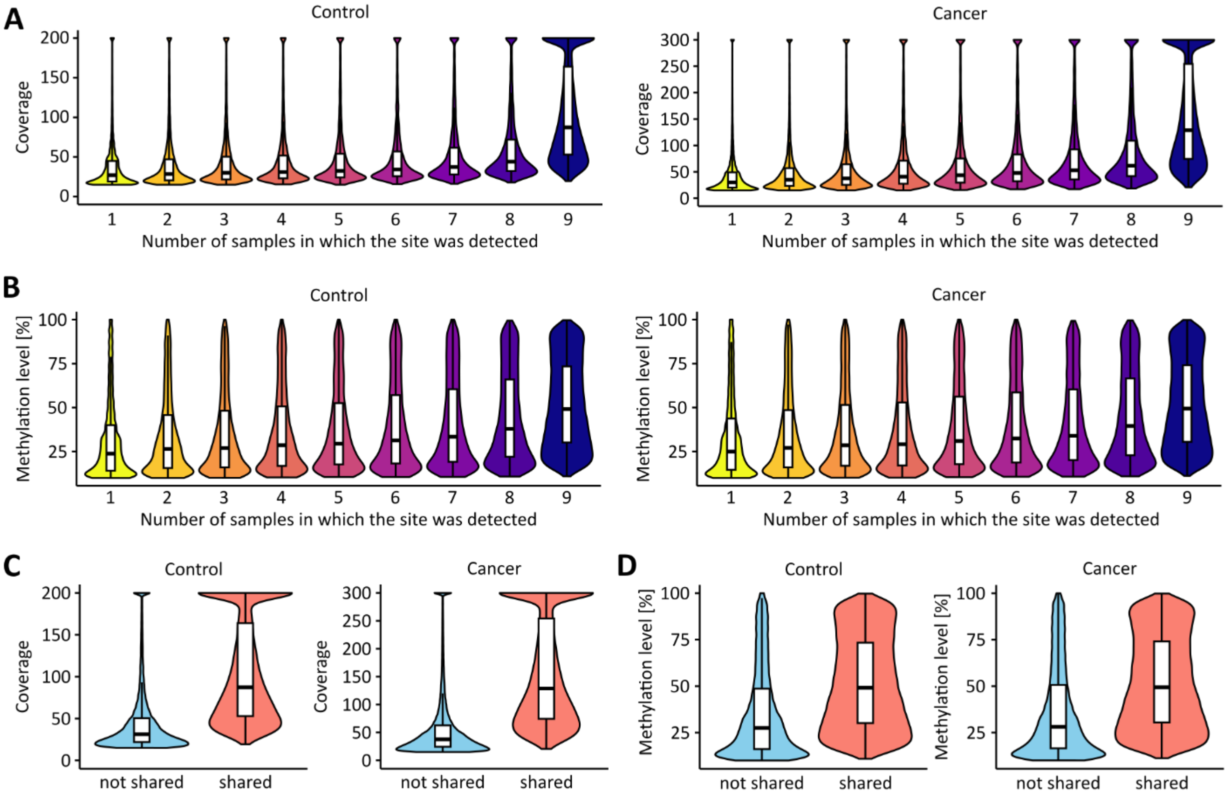

Suppl. Fig. 7: Shared m^{6}A sites show high coverage and methylation levels. Related to Fig. 18. **A)** Distributions of sequencing coverage for m^{6}A sites detected across different numbers of samples within each tissue group. **B)** Distributions of methylation levels for m^{6}A sites detected across different numbers of samples within each tissue group. **C)** Comparison of the sequencing coverage distributions of m^{6}A sites detected in all nine samples (shared) and those detected in 1-8 samples (not shared). **D)** Comparison of the methylation level distributions of m^{6}A sites detected in all nine samples (shared) and those detected in 1-8 samples (not shared).

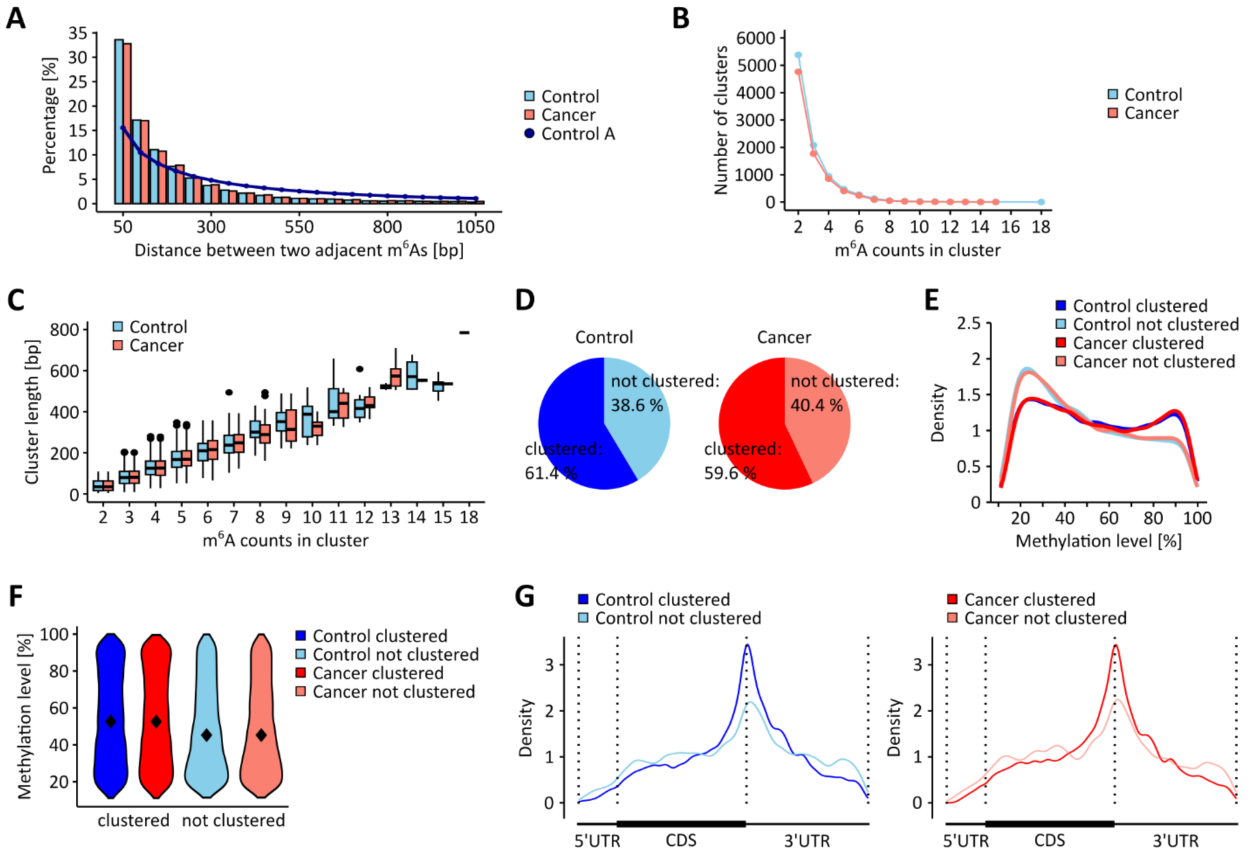

Suppl. Fig. 8: m^{6}A sites cluster similarly in UCB and control tissues. Related to Fig. 19. **A)** Distribution of distances between neighboring m^{6}A sites in UCB and control tissues. **B**) Number of m^{6}A sites per cluster in both tissue types. **C)** Relationship between cluster length and the number of contained m^{6}A sites. **D)** Proportion of m^{6}A sites assigned to clusters versus non-clustered sites in UCB and control tissues. **E)** and **F)** Methylation level distributions of clustered and non-clustered m^{6}A sites in each tissue type. **G)** Metagene analyses illustrating proportional enrichment of clustered and non-clustered m^{6}A sites in UCB and control samples.

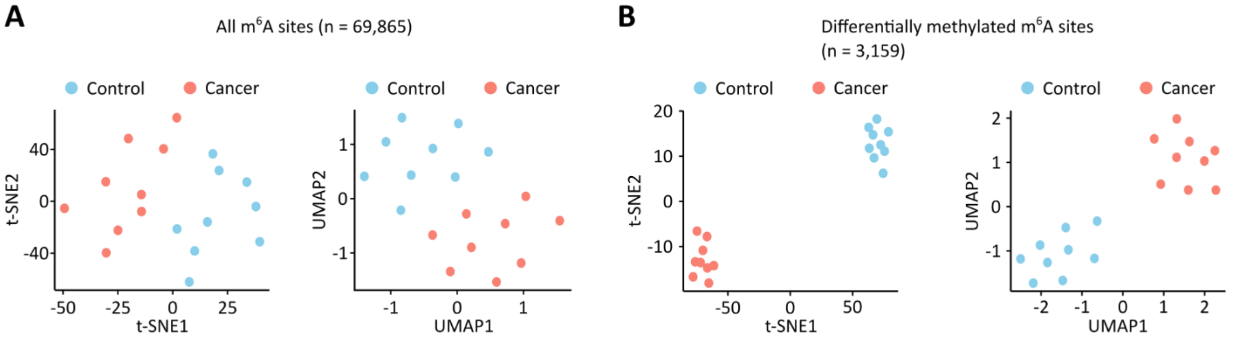

Suppl. Fig. 9: t-SNE and UMAP separate UCB and control samples by m^{6}A profiles. Related to Fig. 19 and Fig. 20. t-SNE and UMAP analyses performed using all detected m^{6}A sites **A)**, and only the differentially methylated sites **B)**.

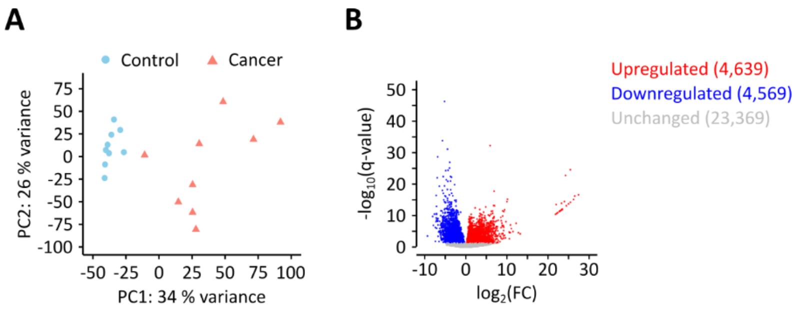

Suppl. Fig. 10: RNA-seq reveals distinct patient transcriptional profiles. Related to Fig. 21. **A)** PCA of UCB and control samples based on gene expression patterns. **B)** Overview of differentially expressed genes identified between UCB and control samples. q-value < 0.05.

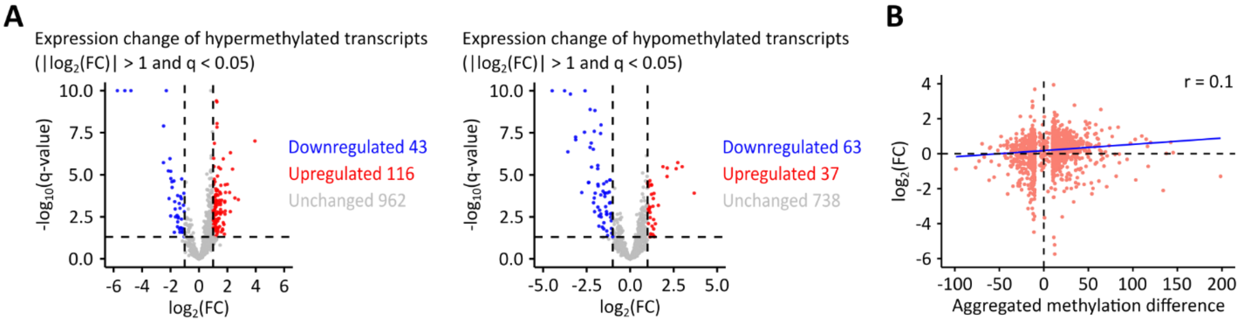

Suppl. Fig. 11: Expression changes of differentially methylated transcripts. Related to Fig. 22. **A)** Expression changes of transcripts containing hypermethylated or hypomethylated m^6A sites in UCB compared to control tissues. **B)** Correlation analysis comparing aggregated methylation differences of transcripts with differentially methylated m^6A sites to their corresponding expression changes. Correlation coefficient r = 0.1, $p = 7.9 \times 10^{-6}$.

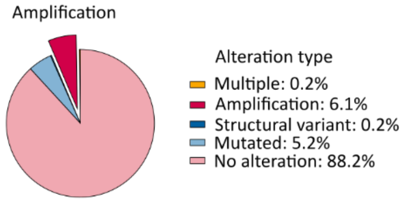

Suppl. Fig. 12: Genomic alterations of the VIRMA gene in UCB. Related to Fig. 22. Overview of VIRMA genomic alterations in the TCGA-BLCA cohort.

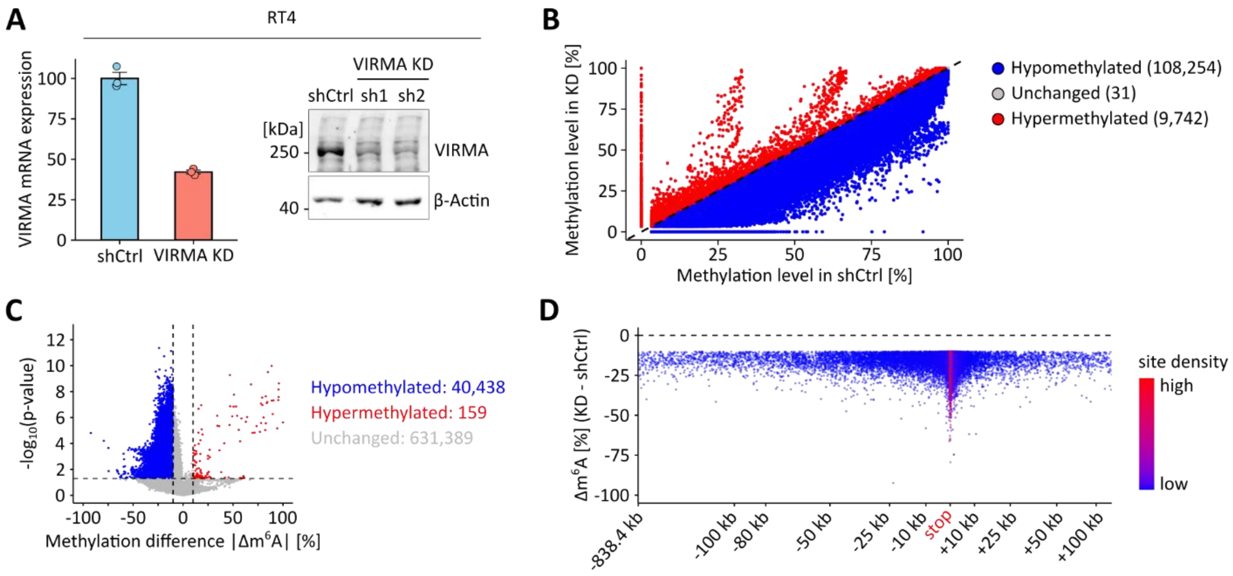

Suppl. Fig. 13: VIRMA depletion leads to a global loss of m^{6}A methylation in RT4 cells. Related to Fig. 22. **A)** RNA-seq and Western blot analyses of VIRMA expression levels in RT4 VIRMA KD and shCtrl cells. **B)** Scatter plot comparing mean m^{6}A levels of methylated DRAC(H) sites shared between RT4 VIRMA KD and shCtrl cell lines. **C)** Overview of differentially methylated m^{6}A sites in VIRMA-depleted RT4 cells, based on |Δmethylation| ≥ 10% and $p < 0.05$ thresholds. Unmethylated DRAC(H) sites are included in this analysis. **D)** Δm^{6}A levels (RT4 VIRMA KD - shCtrl) for differentially hypomethylated m^{6}A sites were plotted across transcript regions surrounding the stop codon.

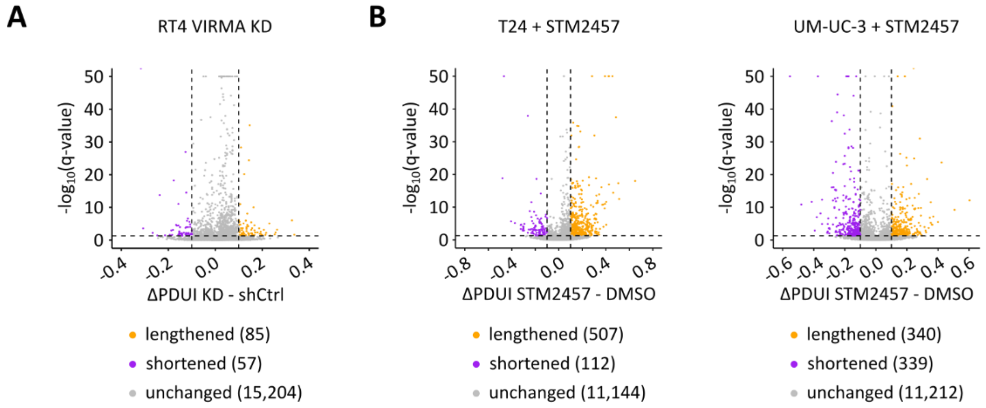

Suppl. Fig. 14: APA analysis in writer complex-disturbed UCB cells. Related to Fig. 24. **A)** DaPars-based analysis of APA showing ΔPDUI for RT4 VIRMA-depleted cells compared to shCtrl cells. **B)** DaPars-based APA analysis showing ΔPDUI for STM2457-treated T24 and UM-UC-3 cells compared to DMSO-treated cells.

7.3 Expanded View Data

7.3.1 GLORI 2.0 detects m^{6}A in total RNA from urine

Early detection biomarkers for UCB are currently lacking, which limits patient diagnosis and treatment [6]. Since uroepithelial and UCB cells are shed into the urine, urine represents a non-invasive and clinically accessible source of material for diagnostic and prognostic analyses. The presented GLORI-seq analysis of UCB and paratumoral control tissues revealed systematic alterations in the m^{6}A landscapes between both groups, highlighting the biomarker potential of m^{6}A profiling. Based on these findings, I investigated the feasibility of developing a PCR-based assay for the detection of specific, differentially methylated m^{6}A sites in total RNA isolated from urine-derived cells.

For this purpose, total RNA was isolated from cells present in freshly voided or morning urine samples (50 mL each). RNA quality was assessed by TapeStation and revealed RNA integrity numbers of approximately 4.8 and 4.5, which reflect moderate RNA degradation (Expanded View Fig. 1A). Total RNA yields ranged from 200 - 250 ng per sample. Although this amount is insufficient for the original GLORI protocol, which requires roughly 200 ng of fragmented mRNA [27], it is adequate for GLORI 2.0. In addition, the chemical treatment used in GLORI 2.0 is considerably milder, which allows for downstream PCR-based assays for m^{6}A detection [189]. To implement and validate the GLORI 2.0-based deamination reaction, I first deaminated a synthetic RNA oligonucleotide that was also previously used to establish the original GLORI protocol. Complete conversion of the adenosines was confirmed by GLORI 2.0-PCR and Sanger sequencing (Expanded View Fig. 1B). Subsequently, 50 ng of total RNA isolated from the freshly voided urine sample and an equal amount of total RNA from T24 cells (as a control) were subjected to GLORI 2.0 treatment. In further GLORI 2.0-PCR assays, both a non-m^{6}A control site and a known m^{6}A site in 28S rRNA could be detected in both samples, as confirmed by Sanger sequencing (Expanded View Fig. 1C) [189]. Sites in the 28S rRNA were selected since rRNA is the most abundant RNA species in total RNA. These results demonstrate that GLORI 2.0-PCR enables the detection of m^{6}A in total RNA derived from urine.

In the T24 control RNA sample, additional known m^{6}A sites were detected in abundant mRNA transcripts, including CAND1, EIF2A, and ILF3 (Expanded View Fig. 1D) [189]. Sites from abundant mRNAs were selected because mRNA constitutes only 5% of total RNA. Whether these sites, and ultimately those sites found to be differentially methylated in my comparative GLORI-seq analysis, can also be detected in total RNA from urine remains to be determined. However, the preliminary findings suggest that m^{6}A detection in urinary RNA could be developed into a biomarker approach for UCB.

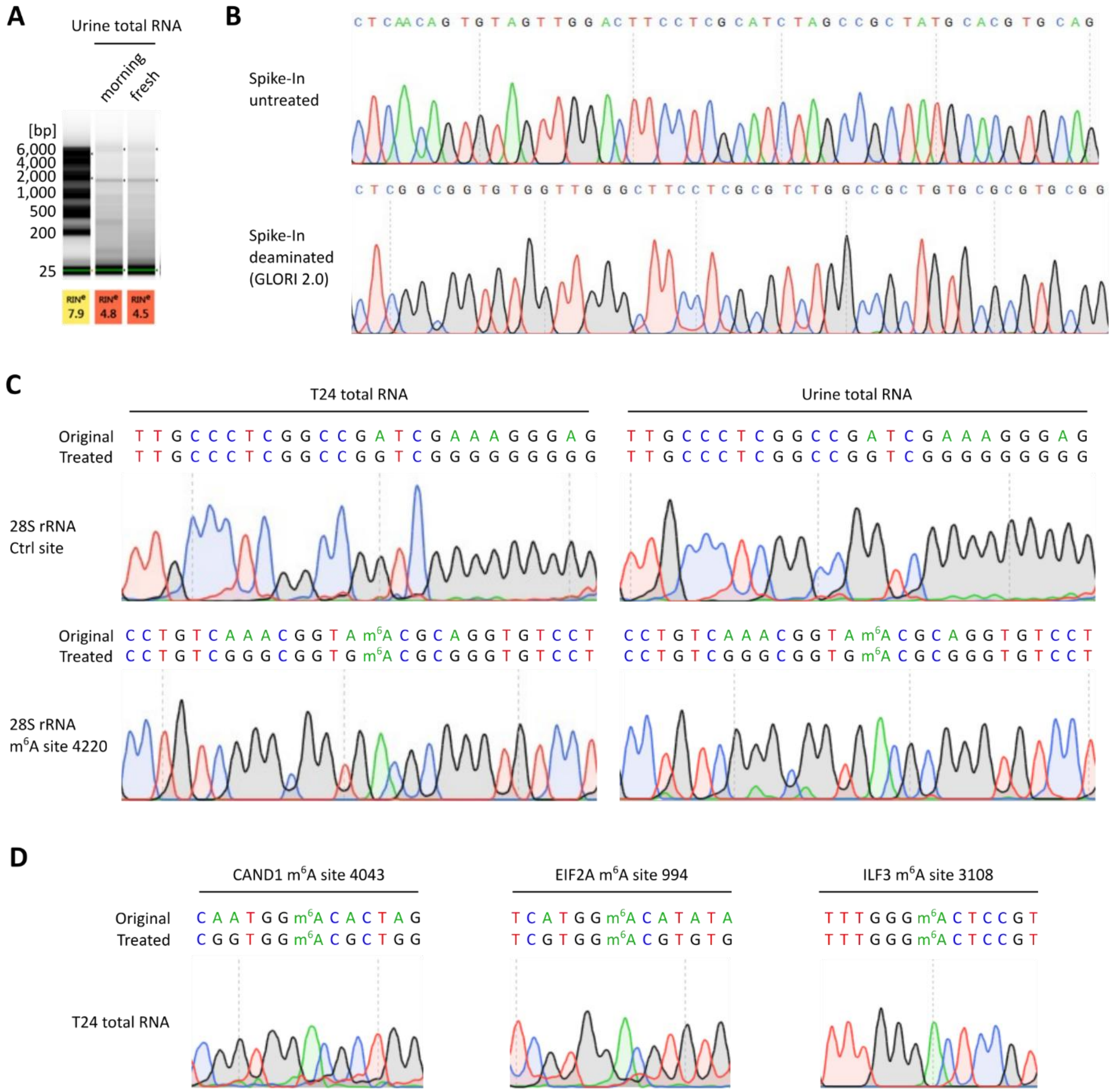

Expanded View Fig. 1: Detection of m^{6}A in total RNA from urine using GLORI 2.0. A) TapeStation analysis of total RNA isolated from cells present in urine. **B)** GLORI 2.0-based deamination of a synthetic RNA oligonucleotide. **C)** GLORI 2.0-PCR assays targeting a control site and an m^{6}A site in 28S rRNA. **D)** GLORI 2.0-PCR assays targeting selected m^{6}A sites in abundant mRNAs in total RNA from T24 cells.

7.3.2 Workflow establishment for the enrichment of P-body-associated transcripts

Recently, m^{6}A was shown to enhance the phase separation potential of its target transcripts. Transcripts with multiple modification sites recruit and juxtapose multiple reader proteins, which promoted the formation of mRNA-reader condensates that were shown to further separate into cytoplasmic condensates like stress granules and P-bodies [56,70]. For future investigation of the influence of m^{6}A-dependent phase separation and P-body-mediated transcript regulation in UCB, I aimed for the establishment of a protocol that allowed for the isolation or enrichment of P-body-associated transcripts. This workflow was termed cellular fractionation and affinity purification of P-bodies (CFAPP).

Initially, I pursued a protocol that generated cells forming fluorescent P-bodies, which were then subjected to fluorescence-activated particle sorting (FAPS) for the isolation of P-body-associated transcripts [196]. I transduced T24 and UM-UC-3 cells with a GFP-tagged LSM14A fusion protein, with LSM14A being a known P-body marker protein. GFP-LSM14A expressing cells were found to form fluorescent P-bodies in immunofluorescence staining experiments when co-stained with further P-body marker proteins DDX6 and 4E-T (Expanded View Fig. 2A and Expanded View Fig. 3A). Next, I implemented a protocol for the enrichment of the insoluble, cytoplasmic, and organelle-enriched fraction of cells using subsequent differential centrifugation steps that depleted nuclei and the soluble, cytoplasmic fraction of cells (Expanded View Fig. 2B). The resulting insoluble, cytoplasmic cell fraction was then subjected to FAPS. In FAPS, which was performed by Dr. Monika Langlotz (Flow Cytometry and FACS Core Facility, Center for Molecular Biology Heidelberg), two GFP-positive populations that differed in size were detected (Expanded View Fig. 3B and C). However, when I tried to pellet the sorted particles for RNA isolation, no RNA was obtained (not shown). Thus, I pursued another strategy for yielding P-body-associated transcripts by using affinity purification-based enrichment of GFP-tagged P-bodies with anti-GFP beads. The enrichment of P-bodies via CFAPP was analyzed via Western blotting, which confirmed the enrichment of the P-body marker proteins EDC4, 4E-T, DCP1A, and DDX6 (Expanded View Fig. 2C). In qRT-PCR analyses, known P-body-enriched and P-body-depleted transcripts [196] were targeted to validate the enrichment of P-bodies during CFAPP. The results confirmed an enrichment of transcripts that are known to accumulate in P-bodies, while the depletion of P-body-unassociated transcripts was not as efficient (Expanded View Fig. 2D). Finally, and to confirm a potential role of reader-mediated transcript regulation in UCB, the subcellular localization pattern of YTHDF2 was investigated in immunofluorescence staining experiments (Expanded View Fig. 3D). The YTHDF2 staining pattern was found to resemble puncta, which was already reported [70]. Furthermore, distinct puncta co-localized with GFP-tagged P-bodies, suggesting a role for the m^6A-dependent and reader-mediated transcript regulation via phase separation in UCB.

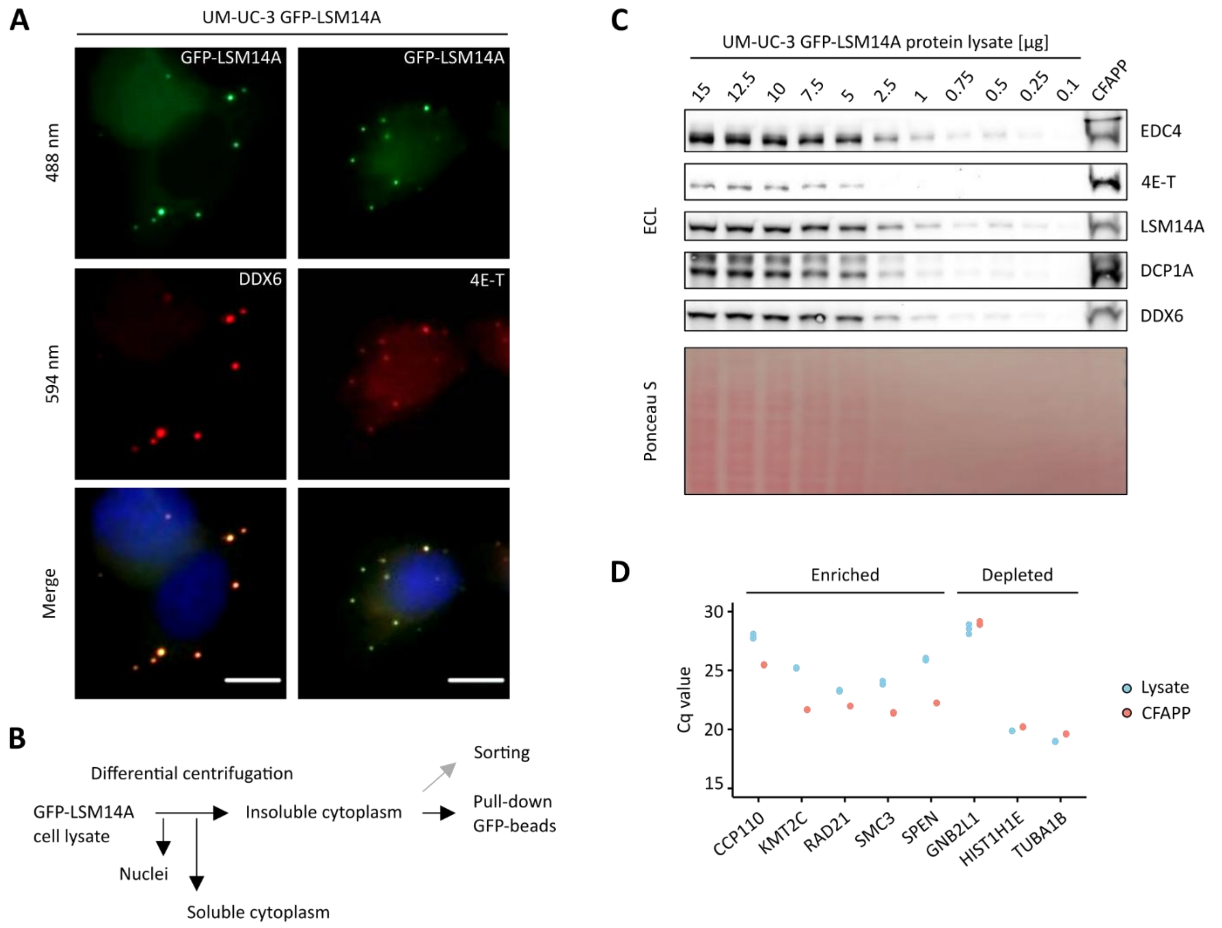

Expanded View Fig. 2: CFAPP enriches P-body-associated transcripts. A) Immunofluorescence staining of the P-body marker proteins DDX6 and 4E-T in cells expressing GFP-tagged LSM14A. Scale bar = 10 µm. **B)** Schematic workflow of CFAPP. **C)** Western blotting analysis of the CFAPP fraction showing the presence of selected P-body marker proteins. **D)** qRT-PCR analysis of known P-body enriched/depleted transcripts in total cell lysate and the CFAPP fraction. A representative example measured in technical triplicates is shown.

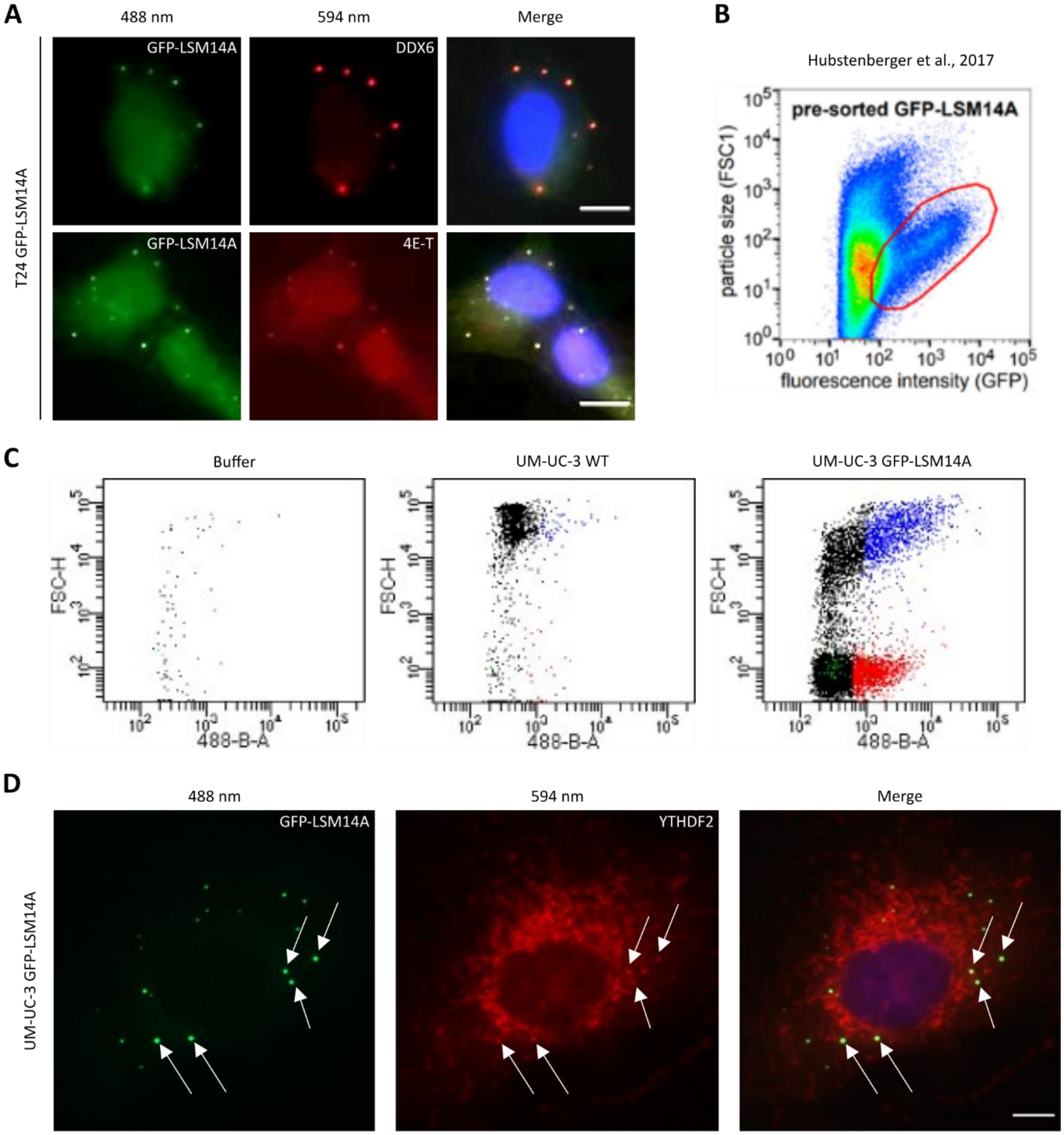

Expanded View Fig. 3: FAPS and co-localization of YTHDF2 with labeled P-bodies. A) Immunofluorescence staining of the P-body marker proteins DDX6 and 4E-T in T24 cells expressing GFP-tagged LSM14A. Scale bar = 10 µm. **B)** Sorting of GFP-tagged P-bodies as a function of size and fluorescence. The figure is taken from Hubstenberger *et al*. and displays the expected particle populations during sorting [196]. The red circle indicates the population of GFP-LSM14A-labeled P-bodies. **C)** Flow cytometric sorting of GFP-tagged P-bodies based on size and fluorescence intensity. The lysis buffer only sample showed background detection that corresponds to electronic noise. The WT sample controlled for the detection of non-fluorescent P-bodies and other particles present in the insoluble cytoplasmic fraction. The GFP-LSM14A sample showed two particle populations (highlighted in blue and red) with different forward scatters (FSCs) that were characterized by a shift in fluorescence intensity when compared to the WT sample. As another control, beads with a diameter of 500 nm (corresponding to the expected diameter of a P-body) were also sorted (highlighted in green). Comparing the signal originating from the two populations to the signal originating from the sorted beads, it is more likely that the red population represents the

GFP-tagged P-bodies. Also, the size of the particles detected in the red population is more similar to the size of the detected P-bodies in Expanded View Fig. 3B. Sorting was performed by Dr. Monika Langlotz (Flow Cytometry and FACS Core Facility, Center for Molecular Biology Heidelberg). **D)** Immunofluorescence staining of the m^6A reader YTHDF2 showed its co-localization with the GFP-labeled P-bodies in UM-UC-3 cells. Co-localization is indicated by white arrows. Scale bar = 10 µm.

7.4 Sequence information

7.4.1 pLVX-GFP-HA-FLAG vector map

This vector was kindly provided by Dr. Simge Kelekci (Division of Cancer Epigenomics, German Cancer Research Center, Heidelberg).


Created with SnapGene®
pLVX-GFP-HA-FLAG
10,149 bp
10,000
5' LTR
HIV-1 ψ
RRE
2000
cPPT/CTS
CMV enhancer
CMV promoter
Kozak sequence
EGFP
HA tag
FLAG
FLAG
FLAG
XTEN Based Linker
4000
ORF-MNX1ms
PGK promoter
PuroR
6000
WPRE
3' LTR
8000
ori
AmpR
AmpR promoter

7.5 List of publications

Koch, J., Xu, J., Bormann, F., Carneiro, V.C., Neuberger, M., Nitschke, K., Nientiedt, M., Erben, P., Michel, M.S., Rodriguez-Paredes, M., and Lyko, F. (2025). The bladder cancer m^{6}A landscape is defined by methylation dilution and 3’-UTR hypermethylation. bioRxiv, 10.1101/2025.07.11.664345.

Koch, J., and Lyko, F. (2024). Refining the role of N^6-methyladenosine in cancer. Curr Opin Genet Dev. 88, 102242. 10.1016/j.gde.2024.102242.

Koch, J., Neuberger, M., Schmidt-Dengler, M., Xu, J., Carneiro, V.C., Ellinger, J., Kriegmair, M.C., Nuhn, P., Erben, P., Michel, M.S., Helm, M., Rodriguez-Paredes, M., Nientiedt, M., and Lyko, F. (2023). Reinvestigating the clinical relevance of the m^{6}A writer METTL3 in urothelial carcinoma of the bladder. iScience 26, 107300. 10.1016/j.isci.2023.107300.

Xu, J., **Koch, J.**, Schmidt, C., Nientiedt, M., Neuberger, M., Erben, P., Michel, M.S., Rodriguez-Paredes, M., and Lyko, F. (2025). Loss of YTHDC1 m^{6}A reading function promotes invasiveness in urothelial carcinoma of the bladder. Exp Mol Med. 57, 118-130. 10.1038/s12276-024-01377-x.

Hewel, C., Wierczeiko, A., Miedema, J., Friedrich, J., Hofmann, F., Weißbach, S., Dietrich, V., Holthöfer, L., Haug, V., Mündnich, S., Schartel, L., Lehmann, L., Jensen, K.L., Diederich, S., Sys, S., Butto, T., Paul, N.W., **Koch, J.**, Lyko, F., Kraft, F., Russo, A., Schweiger, S., Lemke, E.A., Helm, M., Linke, M., and Gerber, S. (2025). Direct RNA sequencing enables improved transcriptome assessment and tracking of RNA modifications for medical applications. Nucleic Acid Res. 53, gkaf1314. 10.1093/nar/gkaf1314.

Schwickert, M., Fischer, T.R., Zimmermann, R.A., Hoba, S.N., Meidner, J.L., Weber, M., Weber, M., Stark, M.M., **Koch, J.**, Jung, N., Kersten, C., Windbergs, M., Lyko, F., Helm, M., and Schirmeister, T. (2022). Discovery of Inhibitors of DNA Methyltransferase 2, an Epitranscriptomic Modulator and Potential Target for Cancer Treatment. J Med Chem. 65, 9750-9788. 10.1021/acs.jmedchem.2c00388.

8 Acknowledgements

First, I would like to thank Frank for giving me the opportunity to pursue my PhD in his lab and for supervising me over the past 4.5 years. I enjoyed working together, and I am proud that we managed to grow m^{6}A to what it is today. I always felt that my input was valued and that my opinion mattered. You made me a better scientist, and I also thoroughly enjoyed our non-project-related conversations during our trips to Mainz or Vienna. I wish your lab and all future m^{6}A projects great success.

My gratitude also goes to my collaboration partners in Mannheim: Manuel, Malin, and Philipp. This project would not have been possible without you, and I thank you for your dedication and for providing the valuable patient samples.

Of course, the biggest thanks go to my beloved colleagues from the lab, who became my second family over the past 4.5 years:

Thank you, Vitor, whom I got to know as the crayfish PostDoc and passionate investor. Our projects were always very different, and you never had any obligation to help me - but you always did, just as you promised in our very first Zoom meeting. I am truly grateful for that, both as a colleague and as a friend.

Thank you, Manolo, the irrepressible optimist and whistling jukebox. I know no one who loves science as unconditionally as you do, and I admire you for that. Thank you for your emotional support during difficult phases and for your childish humor, which we both share (“there is only one…”). Our tennis matches and our trips to Spain and Chicago will remain unforgettable.

Thank you, Jinyun, my foster child, my m^{6}A buddy. I could not have wished for a better project partner. Working on m^{6}A was never easy for us, but we supported each other in every phase of this project and always had each other’s backs. Thank you for every moment in the lab, in the office, on walks, and on the Betzenberg. Let’s fly in the future - like spying balloons.

Thank you, Jaime, for all the lessons on awareness and the philosophy of life. Because of you, I came much closer to understanding emotional intelligence. Thank you for always having an open ear for me, and for letting me admire your Adonis body during our visits to the swimming pool. You have so much potential as a scientist, and I wish for you to go very, very far.

Thank you, Oliver, my rock, my lion, my bear, my tour guide. Without you, I would have been lost in the U.S. and would probably have gambled away all my money in Las Vegas. Thank you for taking me by the hand and for all the wonderful moments in the States (especially that cold night under the stars), at the Academics, and in the office. You had to endure quite a lot, but I know you secretly loved it - at least a little.

Thank you, Yan, for your carefree nature, your kindness, and your humor. After such a short time, you are already an icon to me. Stay exactly as you are and inspire the next generation in the lab with your personality.

Thank you, Zoe, for your willingness to take risks during our salsa lessons. It takes courage to dance with such a stiff, old man, but I truly enjoyed it. Oh, and thanks for being older than me, and for still being and always staying older.

Thank you, Ariane, for our pleasant little conversations and verbal sparring sessions over lunch, and for the creative collaboration on figure design with ChatGPT. I also see my legacy as the Cell Culture Sheriff in the best possible hands with you. I wish you all the best in the fight against Mycoplasma and fungi.

Thank you, Kati and Tanja, for your support in the lab - whether in cell culture, cloning, or dealing with endless orders. You are the constant that every dynamic work environment needs.

Thank you, Felix, the remote bioinformatician. Together, we tackled the glorious bioinformatics demands and mostly mastered them. Thank you for your support and the entertaining Zoom meetings.

I would also like to thank sports and music, in particular the 1. FC Kaiserslautern, the best football club in the world, and Deichkind, the best band in the world. Thank you for pulling me out of science every now and then.

A big thank you goes to my family, who always supported me emotionally. Your contribution to this achievement cannot be overstated, and I am deeply grateful that you accompanied my journey “vum klääne Pälzer Bu” to a real scientist. A special thank you goes to my mom, whose ears I talked off more than once. You were always there for me, and I treasure that more than words can say.

And lastly, a giga-thank you to my Perlche, my Zaunkönigin, my soulmate. Thank you for always making me laugh, for roasting me, for lifting me up, and for motivating and supporting me all the way to the end. We collected and shared so many moments in this lab. This lab was the beginning of our story, and I wish for that story to never end.

9 References

1. Dyrskjøt, L., Hansel, D.E., Efstathiou, J.A., Knowles, M.A., Galsky, M.D., Teoh, J., and Theodorescu, D. (2023). Bladder cancer. Nat Rev Dis Primers *9*, 58. 10.1038/s41572-023-00468-9.
2. Siegel, R.L., Kratzer, T.B., Giaquinto, A.N., Sung, H., and Jemal, A. (2025). Cancer statistics, 2025. CA Cancer J Clin *75*, 10–45. 10.3322/caac.21871.
3. Berdik, C. (2017). Unlocking bladder cancer. Nature *551*, S34–s35. 10.1038/551S34a.
4. Lopez-Beltran, A., Cookson, M.S., Guercio, B.J., and Cheng, L. (2024). Advances in diagnosis and treatment of bladder cancer. Bmj *384*, e076743. 10.1136/bmj-2023-076743.
5. Richters, A., Aben, K.K.H., and Kiemeney, L. (2020). The global burden of urinary bladder cancer: an update. World J Urol *38*, 1895–1904. 10.1007/s00345-019-02984-4.
6. Batista, R., Vinagre, N., Meireles, S., Vinagre, J., Prazeres, H., Leão, R., Máximo, V., and Soares, P. (2020). Biomarkers for Bladder Cancer Diagnosis and Surveillance: A Comprehensive Review. Diagnostics (Basel) *10*. 10.3390/diagnostics10010039.
7. Gill, E., and Perks, C.M. (2024). Mini-Review: Current Bladder Cancer Treatment-The Need for Improvement. Int J Mol Sci *25*. 10.3390/ijms25031557.
8. Ke, S., Pandya-Jones, A., Saito, Y., Fak, J.J., Vågbø, C.B., Geula, S., Hanna, J.H., Black, D.L., Darnell, J.E., Jr., and Darnell, R.B. (2017). m(6)A mRNA modifications are deposited in nascent pre-mRNA and are not required for splicing but do specify cytoplasmic turnover. Genes Dev *31*, 990–1006. 10.1101/gad.301036.117.
9. He, P.C., and He, C. (2021). m(6) A RNA methylation: from mechanisms to therapeutic potential. Embo j *40*, e105977. 10.15252/embj.2020105977.
10. Wang, X., Feng, J., Xue, Y., Guan, Z., Zhang, D., Liu, Z., Gong, Z., Wang, Q., Huang, J., Tang, C., et al. (2016). Structural basis of N(6)-adenosine methylation by the METTL3-METTL14 complex. Nature *534*, 575–578. 10.1038/nature18298.
11. Wang, P., Doxtader, K.A., and Nam, Y. (2016). Structural Basis for Cooperative Function of Mettl3 and Mettl14 Methyltransferases. Molecular cell *63*, 306–317. 10.1016/j.molcel.2016.05.041.
12. Śledź, P., and Jinek, M. (2016). Structural insights into the molecular mechanism of the m(6)A writer complex. Elife *5*. 10.7554/eLife.18434.
13. Iyer, L.M., Zhang, D., and Aravind, L. (2016). Adenine methylation in eukaryotes: Apprehending the complex evolutionary history and functional potential of an epigenetic modification. Bioessays *38*, 27–40. 10.1002/bies.201500104.
14. Knuckles, P., Lence, T., Haussmann, I.U., Jacob, D., Kreim, N., Carl, S.H., Masiello, I., Hares, T., Villaseñor, R., Hess, D., et al. (2018). Zc3h13/Flacc is required for adenosine methylation by bridging the mRNA-binding factor Rbm15/Spenito to the m(6)A machinery component Wtap/Fl(2)d. Genes Dev *32*, 415–429. 10.1101/gad.309146.117.
15. Su, S., Li, S., Deng, T., Gao, M., Yin, Y., Wu, B., Peng, C., Liu, J., Ma, J., and Zhang, K. (2022). Cryo-EM structures of human m6A writer complexes. Cell Research *32*, 982–994. 10.1038/s41422-022-00725-8.

16. Ping, X.-L., Sun, B.-F., Wang, L., Xiao, W., Yang, X., Wang, W.-J., Adhikari, S., Shi, Y., Lv, Y., Chen, Y.-S., et al. (2014). Mammalian WTAP is a regulatory subunit of the RNA N6-methyladenosine methyltransferase. Cell Research *24*, 177–189. 10.1038/cr.2014.3.
17. Schwartz, S., Mumbach, M.R., Jovanovic, M., Wang, T., Maciag, K., Bushkin, G.G., Mertins, P., Ter-Ovanesyan, D., Habib, N., Cacchiarelli, D., et al. (2014). Perturbation of m6A writers reveals two distinct classes of mRNA methylation at internal and 5' sites. Cell Rep *8*, 284–296. 10.1016/j.celrep.2014.05.048.
18. Horiuchi, K., Kawamura, T., Iwanari, H., Ohashi, R., Naito, M., Kodama, T., and Hamakubo, T. (2013). Identification of Wilms' tumor 1-associating protein complex and its role in alternative splicing and the cell cycle. J Biol Chem *288*, 33292–33302. 10.1074/jbc.M113.500397.
19. Patil, D.P., Chen, C.-K., Pickering, B.F., Chow, A., Jackson, C., Guttman, M., and Jaffrey, S.R. (2016). m6A RNA methylation promotes XIST-mediated transcriptional repression. Nature *537*, 369–373. 10.1038/nature19342.
20. Yue, Y., Liu, J., Cui, X., Cao, J., Luo, G., Zhang, Z., Cheng, T., Gao, M., Shu, X., Ma, H., et al. (2018). VIRMA mediates preferential m(6)A mRNA methylation in 3'UTR and near stop codon and associates with alternative polyadenylation. Cell Discov *4*, 10. 10.1038/s41421-018-0019-0.
21. Wen, J., Lv, R., Ma, H., Shen, H., He, C., Wang, J., Jiao, F., Liu, H., Yang, P., Tan, L., et al. (2018). Zc3h13 Regulates Nuclear RNA m(6)A Methylation and Mouse Embryonic Stem Cell Self-Renewal. Mol Cell *69*, 1028–1038.e1026. 10.1016/j.molcel.2018.02.015.
22. Bawankar, P., Lence, T., Paolantoni, C., Haussmann, I.U., Kazlauskiene, M., Jacob, D., Heidelberger, J.B., Richter, F.M., Nallasivan, M.P., Morin, V., et al. (2021). Hakai is required for stabilization of core components of the m(6)A mRNA methylation machinery. Nat Commun *12*, 3778. 10.1038/s41467-021-23892-5.
23. Hong, J., Xu, K., and Lee, J.H. (2022). Biological roles of the RNA m6A modification and its implications in cancer. Experimental & Molecular Medicine *54*, 1822–1832. 10.1038/s12276-022-00897-8.
24. Ramsköld, D., Wang, E.T., Burge, C.B., and Sandberg, R. (2009). An abundance of ubiquitously expressed genes revealed by tissue transcriptome sequence data. PLoS Comput Biol *5*, e1000598. 10.1371/journal.pcbi.1000598.
25. Dominissini, D., Moshitch-Moshkovitz, S., Schwartz, S., Salmon-Divon, M., Ungar, L., Osenberg, S., Cesarkas, K., Jacob-Hirsch, J., Amariglio, N., Kupiec, M., et al. (2012). Topology of the human and mouse m6A RNA methylomes revealed by m6A-seq. Nature *485*, 201–206. 10.1038/nature11112.
26. Meyer, K.D., Saletore, Y., Zumbo, P., Elemento, O., Mason, C.E., and Jaffrey, S.R. (2012). Comprehensive analysis of mRNA methylation reveals enrichment in 3' UTRs and near stop codons. Cell *149*, 1635–1646. 10.1016/j.cell.2012.05.003.
27. Liu, C., Sun, H., Yi, Y., Shen, W., Li, K., Xiao, Y., Li, F., Li, Y., Hou, Y., Lu, B., et al. (2023). Absolute quantification of single-base m6A methylation in the mammalian transcriptome using GLORI. Nature Biotechnology *41*, 355–366. 10.1038/s41587-022-01487-9.

28. Perry, R.P., Kelley, D.E., Friderici, K., and Rottman, F. (1975). The methylated constituents of L cell messenger RNA: evidence for an unusual cluster at the 5' terminus. Cell *4*, 387–394. 10.1016/0092-8674(75)90159-2.
29. Schibler, U., Kelley, D.E., and Perry, R.P. (1977). Comparison of methylated sequences in messenger RNA and heterogeneous nuclear RNA from mouse L cells. J Mol Biol *115*, 695–714. 10.1016/0022-2836(77)90110-3.
30. Wei, C.M., and Moss, B. (1977). Nucleotide sequences at the N6-methyladenosine sites of HeLa cell messenger ribonucleic acid. Biochemistry *16*, 1672–1676. 10.1021/bi00627a023.
31. Kane, S.E., and Beemon, K. (1987). Inhibition of methylation at two internal N6-methyladenosine sites caused by GAC to GAU mutations. J Biol Chem *262*, 3422–3427.
32. Harper, J.E., Miceli, S.M., Roberts, R.J., and Manley, J.L. (1990). Sequence specificity of the human mRNA N6-adenosine methylase in vitro. Nucleic Acids Res *18*, 5735–5741. 10.1093/nar/18.19.5735.
33. Ke, S., Alemu, E.A., Mertens, C., Gantman, E.C., Fak, J.J., Mele, A., Haripal, B., Zucker-Scharff, I., Moore, M.J., Park, C.Y., et al. (2015). A majority of m6A residues are in the last exons, allowing the potential for 3' UTR regulation. Genes Dev *29*, 2037–2053. 10.1101/gad.269415.115.
34. Linder, B., Grozhik, A.V., Olarerin-George, A.O., Meydan, C., Mason, C.E., and Jaffrey, S.R. (2015). Single-nucleotide-resolution mapping of m6A and m6Am throughout the transcriptome. Nature Methods *12*, 767–772. 10.1038/nmeth.3453.
35. Zhang, C., Scott, R.L., Tunes, L., Hsieh, M.H., Wang, P., Kumar, A., Khadgi, B.B., Yang, Y.Y., Doxtader Lacy, K.A., Herrell, E., et al. (2024). Cancer mutations rewire the RNA methylation specificity of METTL3-METTL14. Sci Adv *10*, eads4750. 10.1126/sciadv.ads4750.
36. Huang, H., Weng, H., Zhou, K., Wu, T., Zhao, B.S., Sun, M., Chen, Z., Deng, X., Xiao, G., Auer, F., et al. (2019). Histone H3 trimethylation at lysine 36 guides m(6)A RNA modification co-transcriptionally. Nature *567*, 414–419. 10.1038/s41586-019-1016-7.
37. Uzonyi, A., Dierks, D., Nir, R., Kwon, O.S., Toth, U., Barbosa, I., Burel, C., Brandis, A., Rossmanith, W., Le Hir, H., et al. (2023). Exclusion of m6A from splice-site proximal regions by the exon junction complex dictates m6A topologies and mRNA stability. Mol Cell *83*, 237–251.e237. 10.1016/j.molcel.2022.12.026.
38. He, P.C., Wei, J., Dou, X., Harada, B.T., Zhang, Z., Ge, R., Liu, C., Zhang, L.-S., Yu, X., Wang, S., et al. (2023). Exon architecture controls mRNA m6A suppression and gene expression. Science *379*, 677–682. doi:10.1126/science.abj9090.
39. Yang, X., Triboulet, R., Liu, Q., Sendinc, E., and Gregory, R.I. (2022). Exon junction complex shapes the m(6)A epitranscriptome. Nat Commun *13*, 7904. 10.1038/s41467-022-35643-1.
40. Meiser, N., Mench, N., and Hengesbach, M. (2020). RNA secondary structure dependence in METTL3-METTL14 mRNA methylation is modulated by the N-terminal domain of METTL3. Biol Chem *402*, 89–98. 10.1515/hsz-2020-0265.
41. Shachar, R., Dierks, D., Garcia-Campos, M.A., Uzonyi, A., Toth, U., Rossmanith, W., and Schwartz, S. (2024). Dissecting the sequence and structural determinants guiding m6A

deposition and evolution via inter- and intra-species hybrids. Genome Biol *25*, 48. 10.1186/s13059-024-03182-1.

42. Barbieri, I., Tzelepis, K., Pandolfini, L., Shi, J., Millán-Zambrano, G., Robson, S.C., Aspris, D., Migliori, V., Bannister, A.J., Han, N., et al. (2017). Promoter-bound METTL3 maintains myeloid leukaemia by m(6)A-dependent translation control. Nature *552*, 126–131. 10.1038/nature24678.
43. Bertero, A., Brown, S., Madrigal, P., Osnato, A., Ortmann, D., Yiangou, L., Kadiwala, J., Hubner, N.C., de Los Mozos, I.R., Sadée, C., et al. (2018). The SMAD2/3 interactome reveals that TGFβ controls m(6)A mRNA methylation in pluripotency. Nature *555*, 256–259. 10.1038/nature25784.
44. Fish, L., Navickas, A., Culbertson, B., Xu, Y., Nguyen, H.C.B., Zhang, S., Hochman, M., Okimoto, R., Dill, B.D., Molina, H., et al. (2019). Nuclear TARBP2 Drives Oncogenic Dysregulation of RNA Splicing and Decay. Mol Cell *75*, 967–981.e969. 10.1016/j.molcel.2019.06.001.
45. Slobodin, B., Han, R., Calderone, V., Vrielink, J., Loayza-Puch, F., Elkon, R., and Agami, R. (2017). Transcription Impacts the Efficiency of mRNA Translation via Co-transcriptional N6-adenosine Methylation. Cell *169*, 326–337.e312. 10.1016/j.cell.2017.03.031.
46. Patil, D.P., Pickering, B.F., and Jaffrey, S.R. (2018). Reading m(6)A in the Transcriptome: m(6)A-Binding Proteins. Trends Cell Biol *28*, 113–127. 10.1016/j.tcb.2017.10.001.
47. Huang, H., Weng, H., Sun, W., Qin, X., Shi, H., Wu, H., Zhao, B.S., Mesquita, A., Liu, C., Yuan, C.L., et al. (2018). Recognition of RNA N(6)-methyladenosine by IGF2BP proteins enhances mRNA stability and translation. Nat Cell Biol *20*, 285–295. 10.1038/s41556-018-0045-z.
48. Duan, M., Liu, H., Xu, S., Yang, Z., Zhang, F., Wang, G., Wang, Y., Zhao, S., and Jiang, X. (2024). IGF2BPs as novel m(6)A readers: Diverse roles in regulating cancer cell biological functions, hypoxia adaptation, metabolism, and immunosuppressive tumor microenvironment. Genes Dis *11*, 890–920. 10.1016/j.gendis.2023.06.017.
49. Xiao, W., Adhikari, S., Dahal, U., Chen, Y.S., Hao, Y.J., Sun, B.F., Sun, H.Y., Li, A., Ping, X.L., Lai, W.Y., et al. (2016). Nuclear m(6)A Reader YTHDC1 Regulates mRNA Splicing. Mol Cell *61*, 507–519. 10.1016/j.molcel.2016.01.012.
50. Kasowitz, S.D., Ma, J., Anderson, S.J., Leu, N.A., Xu, Y., Gregory, B.D., Schultz, R.M., and Wang, P.J. (2018). Nuclear m6A reader YTHDC1 regulates alternative polyadenylation and splicing during mouse oocyte development. PLoS Genet *14*, e1007412. 10.1371/journal.pgen.1007412.
51. Roundtree, I.A., Luo, G.Z., Zhang, Z., Wang, X., Zhou, T., Cui, Y., Sha, J., Huang, X., Guerrero, L., Xie, P., et al. (2017). YTHDC1 mediates nuclear export of N(6)-methyladenosine methylated mRNAs. Elife *6*. 10.7554/eLife.31311.
52. Flamand, M.N., Tegowski, M., and Meyer, K.D. (2023). The Proteins of mRNA Modification: Writers, Readers, and Erasers. Annu Rev Biochem *92*, 145–173. 10.1146/annurev-biochem-052521-035330.
53. Li, Y., Xia, L., Tan, K., Ye, X., Zuo, Z., Li, M., Xiao, R., Wang, Z., Liu, X., Deng, M., et al. (2020). N(6)-Methyladenosine co-transcriptionally directs the demethylation of histone H3K9me2. Nat Genet *52*, 870–877. 10.1038/s41588-020-0677-3.

54. Liu, J., Gao, M., He, J., Wu, K., Lin, S., Jin, L., Chen, Y., Liu, H., Shi, J., Wang, X., et al. (2021). The RNA m(6)A reader YTHDC1 silences retrotransposons and guards ES cell identity. Nature *591*, 322–326. 10.1038/s41586-021-03313-9.
55. Liu, J., Dou, X., Chen, C., Chen, C., Liu, C., Xu, M.M., Zhao, S., Shen, B., Gao, Y., Han, D., and He, C. (2020). N (6)-methyladenosine of chromosome-associated regulatory RNA regulates chromatin state and transcription. Science *367*, 580–586. 10.1126/science.aay6018.
56. Koch, J., and Lyko, F. (2024). Refining the role of N6-methyladenosine in cancer. Current Opinion in Genetics & Development *88*, 102242. https://doi.org/10.1016/j.gde.2024.102242.
57. Hartmann, A.M., Nayler, O., Schwaiger, F.W., Obermeier, A., and Stamm, S. (1999). The interaction and colocalization of Sam68 with the splicing-associated factor YT521-B in nuclear dots is regulated by the Src family kinase p59(fyn). Mol Biol Cell *10*, 3909–3926. 10.1091/mbc.10.11.3909.
58. Nayler, O., Hartmann, A.M., and Stamm, S. (2000). The ER repeat protein YT521-B localizes to a novel subnuclear compartment. J Cell Biol *150*, 949–962. 10.1083/jcb.150.5.949.
59. Cheng, Y., Xie, W., Pickering, B.F., Chu, K.L., Savino, A.M., Yang, X., Luo, H., Nguyen, D.T.T., Mo, S., Barin, E., et al. (2021). N6-Methyladenosine on mRNA facilitates a phase-separated nuclear body that suppresses myeloid leukemic differentiation. Cancer Cell *39*, 958–972.e958. 10.1016/j.ccell.2021.04.017.
60. Wang, X., Liu, C., Zhang, S., Yan, H., Zhang, L., Jiang, A., Liu, Y., Feng, Y., Li, D., Guo, Y., et al. (2021). N(6)-methyladenosine modification of MALAT1 promotes metastasis via reshaping nuclear speckles. Dev Cell *56*, 702–715.e708. 10.1016/j.devcel.2021.01.015.
61. Wang, X., Zhao, B.S., Roundtree, I.A., Lu, Z., Han, D., Ma, H., Weng, X., Chen, K., Shi, H., and He, C. (2015). N(6)-methyladenosine Modulates Messenger RNA Translation Efficiency. Cell *161*, 1388–1399. 10.1016/j.cell.2015.05.014.
62. Wang, X., Lu, Z., Gomez, A., Hon, G.C., Yue, Y., Han, D., Fu, Y., Parisien, M., Dai, Q., Jia, G., et al. (2014). N6-methyladenosine-dependent regulation of messenger RNA stability. Nature *505*, 117–120. 10.1038/nature12730.
63. Du, H., Zhao, Y., He, J., Zhang, Y., Xi, H., Liu, M., Ma, J., and Wu, L. (2016). YTHDF2 destabilizes m6A-containing RNA through direct recruitment of the CCR4–NOT deadenylase complex. Nature Communications *7*, 12626. 10.1038/ncomms12626.
64. Shi, H., Wang, X., Lu, Z., Zhao, B.S., Ma, H., Hsu, P.J., Liu, C., and He, C. (2017). YTHDF3 facilitates translation and decay of N6-methyladenosine-modified RNA. Cell Research *27*, 315–328. 10.1038/cr.2017.15.
65. Li, A., Chen, Y.-S., Ping, X.-L., Yang, X., Xiao, W., Yang, Y., Sun, H.-Y., Zhu, Q., Baidya, P., Wang, X., et al. (2017). Cytoplasmic m6A reader YTHDF3 promotes mRNA translation. Cell Research *27*, 444–447. 10.1038/cr.2017.10.
66. Zaccara, S., and Jaffrey, S.R. (2020). A Unified Model for the Function of YTHDF Proteins in Regulating m(6)A-Modified mRNA. Cell *181*, 1582–1595.e1518. 10.1016/j.cell.2020.05.012.
67. Lasman, L., Krupalnik, V., Viukov, S., Mor, N., Aguilera-Castrejon, A., Schneir, D., Bayerl, J., Mizrahi, O., Peles, S., Tawil, S., et al. (2020). Context-dependent functional

compensation between Ythdf m(6)A reader proteins. Genes Dev *34*, 1373–1391. 10.1101/gad.340695.120.

68. Park, O.H., Ha, H., Lee, Y., Boo, S.H., Kwon, D.H., Song, H.K., and Kim, Y.K. (2019). Endoribonucleolytic Cleavage of m(6)A-Containing RNAs by RNase P/MRP Complex. Mol Cell *74*, 494–507.e498. 10.1016/j.molcel.2019.02.034.
69. Boo, S.H., Ha, H., Lee, Y., Shin, M.K., Lee, S., and Kim, Y.K. (2022). UPF1 promotes rapid degradation of m(6)A-containing RNAs. Cell Rep *39*, 110861. 10.1016/j.celrep.2022.110861.
70. Ries, R.J., Zaccara, S., Klein, P., Olarerin-George, A., Namkoong, S., Pickering, B.F., Patil, D.P., Kwak, H., Lee, J.H., and Jaffrey, S.R. (2019). m6A enhances the phase separation potential of mRNA. Nature *571*, 424–428. 10.1038/s41586-019-1374-1.
71. Fu, Y., and Zhuang, X. (2020). m(6)A-binding YTHDF proteins promote stress granule formation. Nat Chem Biol *16*, 955–963. 10.1038/s41589-020-0524-y.
72. Ries, R.J., Pickering, B.F., Poh, H.X., Namkoong, S., and Jaffrey, S.R. (2023). m(6)A governs length-dependent enrichment of mRNAs in stress granules. Nat Struct Mol Biol *30*, 1525–1535. 10.1038/s41594-023-01089-2.
73. Meyer, K.D., Patil, D.P., Zhou, J., Zinoviev, A., Skabkin, M.A., Elemento, O., Pestova, T.V., Qian, S.B., and Jaffrey, S.R. (2015). 5' UTR m(6)A Promotes Cap-Independent Translation. Cell *163*, 999–1010. 10.1016/j.cell.2015.10.012.
74. Choe, J., Lin, S., Zhang, W., Liu, Q., Wang, L., Ramirez-Moya, J., Du, P., Kim, W., Tang, S., Sliz, P., et al. (2018). mRNA circularization by METTL3-eIF3h enhances translation and promotes oncogenesis. Nature *561*, 556–560. 10.1038/s41586-018-0538-8.
75. Shan, T., Liu, F., Wen, M., Chen, Z., Li, S., Wang, Y., Cheng, H., and Zhou, Y. (2023). m(6)A modification negatively regulates translation by switching mRNA from polysome to P-body via IGF2BP3. Mol Cell *83*, 4494–4508. 10.1016/j.molcel.2023.10.040.
76. Helm, M., Lyko, F., and Motorin, Y. (2019). Limited antibody specificity compromises epitranscriptomic analyses. Nat Commun *10*, 5669. 10.1038/s41467-019-13684-3.
77. Legrand, C., Tuorto, F., Hartmann, M., Liebers, R., Jacob, D., Helm, M., and Lyko, F. (2017). Statistically robust methylation calling for whole-transcriptome bisulfite sequencing reveals distinct methylation patterns for mouse RNAs. Genome Res *27*, 1589–1596. 10.1101/gr.210666.116.
78. Thüring, K., Schmid, K., Keller, P., and Helm, M. (2016). Analysis of RNA modifications by liquid chromatography-tandem mass spectrometry. Methods *107*, 48–56. 10.1016/j.ymeth.2016.03.019.
79. McIntyre, A.B.R., Gokhale, N.S., Cerchietti, L., Jaffrey, S.R., Horner, S.M., and Mason, C.E. (2020). Limits in the detection of m6A changes using MeRIP/m6A-seq. Scientific Reports *10*, 6590. 10.1038/s41598-020-63355-3.
80. Molinie, B., Wang, J., Lim, K.S., Hillebrand, R., Lu, Z.-x., Van Wittenberghe, N., Howard, B.D., Daneshvar, K., Mullen, A.C., Dedon, P., et al. (2016). m6A-LAIC-seq reveals the census and complexity of the m6A epitranscriptome. Nature Methods *13*, 692–698. 10.1038/nmeth.3898.
81. Dierks, D., Garcia-Campos, M.A., Uzonyi, A., Safra, M., Edelheit, S., Rossi, A., Sideri, T., Varier, R.A., Brandis, A., Stelzer, Y., et al. (2021). Multiplexed profiling facilitates robust

m6A quantification at site, gene and sample resolution. Nature Methods *18*, 1060–1067. 10.1038/s41592-021-01242-z.

82. Garcia-Campos, M.A., Edelheit, S., Toth, U., Safra, M., Shachar, R., Viukov, S., Winkler, R., Nir, R., Lasman, L., Brandis, A., et al. (2019). Deciphering the "m(6)A Code" via Antibody-Independent Quantitative Profiling. Cell *178*, 731–747.e716. 10.1016/j.cell.2019.06.013.
83. Zhang, Z., Chen, L.Q., Zhao, Y.L., Yang, C.G., Roundtree, I.A., Zhang, Z., Ren, J., Xie, W., He, C., and Luo, G.Z. (2019). Single-base mapping of m(6)A by an antibody-independent method. Sci Adv *5*, eaax0250. 10.1126/sciadv.aax0250.
84. Zhang, Z., Chen, T., Chen, H.-X., Xie, Y.-Y., Chen, L.-Q., Zhao, Y.-L., Liu, B.-D., Jin, L., Zhang, W., Liu, C., et al. (2021). Systematic calibration of epitranscriptomic maps using a synthetic modification-free RNA library. Nature Methods *18*, 1213–1222. 10.1038/s41592-021-01280-7.
85. Meyer, K.D. (2019). DART-seq: an antibody-free method for global m6A detection. Nature Methods *16*, 1275–1280. 10.1038/s41592-019-0570-0.
86. Tegowski, M., Zhu, H., and Meyer, K.D. (2022). Detecting m(6)A with In Vitro DART-Seq. Methods Mol Biol *2404*, 363–374. 10.1007/978-1-0716-1851-6_20.
87. Tegowski, M., Flamand, M.N., and Meyer, K.D. (2022). scDART-seq reveals distinct m(6)A signatures and mRNA methylation heterogeneity in single cells. Mol Cell. 10.1016/j.molcel.2021.12.038.
88. Shu, X., Cao, J., Cheng, M., Xiang, S., Gao, M., Li, T., Ying, X., Wang, F., Yue, Y., Lu, Z., et al. (2020). A metabolic labeling method detects m(6)A transcriptome-wide at single base resolution. Nat Chem Biol *16*, 887–895. 10.1038/s41589-020-0526-9.
89. Wang, Y., Xiao, Y., Dong, S., Yu, Q., and Jia, G. (2020). Antibody-free enzyme-assisted chemical approach for detection of N6-methyladenosine. Nature Chemical Biology *16*, 896–903. 10.1038/s41589-020-0525-x.
90. Hartstock, K., Nilges, B.S., Ovcharenko, A., Cornelissen, N.V., Püllen, N., Lawrence-Dörner, A.M., Leidel, S.A., and Rentmeister, A. (2018). Enzymatic or In Vivo Installation of Propargyl Groups in Combination with Click Chemistry for the Enrichment and Detection of Methyltransferase Target Sites in RNA. Angew Chem Int Ed Engl *57*, 6342–6346. 10.1002/anie.201800188.
91. Hartstock, K., Kueck, N.A., Spacek, P., Ovcharenko, A., Hüwel, S., Cornelissen, N.V., Bollu, A., Dieterich, C., and Rentmeister, A. (2023). MePMe-seq: antibody-free simultaneous m(6)A and m(5)C mapping in mRNA by metabolic propargyl labeling and sequencing. Nat Commun *14*, 7154. 10.1038/s41467-023-42832-z.
92. Hu, L., Liu, S., Peng, Y., Ge, R., Su, R., Senevirathne, C., Harada, B.T., Dai, Q., Wei, J., Zhang, L., et al. (2022). m6A RNA modifications are measured at single-base resolution across the mammalian transcriptome. Nature Biotechnology *40*, 1210–1219. 10.1038/s41587-022-01243-z.
93. Ge, R., Ye, C., Peng, Y., Dai, Q., Zhao, Y., Liu, S., Wang, P., Hu, L., and He, C. (2023). m6A-SAC-seq for quantitative whole transcriptome m6A profiling. Nature Protocols *18*, 626–657. 10.1038/s41596-022-00765-9.
94. Clark, S.J., Harrison, J., Paul, C.L., and Frommer, M. (1994). High sensitivity mapping of methylated cytosines. Nucleic Acids Res *22*, 2990–2997. 10.1093/nar/22.15.2990.

95. Schaefer, M., Pollex, T., Hanna, K., and Lyko, F. (2009). RNA cytosine methylation analysis by bisulfite sequencing. Nucleic Acids Res *37*, e12. 10.1093/nar/gkn954.
96. Motorin, Y., Lyko, F., and Helm, M. (2010). 5-methylcytosine in RNA: detection, enzymatic formation and biological functions. Nucleic Acids Res *38*, 1415–1430. 10.1093/nar/gkp1117.
97. Bock, C., Tomazou, E.M., Brinkman, A.B., Müller, F., Simmer, F., Gu, H., Jäger, N., Gnirke, A., Stunnenberg, H.G., and Meissner, A. (2010). Quantitative comparison of genome-wide DNA methylation mapping technologies. Nat Biotechnol *28*, 1106–1114. 10.1038/nbt.1681.
98. Garalde, D.R., Snell, E.A., Jachimowicz, D., Sipos, B., Lloyd, J.H., Bruce, M., Pantic, N., Admassu, T., James, P., Warland, A., et al. (2018). Highly parallel direct RNA sequencing on an array of nanopores. Nature Methods *15*, 201–206. 10.1038/nmeth.4577.
99. Liu, H., Begik, O., Lucas, M.C., Ramirez, J.M., Mason, C.E., Wiener, D., Schwartz, S., Mattick, J.S., Smith, M.A., and Novoa, E.M. (2019). Accurate detection of m6A RNA modifications in native RNA sequences. Nature Communications *10*, 4079. 10.1038/s41467-019-11713-9.
100. Wan, Y.K., Hendra, C., Pratanwanich, P.N., and Göke, J. (2022). Beyond sequencing: machine learning algorithms extract biology hidden in Nanopore signal data. Trends Genet *38*, 246–257. 10.1016/j.tig.2021.09.001.
101. Leger, A., Amaral, P.P., Pandolfini, L., Capitanchik, C., Capraro, F., Miano, V., Migliori, V., Toolan-Kerr, P., Sideri, T., Enright, A.J., et al. (2021). RNA modifications detection by comparative Nanopore direct RNA sequencing. Nat Commun *12*, 7198. 10.1038/s41467-021-27393-3.
102. Hendra, C., Pratanwanich, P.N., Wan, Y.K., Goh, W.S.S., Thiery, A., and Göke, J. (2022). Detection of m6A from direct RNA sequencing using a multiple instance learning framework. Nat Methods *19*, 1590–1598. 10.1038/s41592-022-01666-1.
103. Huang, S., Wylder, A.C., and Pan, T. (2024). Simultaneous nanopore profiling of mRNA m(6)A and pseudouridine reveals translation coordination. Nat Biotechnol. 10.1038/s41587-024-02135-0.
104. Lan, Q., Liu, P.Y., Haase, J., Bell, J.L., Hüttelmaier, S., and Liu, T. (2019). The Critical Role of RNA m(6)A Methylation in Cancer. Cancer Res *79*, 1285–1292. 10.1158/0008-5472.Can-18-2965.
105. Deng, L.-J., Deng, W.-Q., Fan, S.-R., Chen, M.-F., Qi, M., Lyu, W.-Y., Qi, Q., Tiwari, A.K., Chen, J.-X., Zhang, D.-M., and Chen, Z.-S. (2022). m6A modification: recent advances, anticancer targeted drug discovery and beyond. Mol Cancer *21*, 52. 10.1186/s12943-022-01510-2.
106. Deng, X., Qing, Y., Horne, D., Huang, H., and Chen, J. (2023). The roles and implications of RNA m(6)A modification in cancer. Nat Rev Clin Oncol *20*, 507–526. 10.1038/s41571-023-00774-x.
107. Vu, L.P., Pickering, B.F., Cheng, Y., Zaccara, S., Nguyen, D., Minuesa, G., Chou, T., Chow, A., Saletore, Y., MacKay, M., et al. (2017). The N(6)-methyladenosine (m(6)A)-forming enzyme METTL3 controls myeloid differentiation of normal hematopoietic and leukemia cells. Nat Med *23*, 1369–1376. 10.1038/nm.4416.

108. Li, Z., Peng, Y., Li, J., Chen, Z., Chen, F., Tu, J., Lin, S., and Wang, H. (2020). N(6)-methyladenosine regulates glycolysis of cancer cells through PDK4. Nat Commun *11*, 2578. 10.1038/s41467-020-16306-5.
109. Lin, S., Liu, J., Jiang, W., Wang, P., Sun, C., Wang, X., Chen, Y., and Wang, H. (2019). METTL3 Promotes the Proliferation and Mobility of Gastric Cancer Cells. Open Med (Wars) *14*, 25–31. 10.1515/med-2019-0005.
110. Zhao, X., and Cui, L. (2019). Development and validation of a m(6)A RNA methylation regulators-based signature for predicting the prognosis of head and neck squamous cell carcinoma. Am J Cancer Res *9*, 2156–2169.
111. Chen, M., Wei, L., Law, C.T., Tsang, F.H., Shen, J., Cheng, C.L., Tsang, L.H., Ho, D.W., Chiu, D.K., Lee, J.M., et al. (2018). RNA N6-methyladenosine methyltransferase-like 3 promotes liver cancer progression through YTHDF2-dependent posttranscriptional silencing of SOCS2. Hepatology *67*, 2254–2270. 10.1002/hep.29683.
112. Lin, S., Choe, J., Du, P., Triboulet, R., and Gregory, R.I. (2016). The m(6)A Methyltransferase METTL3 Promotes Translation in Human Cancer Cells. Mol Cell *62*, 335–345. 10.1016/j.molcel.2016.03.021.
113. Dahal, U., Le, K., and Gupta, M. (2019). RNA m6A methyltransferase METTL3 regulates invasiveness of melanoma cells by matrix metallopeptidase 2. Melanoma Res *29*, 382–389. 10.1097/cmr.0000000000000580.
114. Taketo, K., Konno, M., Asai, A., Koseki, J., Toratani, M., Satoh, T., Doki, Y., Mori, M., Ishii, H., and Ogawa, K. (2018). The epitranscriptome m6A writer METTL3 promotes chemo- and radioresistance in pancreatic cancer cells. Int J Oncol *52*, 621–629. 10.3892/ijo.2017.4219.
115. Cai, J., Yang, F., Zhan, H., Situ, J., Li, W., Mao, Y., and Luo, Y. (2019). RNA m(6)A Methyltransferase METTL3 Promotes The Growth Of Prostate Cancer By Regulating Hedgehog Pathway. Onco Targets Ther *12*, 9143–9152. 10.2147/ott.S226796.
116. Hua, W., Zhao, Y., Jin, X., Yu, D., He, J., Xie, D., and Duan, P. (2018). METTL3 promotes ovarian carcinoma growth and invasion through the regulation of AXL translation and epithelial to mesenchymal transition. Gynecol Oncol *151*, 356–365. 10.1016/j.ygyno.2018.09.015.
117. Cheng, M., Sheng, L., Gao, Q., Xiong, Q., Zhang, H., Wu, M., Liang, Y., Zhu, F., Zhang, Y., Zhang, X., et al. (2019). The m(6)A methyltransferase METTL3 promotes bladder cancer progression via AFF4/NF-κB/MYC signaling network. Oncogene *38*, 3667–3680. 10.1038/s41388-019-0683-z.
118. Zhao, S., Liu, J., Nanga, P., Liu, Y., Cicek, A.E., Knoblauch, N., He, C., Stephens, M., and He, X. (2019). Detailed modeling of positive selection improves detection of cancer driver genes. Nature Communications *10*, 3399. 10.1038/s41467-019-11284-9.
119. Cai, X., Wang, X., Cao, C., Gao, Y., Zhang, S., Yang, Z., Liu, Y., Zhang, X., Zhang, W., and Ye, L. (2018). HBXIP-elevated methyltransferase METTL3 promotes the progression of breast cancer via inhibiting tumor suppressor let-7g. Cancer Lett *415*, 11–19. 10.1016/j.canlet.2017.11.018.
120. Shi, Y., Zheng, C., Jin, Y., Bao, B., Wang, D., Hou, K., Feng, J., Tang, S., Qu, X., Liu, Y., et al. (2020). Reduced Expression of METTL3 Promotes Metastasis of Triple-Negative Breast

Cancer by m6A Methylation-Mediated COL3A1 Up-Regulation. Front Oncol *10*, 1126. 10.3389/fonc.2020.01126.

121. Uddin, M.B., Roy, K.R., Hosain, S.B., Khiste, S.K., Hill, R.A., Jois, S.D., Zhao, Y., Tackett, A.J., and Liu, Y.Y. (2019). An N(6)-methyladenosine at the transited codon 273 of p53 pre-mRNA promotes the expression of R273H mutant protein and drug resistance of cancer cells. Biochem Pharmacol *160*, 134–145. 10.1016/j.bcp.2018.12.014.
122. Deng, R., Cheng, Y., Ye, S., Zhang, J., Huang, R., Li, P., Liu, H., Deng, Q., Wu, X., Lan, P., and Deng, Y. (2019). m(6)A methyltransferase METTL3 suppresses colorectal cancer proliferation and migration through p38/ERK pathways. Onco Targets Ther *12*, 4391–4402. 10.2147/ott.S201052.
123. Wang, K., Jiang, L., Zhang, Y., and Chen, C. (2020). Progression of Thyroid Carcinoma Is Promoted by the m6A Methyltransferase METTL3 Through Regulating m(6)A Methylation on TCF1. Onco Targets Ther *13*, 1605–1612. 10.2147/ott.S234751.
124. He, J., Zhou, M., Yin, J., Wan, J., Chu, J., Jia, J., Sheng, J., Wang, C., Yin, H., and He, F. (2021). METTL3 restrains papillary thyroid cancer progression via m(6)A/c-Rel/IL-8-mediated neutrophil infiltration. Mol Ther *29*, 1821–1837. 10.1016/j.ymthe.2021.01.019.
125. Liu, J., Eckert, M.A., Harada, B.T., Liu, S.M., Lu, Z., Yu, K., Tienda, S.M., Chryplewicz, A., Zhu, A.C., Yang, Y., et al. (2018). m(6)A mRNA methylation regulates AKT activity to promote the proliferation and tumorigenicity of endometrial cancer. Nat Cell Biol *20*, 1074–1083. 10.1038/s41556-018-0174-4.
126. Li, X., Tang, J., Huang, W., Wang, F., Li, P., Qin, C., Qin, Z., Zou, Q., Wei, J., Hua, L., et al. (2017). The M6A methyltransferase METTL3: acting as a tumor suppressor in renal cell carcinoma. Oncotarget *8*, 96103–96116. 10.18632/oncotarget.21726.
127. Yankova, E., Blackaby, W., Albertella, M., Rak, J., De Braekeleer, E., Tsagkogeorga, G., Pilka, E.S., Aspris, D., Leggate, D., Hendrick, A.G., et al. (2021). Small-molecule inhibition of METTL3 as a strategy against myeloid leukaemia. Nature *593*, 597–601. 10.1038/s41586-021-03536-w.
128. Sun, Y., Shen, W., Hu, S., Lyu, Q., Wang, Q., Wei, T., Zhu, W., and Zhang, J. (2023). METTL3 promotes chemoresistance in small cell lung cancer by inducing mitophagy. J Exp Clin Cancer Res *42*, 65. 10.1186/s13046-023-02638-9.
129. An, X., Wu, W., Yang, L., Dong, J., Liu, B., Guo, J., Chen, J., Guo, B., Cao, W., and Jiang, Q. (2023). ZBTB7C m6A modification incurred by METTL3 aberration promotes osteosarcoma progression. Transl Res *259*, 62–71. 10.1016/j.trsl.2023.04.005.
130. Xu, Q.C., Tien, Y.C., Shi, Y.H., Chen, S., Zhu, Y.Q., Huang, X.T., Huang, C.S., Zhao, W., and Yin, X.Y. (2022). METTL3 promotes intrahepatic cholangiocarcinoma progression by regulating IFIT2 expression in an m(6)A-YTHDF2-dependent manner. Oncogene *41*, 1622–1633. 10.1038/s41388-022-02185-1.
131. Gao, J., Fang, Y., Chen, J., Tang, Z., Tian, M., Jiang, X., Tao, C., Huang, R., Zhu, G., Qu, W., et al. (2023). Methyltransferase like 3 inhibition limits intrahepatic cholangiocarcinoma metabolic reprogramming and potentiates the efficacy of chemotherapy. Oncogene *42*, 2507–2520. 10.1038/s41388-023-02760-0.

132. Wang, L., Yang, Q., Zhou, Q., Fang, F., Lei, K., Liu, Z., Zheng, G., Zhu, L., Huo, J., Li, X., et al. (2023). METTL3-m(6)A-EGFR-axis drives lenvatinib resistance in hepatocellular carcinoma. Cancer Lett *559*, 216122. 10.1016/j.canlet.2023.216122.

133. Guirguis, A.A., Ofir-Rosenfeld, Y., Knezevic, K., Blackaby, W., Hardick, D., Chan, Y.C., Motazedian, A., Gillespie, A., Vassiliadis, D., Lam, E.Y.N., et al. (2023). Inhibition of METTL3 Results in a Cell-Intrinsic Interferon Response That Enhances Antitumor Immunity. Cancer Discov *13*, 2228–2247. 10.1158/2159-8290.Cd-23-0007.

134. Pan, Y., Chen, H., Zhang, X., Liu, W., Ding, Y., Huang, D., Zhai, J., Wei, W., Wen, J., Chen, D., et al. (2023). METTL3 drives NAFLD-related hepatocellular carcinoma and is a therapeutic target for boosting immunotherapy. Cell Rep Med *4*, 101144. 10.1016/j.xcrm.2023.101144.

135. Chen, H., Pan, Y., Zhou, Q., Liang, C., Wong, C.C., Zhou, Y., Huang, D., Liu, W., Zhai, J., Gou, H., et al. (2022). METTL3 Inhibits Antitumor Immunity by Targeting m(6)A-BHLHE41-CXCL1/CXCR2 Axis to Promote Colorectal Cancer. Gastroenterology *163*, 891–907. 10.1053/j.gastro.2022.06.024.

136. Yu, H., Liu, J., Bu, X., Ma, Z., Yao, Y., Li, J., Zhang, T., Song, W., Xiao, X., Sun, Y., et al. (2023). Targeting METTL3 reprograms the tumor microenvironment to improve cancer immunotherapy. Cell Chem Biol *31*, 776–791. 10.1016/j.chembiol.2023.09.001.

137. Moser, J.C., Papadopoulos, K.P., Ahnert, J.R., Ofir-Rosenfeld, Y., and Holz, J.-B. (2024). Phase 1 dose escalation and cohort expansion study evaluating safety, PK, PD and clinical activity of STC-15, a METTL-3 inhibitor, in patients with advanced malignancies. Journal of Clinical Oncology *42*, 2586–2586. 10.1200/JCO.2024.42.16_suppl.2586.

138. Han, J., Wang, J.Z., Yang, X., Yu, H., Zhou, R., Lu, H.C., Yuan, W.B., Lu, J.C., Zhou, Z.J., Lu, Q., et al. (2019). METTL3 promote tumor proliferation of bladder cancer by accelerating pri-miR221/222 maturation in m6A-dependent manner. Mol Cancer *18*, 110. 10.1186/s12943-019-1036-9.

139. Gao, Q., Zheng, J., Ni, Z., Sun, P., Yang, C., Cheng, M., Wu, M., Zhang, X., Yuan, L., Zhang, Y., and Li, Y. (2020). The m(6)A Methylation-Regulated AFF4 Promotes Self-Renewal of Bladder Cancer Stem Cells. Stem Cells Int *2020*, 8849218. 10.1155/2020/8849218.

140. Jin, H., Ying, X., Que, B., Wang, X., Chao, Y., Zhang, H., Yuan, Z., Qi, D., Lin, S., Min, W., et al. (2019). N6-methyladenosine modification of ITGA6 mRNA promotes the development and progression of bladder cancer. EBioMedicine *47*, 195–207. https://doi.org/10.1016/j.ebiom.2019.07.068.

141. Ni, Z., Sun, P., Zheng, J., Wu, M., Yang, C., Cheng, M., Yin, M., Cui, C., Wang, G., Yuan, L., et al. (2022). JNK Signaling Promotes Bladder Cancer Immune Escape by Regulating METTL3-Mediated m6A Modification of PD-L1 mRNA. Cancer Res *82*, 1789–1802. 10.1158/0008-5472.Can-21-1323.

142. Wang, G., Dai, Y., Li, K., Cheng, M., Xiong, G., Wang, X., Chen, S., Chen, Z., Chen, J., Xu, X., et al. (2021). Deficiency of Mettl3 in Bladder Cancer Stem Cells Inhibits Bladder Cancer Progression and Angiogenesis. Frontiers in Cell and Developmental Biology *9*. 10.3389/fcell.2021.627706.

143. Liu, H., Gu, J., Huang, Z., Han, Z., Xin, J., Yuan, L., Du, M., Chu, H., Wang, M., and Zhang, Z. (2022). Fine particulate matter induces METTL3-mediated m(6)A modification of

BIRC5 mRNA in bladder cancer. J Hazard Mater *437*, 129310. 10.1016/j.jhazmat.2022.129310.

144. Yang, F., Jin, H., Que, B., Chao, Y., Zhang, H., Ying, X., Zhou, Z., Yuan, Z., Su, J., Wu, B., et al. (2019). Dynamic m(6)A mRNA methylation reveals the role of METTL3-m(6)A-CDCP1 signaling axis in chemical carcinogenesis. Oncogene *38*, 4755–4772. 10.1038/s41388-019-0755-0.
145. Ying, X., Jiang, X., Zhang, H., Liu, B., Huang, Y., Zhu, X., Qi, D., Yuan, G., Luo, J., and Ji, W. (2020). Programmable N6-methyladenosine modification of CDCP1 mRNA by RCas9-methyltransferase like 3 conjugates promotes bladder cancer development. Mol Cancer *19*, 169. 10.1186/s12943-020-01289-0.
146. Xie, H., Li, J., Ying, Y., Yan, H., Jin, K., Ma, X., He, L., Xu, X., Liu, B., Wang, X., et al. (2020). METTL3/YTHDF2 m(6) A axis promotes tumorigenesis by degrading SETD7 and KLF4 mRNAs in bladder cancer. J Cell Mol Med *24*, 4092–4104. 10.1111/jcmm.15063.
147. Zhang, L., Li, Y., Zhou, L., Zhou, H., Ye, L., Ou, T., Hong, H., Zheng, S., Zhou, Z., Wu, K., et al. (2023). The m6A Reader YTHDF2 Promotes Bladder Cancer Progression by Suppressing RIG-I-Mediated Immune Response. Cancer Res *83*, 1834–1850. 10.1158/0008-5472.Can-22-2485.
148. Geula, S., Moshitch-Moshkovitz, S., Dominissini, D., Mansour, A.A., Kol, N., Salmon-Divon, M., Hershkovitz, V., Peer, E., Mor, N., Manor, Y.S., et al. (2015). Stem cells. m6A mRNA methylation facilitates resolution of naïve pluripotency toward differentiation. Science *347*, 1002–1006. 10.1126/science.1261417.
149. Poh, H.X., Mirza, A.H., Pickering, B.F., and Jaffrey, S.R. (2022). Alternative splicing of METTL3 explains apparently METTL3-independent m6A modifications in mRNA. PLoS Biology *20*, e3001683. 10.1371/journal.pbio.3001683.
150. Zhang, L., Chen, Z., Sun, G., Li, C., Wu, P., Xu, W., Zhu, H., Zhang, Z., Tang, Y., Li, Y., et al. (2024). Dynamic landscape of m6A modifications and related post-transcriptional events in muscle-invasive bladder cancer. J Transl Med *22*, 912. 10.1186/s12967-024-05701-x.
151. Dempster, J.M., Boyle, I., Vazquez, F., Root, D.E., Boehm, J.S., Hahn, W.C., Tsherniak, A., and McFarland, J.M. (2021). Chronos: a cell population dynamics model of CRISPR experiments that improves inference of gene fitness effects. Genome Biol *22*, 343. 10.1186/s13059-021-02540-7.
152. Support, I.T. Adapter dimers causes, effects, and how to remove them. https://knowledge.illumina.com/library-preparation/general/library-preparation-general-troubleshooting-list/000001911.
153. Sui, X., Lei, L., Chen, L., Xie, T., and Li, X. (2017). Inflammatory microenvironment in the initiation and progression of bladder cancer. Oncotarget *8*, 93279–93294. 10.18632/oncotarget.21565.
154. Goriki, A., Seiler, R., Wyatt, A.W., Contreras-Sanz, A., Bhat, A., Matsubara, A., Hayashi, T., and Black, P.C. (2018). Unravelling disparate roles of NOTCH in bladder cancer. Nat Rev Urol *15*, 345–357. 10.1038/s41585-018-0005-1.
155. Knowles, M.A., and Hurst, C.D. (2015). Molecular biology of bladder cancer: new insights into pathogenesis and clinical diversity. Nat Rev Cancer *15*, 25–41. 10.1038/nrc3817.

156. Millet, C., and Zhang, Y.E. (2007). Roles of Smad3 in TGF-beta signaling during carcinogenesis. Crit Rev Eukaryot Gene Expr *17*, 281–293. 10.1615/critreveukargeneexpr.v17.i4.30.

157. Mao, B., Zhang, Z., and Wang, G. (2015). BTG2: a rising star of tumor suppressors (review). Int J Oncol *46*, 459–464. 10.3892/ijo.2014.2765.

158. Yuniati, L., Scheijen, B., van der Meer, L.T., and van Leeuwen, F.N. (2019). Tumor suppressors BTG1 and BTG2: Beyond growth control. J Cell Physiol *234*, 5379–5389. 10.1002/jcp.27407.

159. Zaharieva, B., Simon, R., Ruiz, C., Oeggerli, M., Mihatsch, M.J., Gasser, T., Sauter, G., and Toncheva, D. (2005). High-throughput tissue microarray analysis of CMYC amplificationin urinary bladder cancer. Int J Cancer *117*, 952–956. 10.1002/ijc.21253.

160. Kluth, M., Hitzschke, M., Lennartz, M., Blessin, N.C., Sauter, G., Plage, H., Klatte, T., Schlomm, T., Marx, A.H., Rink, M., et al. (2023). MYC amplifications are a common event in urothelial bladder carcinomas associated with an aggressive tumor phenotype. American Journal of Clinical Pathology *160*, S91–S92. 10.1093/ajcp/aqad150.202.

161. Bou Zerdan, M., Bratslavsky, G., Jacob, J., Ross, J., Huang, R., and Basnet, A. (2023). Urothelial Bladder Cancer: Genomic Alterations in Fibroblast Growth Factor Receptor. Mol Diagn Ther *27*, 475–485. 10.1007/s40291-023-00647-0.

162. Helsten, T., Elkin, S., Arthur, E., Tomson, B.N., Carter, J., and Kurzrock, R. (2016). The FGFR Landscape in Cancer: Analysis of 4,853 Tumors by Next-Generation Sequencing. Clin Cancer Res *22*, 259–267. 10.1158/1078-0432.Ccr-14-3212.

163. Fleischmann, A., Rotzer, D., Seiler, R., Studer, U.E., and Thalmann, G.N. (2011). Her2 amplification is significantly more frequent in lymph node metastases from urothelial bladder cancer than in the primary tumours. Eur Urol *60*, 350–357. 10.1016/j.eururo.2011.05.035.

164. Xia, Z., Donehower, L.A., Cooper, T.A., Neilson, J.R., Wheeler, D.A., Wagner, E.J., and Li, W. (2014). Dynamic analyses of alternative polyadenylation from RNA-seq reveal a 3'-UTR landscape across seven tumour types. Nat Commun *5*, 5274. 10.1038/ncomms6274.

165. Zaccara, S., Ries, R.J., and Jaffrey, S.R. (2019). Reading, writing and erasing mRNA methylation. Nature Reviews Molecular Cell Biology *20*, 608–624. 10.1038/s41580-019-0168-5.

166. Jiang, X., Liu, B., Nie, Z., Duan, L., Xiong, Q., Jin, Z., Yang, C., and Chen, Y. (2021). The role of m6A modification in the biological functions and diseases. Signal Transduct Target Ther *6*, 74. 10.1038/s41392-020-00450-x.

167. Boulias, K., and Greer, E.L. (2023). Biological roles of adenine methylation in RNA. Nature Reviews Genetics *24*, 143–160. 10.1038/s41576-022-00534-0.

168. Yang, L., Ying, J., Tao, Q., and Zhang, Q. (2024). RNA N(6)-methyladenosine modifications in urological cancers: from mechanism to application. Nat Rev Urol *21*, 460–476. 10.1038/s41585-023-00851-x.

169. Li, T., Hu, P.S., Zuo, Z., Lin, J.F., Li, X., Wu, Q.N., Chen, Z.H., Zeng, Z.L., Wang, F., Zheng, J., et al. (2019). METTL3 facilitates tumor progression via an m(6)A-IGF2BP2-dependent mechanism in colorectal carcinoma. Mol Cancer *18*, 112. 10.1186/s12943-019-1038-7.

170. Murakami, S., and Jaffrey, S.R. (2022). Hidden codes in mRNA: Control of gene expression by m(6)A. Mol Cell *82*, 2236–2251. 10.1016/j.molcel.2022.05.029.
171. Chang, L., Ruiz, P., Ito, T., and Sellers, W.R. (2021). Targeting pan-essential genes in cancer: Challenges and opportunities. Cancer Cell *39*, 466–479. 10.1016/j.ccell.2020.12.008.
172. Rudd, S.G. (2023). Targeting pan-essential pathways in cancer with cytotoxic chemotherapy: challenges and opportunities. Cancer Chemother Pharmacol *92*, 241–251. 10.1007/s00280-023-04562-3.
173. Liu, J., Li, K., Cai, J., Zhang, M., Zhang, X., Xiong, X., Meng, H., Xu, X., Huang, Z., Peng, J., et al. (2020). Landscape and Regulation of m(6)A and m(6)Am Methylome across Human and Mouse Tissues. Mol Cell *77*, 426–440.e426. 10.1016/j.molcel.2019.09.032.
174. Barbieri, I., and Kouzarides, T. (2020). Role of RNA modifications in cancer. Nat Rev Cancer *20*, 303–322. 10.1038/s41568-020-0253-2.
175. Li, H., Li, C., Zhang, Y., Jiang, W., Zhang, F., Tang, X., Sun, G., Xu, S., Dong, X., Shou, J., et al. (2024). Comprehensive analysis of m(6) A methylome and transcriptome by Nanopore sequencing in clear cell renal carcinoma. Mol Carcinog *63*, 677–687. 10.1002/mc.23680.
176. Qin, H., Ou, L., Gao, J., Chen, L., Wang, J.W., Hao, P., and Li, X. (2022). DENA: training an authentic neural network model using Nanopore sequencing data of Arabidopsis transcripts for detection and quantification of N(6)-methyladenosine on RNA. Genome Biol *23*, 25. 10.1186/s13059-021-02598-3.
177. Lee, Q., Song, R., Phan, D.A.V., Pinello, N., Tieng, J., Su, A., Halstead, J.M., Wong, A.C.H., van Geldermalsen, M., Lee, B.S., et al. (2023). Overexpression of VIRMA confers vulnerability to breast cancers via the m(6)A-dependent regulation of unfolded protein response. Cell Mol Life Sci *80*, 157. 10.1007/s00018-023-04799-4.
178. Tian, B., and Manley, J.L. (2017). Alternative polyadenylation of mRNA precursors. Nat Rev Mol Cell Biol *18*, 18–30. 10.1038/nrm.2016.116.
179. Yuan, F., Hankey, W., Wagner, E.J., Li, W., and Wang, Q. (2021). Alternative polyadenylation of mRNA and its role in cancer. Genes Dis *8*, 61–72. 10.1016/j.gendis.2019.10.011.
180. Destefanis, E., Sighel, D., Dalfovo, D., Gilmozzi, R., Broso, F., Cappannini, A., Bujnicki, J.M., Romanel, A., Dassi, E., and Quattrone, A. (2024). The three YTHDF paralogs and VIRMA are the major tumor drivers among the m⁶A core genes in a pan-cancer analysis. bioRxiv, 2024.2006.2013.598899. 10.1101/2024.06.13.598899.
181. Li, N., Zhu, Z., Deng, Y., Tang, R., Hui, H., Kang, Y., and Rana, T.M. (2023). KIAA1429/VIRMA promotes breast cancer progression by m(6) A-dependent cytosolic HAS2 stabilization. EMBO Rep *24*, e55506. 10.15252/embr.202255506.
182. Zhu, C., Cheng, Y., Yu, Y., Zhang, Y., and Ren, G. (2024). VIRMA promotes the progression of head and neck squamous cell carcinoma by regulating UBR5 mRNA and m6A levels. Biomol Biomed *24*, 1244–1257. 10.17305/bb.2024.10358.
183. Zheng, Z.Q., Huang, Z.H., Liang, Y.L., Zheng, W.H., Xu, C., Li, Z.X., Liu, N., Yang, P.Y., Li, Y.Q., Ma, J., et al. (2023). VIRMA promotes nasopharyngeal carcinoma, tumorigenesis, and metastasis by upregulation of E2F7 in an m6A-dependent manner. J Biol Chem *299*, 104677. 10.1016/j.jbc.2023.104677.

184. Yang, K., Zhong, Z., Zou, J., Liao, J.Y., Chen, S., Zhou, S., Zhao, Y., Li, J., Yin, D., Huang, K., and Li, Y. (2024). Glycolysis and tumor progression promoted by the m(6)A writer VIRMA via m(6)A-dependent upregulation of STRA6 in pancreatic ductal adenocarcinoma. Cancer Lett *590*, 216840. 10.1016/j.canlet.2024.216840.
185. Zhu, W., Wang, J.Z., Wei, J.F., and Lu, C. (2021). Role of m6A methyltransferase component VIRMA in multiple human cancers (Review). Cancer Cell Int *21*, 172. 10.1186/s12935-021-01868-1.
186. Siegfried, N.A., Busan, S., Rice, G.M., Nelson, J.A.E., and Weeks, K.M. (2014). RNA motif discovery by SHAPE and mutational profiling (SHAPE-MaP). Nature Methods *11*, 959–965. 10.1038/nmeth.3029.
187. Zheng, D., Liu, X., and Tian, B. (2016). 3'READS+, a sensitive and accurate method for 3' end sequencing of polyadenylated RNA. RNA *22*, 1631–1639. 10.1261/rna.057075.116.
188. Yu, F., Zhang, Y., Cheng, C., Wang, W., Zhou, Z., Rang, W., Yu, H., Wei, Y., Wu, Q., and Zhang, Y. (2020). Poly(A)-seq: A method for direct sequencing and analysis of the transcriptomic poly(A)-tails. PLoS One *15*, e0234696. 10.1371/journal.pone.0234696.
189. Sun, H., Lu, B., Zhang, Z., Xiao, Y., Zhou, Z., Xi, L., Li, Z., Jiang, Z., Zhang, J., Wang, M., et al. (2025). Mild and ultrafast GLORI enables absolute quantification of m6A methylome from low-input samples. Nature Methods. 10.1038/s41592-025-02680-9.
190. Patel, A., Mitrea, D., Namasivayam, V., Murcko, M.A., Wagner, M., and Klein, I.A. (2022). Principles and functions of condensate modifying drugs. Front Mol Biosci *9*, 1007744. 10.3389/fmolb.2022.1007744.
191. Mitrea, D.M., Mittasch, M., Gomes, B.F., Klein, I.A., and Murcko, M.A. (2022). Modulating biomolecular condensates: a novel approach to drug discovery. Nature Reviews Drug Discovery *21*, 841–862. 10.1038/s41573-022-00505-4.
192. Guzmán, C., Bagga, M., Kaur, A., Westermarck, J., and Abankwa, D. (2014). ColonyArea: an ImageJ plugin to automatically quantify colony formation in clonogenic assays. PLoS One *9*, e92444. 10.1371/journal.pone.0092444.
193. Ge, S.X., Jung, D., and Yao, R. (2020). ShinyGO: a graphical gene-set enrichment tool for animals and plants. Bioinformatics *36*, 2628–2629. 10.1093/bioinformatics/btz931.
194. Koch, J., Neuberger, M., Schmidt-Dengler, M., Xu, J., Carneiro, V.C., Ellinger, J., Kriegmair, M.C., Nuhn, P., Erben, P., Michel, M.S., et al. (2023). Reinvestigating the clinical relevance of the m(6)A writer METTL3 in urothelial carcinoma of the bladder. iScience *26*, 107300. 10.1016/j.isci.2023.107300.
195. Love, M.I., Huber, W., and Anders, S. (2014). Moderated estimation of fold change and dispersion for RNA-seq data with DESeq2. Genome Biology *15*, 550. 10.1186/s13059-014-0550-8.
196. Hubstenberger, A., Courel, M., Bénard, M., Souquere, S., Ernoult-Lange, M., Chouaib, R., Yi, Z., Morlot, J.-B., Munier, A., Fradet, M., et al. (2017). P-Body Purification Reveals the Condensation of Repressed mRNA Regulons. Molecular Cell *68*, 144–157.e145. https://doi.org/10.1016/j.molcel.2017.09.003.